Doctoral Thesis

A Versatile Halide Substitution Method for Advanced Halide Perovskite Optoelectronics

Yung Jin Yoon

School of Energy and Chemical Engineering
(Energy Engineering)

Ulsan National Institute of Science and Technology

2021

A Versatile Halide Substitution Method for Advanced Halide Perovskite Optoelectronics

Yung Jin Yoon

School of Energy and Chemical Engineering
(Energy Engineering)

Ulsan National Institute of Science and Technology

A Versatile Halide Substitution Method for Advanced Halide Perovskite Optoelectronics

A thesis/dissertation submitted to
Ulsan National Institute of Science and Technology
in partial fulfillment of the
requirements for the degree of
Doctor of Philosophy

Yung Jin Yoon

11/26/2020 of submission

Approved by

Advisor
Jin Young Kim

A Versatile Halide Substitution Method for Advanced Halide Perovskite Optoelectronics

Yung Jin Yoon

This certifies that the thesis/dissertation of Yung Jin Yoon is approved.

11/26/2020 of submission

Signature

Advisor: Jin Young Kim

Signature

Myoung Hoon Song: Thesis Committee Member #1

Signature

Jongnam Park: Thesis Committee Member #2

Signature

Tae-Hyuk Kwon: Thesis Committee Member #3

Signature

Gi-Hwan Kim: Thesis Committee Member #4;

Abstract

Halide perovskites are considered as promising material for the next generation light emitting diodes, due to its high color purity, easily tunable bandgap, cheap precursors, and solution processability. This thesis covers post treatment methods for halide perovskites nanocrystals and bulk halide perovskites to tune the bandgap, and their device applications. First, bandgap tuning method for $CsPbBr_3$ halide perovskite nanocrystals (PeNCs) is developed with newly introduced tridodecylmethyl ammonium iodide (TrDAI) ligand. The Br halides in the original perovskite nanocrystals were exchanged with I halides in the TrDAI ligand with assistance of the anti-solvent, and the bandgap was narrowed to obtain the red emission with high photoluminescence quantum yield (~ 90%). The red emitting PeNCs were applied to the halide perovskite light emitting diodes (PeLEDs). With the ligand passivation effect, the halide segregation was successfully suppressed and the PeLEDs maintained original emission peak. The next chapter focus on the newly developed reversible and non-destructive halide exchange method. The halide containing solvents, such as chloroform, bromoform, or ethyl iodide, were used as halide sources, which were stable in typical states. The halides in the solvents were detached by the assistance of the strong nucleophilic ligand. With the computational simulation on reaction paths and the detection of the biproducts, the reaction mechanism was clearly revealed. Due to the understanding of the reaction mechanism, the halide exchange process was finely tuned. Then, the PeNCs and the PeLEDs of desired color, which covers all visible wavelength region, were achievable with a single batch of pristine PeNCs. Following chapter introduces the insight on the emission spectra width of the PeNCs. To narrow the emission spectra, the factors of PeNCs which have effect on the emission spectra width were studied. Interestingly, it was found that the emission spectra width was dominantly affected by the mean size, not by the size distribution. With the developed surface passivation method, which is modified halide exchange method, the emission spectra could be more narrowed by the ligand passivation effect. The blue color PeLEDs were fabricated with surface passivated PeNCs, resulted very narrow emission spectra and high color purity. Finally, the halide exchange method was applied to the inorganic bulk state halide perovskites to get blue emissive layer. Because of the low solubility of the Cl precursor, inorganic bulk halide perovskite was expected to be difficult to fabricate. However, by exchanging halides in the well fabricated inorganic bulk $CsPbBr_3$ film with Cl, the inorganic bulk blue perovskite was able to be fabricated. The new approach of fabrication method for inorganic bulk blue PeLEDs could suggest the breakthrough pathway to achieve highly efficient blue PeLEDs. Development of post treatment methods for the halide perovskites presents deep understand for following studies, and enabling devices with halide perovskite to be applied to our real life.

Table of Contents

List of Figures

List of Tables

Abbreviation

Abbreviation	Description
LED	light emitting diode
EL	electroluminescence
OLED	organic light emitting diode
AMOLED	active-matrix organic light emitting diode
QLED	quantum dot light emitting diode
QD	quantum dot
PeLED	halide perovskite light emitting diode
NCs	nanocrystals
PeNCs	halide perovskite nanocrystals
NTSC	national television system committee
MA	methyl ammonium
FA	formamidinium
PL	photoluminescence
PLQY	photoluminescence quantum yield
OA	oleic acid
OAm	oleyl amine
TOP	trioctylphosphine
CB	chlorobenzene
CF	chloroform
Tol	toluene
ETL	electron transport layer
HTL	hole transport layer
WF	work function
ITO	indium tin oxide

FTO	fluorine doped tin oxide
IQE	internal quantum efficiency
EQE	external quantum efficiency
CE	current efficiency
PE	power efficiency
LHP	lead halide perovskite
FWHM	full width at half maximum
LMPT	ligand mediated post-treatment
BuOH	butanol
PEDOT:PSS	poly(3,4-ethylenedioxythiophene) polystyrene sulfonate
Poly-TPD	poly(N,N'-bis-4-butylphenyl-N,N'-bisphenyl)benzidine
TPBi	2,2',2''-(1,3,5-benzinetriyl)-tris(1-phenyl-1-H-benzimidazole)
TEM	transmission Electron Microscopy
TCSPC	time-correlated single-photon counting
XPS	X-ray Photoelectron Spectroscopy
FTIR	Fourier Transform Infrared Spectroscopy
XRD	X-ray diffraction
IPA	isopropyl alcohol
HIL	hole injection layer
EIL	electron injection layer
UV	ultraviolet
DFT	density functional theory
GGA	Generalized gradient approximation
PBE	Perdew-Burke-Ernzerhof
DNP	double numerical plus polarization
PBC	periodic boundary conditions
COSMO	conductor-like screening model
TS	transition state
LST/QST	transit/quadratic synchronous transit

RMS	root mean square
PT	post treatment
PR	pristine
SN	strong nucleophile
AFM	atomic force microscope
THP	trihexylphosphine
TBP	tributylphosphine
SD	standard deviation
SP	surface passivated
DMSO	dimethylsulfoxide
HIL	hole injection layer
TFA	trifluoroacetate
UPS	ultraviolet photoelectron spectroscopy

CHAPTER 1. Introduction

Energy crisis is not a distant future. Energy sources, such as fossil fuels or nuclear fuels, are limited resources and one day it will run out. To prepare for the energy crisis, we should not only develop the renewable energy, but also develop the energy efficient electric devices. Among the uses of electricity, the lighting accounts for about 15% of the world's power consumption and demand for display panels is increasing year by year.[1] The light emitting diodes (LEDs) can be a strong candidate for these applications. The white LEDs for lighting applications shows significantly higher efficiency than conventional light sources such as incandescent bulbs, halogen lamps, and fluorescent lamps. The monochromatic LEDs are also known as energy efficient component for nowadays displays.

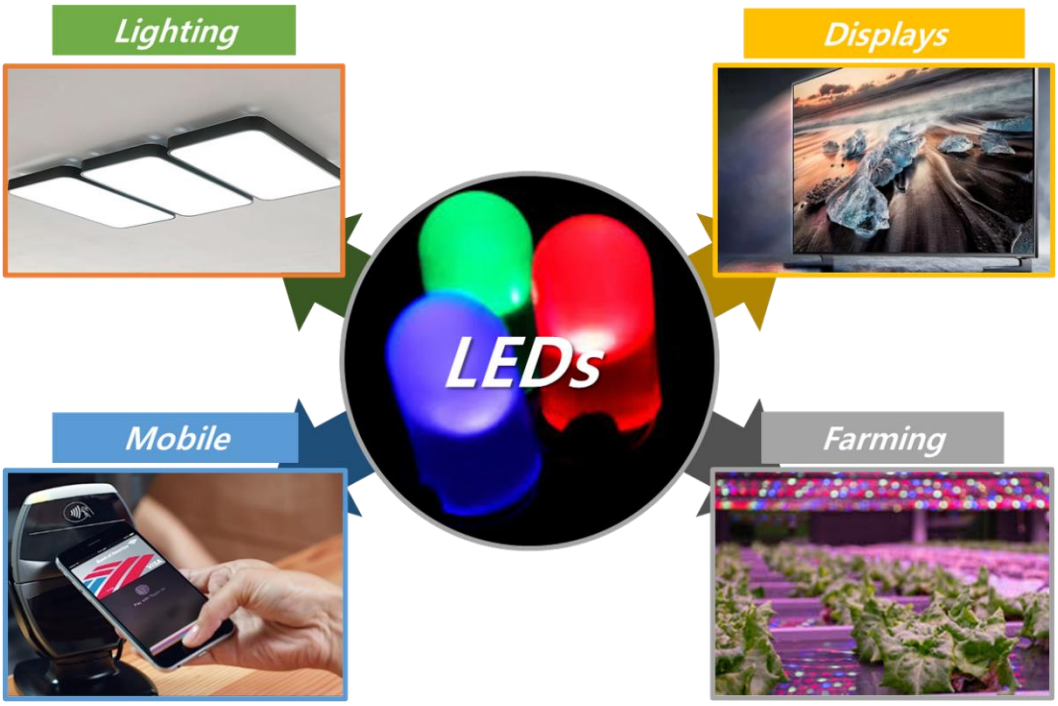

Figure 1.1. LED application fields.

High energy efficiency is a typical part of the benefits of LEDs, besides structural simplicity, long device lifetime, and high color purity. These advantages attracted vast researchers and now the LEDs are used in everywhere. The LEDs are used for lighting in our daily life, displays for various purposes and sizes, wireless telecommunications, medical and environmental fields, and even used in farming field as artificial lighting.

These versatile LEDs have been researched more than 100 years. The first LED was born in 1907 by Round.[2] The first LEDs were based on the SiC crystallite with metal electrodes, forming Schottky diodes and emitted the first electroluminescence (EL). The first practical LEDs were based on the GaAs semiconductors, emitting red light, in 1962.[3] Based on this discovery, combination with GaP resulted green LEDs and GaAsP based LEDs were invented achieving bright red to green color with control of material characteristics.[4, 5] In 1994, the first bright blue LEDs were invented by the Nakamura Shuji with GaN semiconductor and the era of LEDs were begun.[6] The LEDs based on these crystalline semiconductors achieved very high efficiency and widely used but have disadvantages of heavy weight and brittle nature.

The organic LEDs (OLEDs) have been researched as alternative candidate for the next LEDs, due to light weight, flexible material property, and solution process which is favorable to mass production. By the Tang and Van Slyke, the first OLED was introduced to the world in 1987.[7] Nowadays, the OLEDs have been improved with enormous developments of organic materials and with structural development of active-matrix OLEDs (AMOLED). State-of-art smart phones are consisting displays based on the OLEDs, even in the shape of foldable or flexible displays.

The quantum dot LEDs (QLEDs) are LEDs consisting quantum dots (QDs) for emissive layers and expected to be commercialized soon. The QDs are the inorganic nanoparticles enwrapped with the organic ligands. By the assistance of the organic ligands, the several physical properties, such as hydrophobic nature or surface energy, of the QDs resembles the organic materials. Therefore, the QLEDs succeed to advantages of OLEDs, with better color purity and stability. In 1994, the first QLED was reported by the Colvin et al. based on the CdSe QDs, and after then vast research were conducted.[8] With the excellent optical properties of the QDs, the QDs are used as emissive layer combined with liquid crystal display (LCD) back light for now. There were known problems of QDs to make successful QLEDs, such as toxicity of heavy metal and low stability, but hopefully these problems were solved with Zn base QDs recently,[9] and ready to be commercialized.

The halide perovskite LEDs (PeLEDs) are immerging LEDs as components for the next generation displays. The strongest point of halide perovskite as emissive material is very narrow emission spectra. The QLEDs that has previous narrowest emission spectra, shows emission spectra width about 30 nm for green color, but the PeLEDs shows emission spectra width about 20 nm for green color. Moreover, the halide perovskite is turned out to have many advantages; high charge mobility, low trap density, and high photoluminescence quantum yield, and succeed the advantages of previous LEDs. With the various advantages, the PeLEDs achieved high device performance recently.[10-12]

Another reason why PeLEDs draws attraction in LED field is easily tunable electronic bandgap property. In the LEDs, the bandgap determines almost everything. The color of the LEDs is determined by the size of the bandgap, the device structure is based on the bandgap position of the emissive layer,

the efficiency is greatly affected by the trap states in the bandgap. Therefore, the control of the bandgap is key technique of developing the LEDs. The important thing is that the bandgap of the halide perovskite could be easily and finely tuned by controlling the halides in the material. Thus, developing the halide tuning method results in the improvements of PeLED performance.

In this thesis, the halide substitution methods for advanced halide perovskite devices are described. The method is based on the mobile character of the halides in the halide perovskite. Due the mobile character, the halides in the material could be tuned just by supply the halides to the material. Following chapter provides properties of halide perovskite and device physics background for the better understand of the thesis.

In **Chapter 3**, simple ligand exchange post treatment method to narrow the bandgap of the halide perovskite nanocrystals (PeNCs), to obtain the red color emission. The halides in the PeNCs were exchanged with halides in the treated ligands. The exchange process was triggered by the anti-solvent, and readily purified through the centrifugation. The treated PeNCs were successfully applied to the PeLEDs.

Chapter 4 demonstrates all solution halide exchange post treatment method for PeNCs. The method used halide containing solvents to supply the halides. Overall detachment mechanism was deeply researched through the computational expects and biproduct detection. With the post treatment method, the PeNCs with various emission peaks covering all visible wavelength region were made with a single batch of the PeNCs. The red, green, blue color PeLED were successfully fabricated which satisfies NTSC standard.

Chapter 5 provides understanding on the narrow emission spectra of the PeNCs and method for making narrower emission spectra. Systematic analysis was conducted by control over synthetic conditions. Briefly, the mean size of the PeNCs have great effect on the emission spectra. The surface passivation post treatment method was developed, which was modified method of halide exchange method in the **Chapter 4**. The surface passivation was conducted by treating the surface defects on the PeNCs with supplying the halides and the ligands, and narrow blue color emission spectra (16.72 nm) were obtained with PeLEDs.

Chapter 6 is devoted to developing fabrication method for inorganic bulk blue PeLEDs. The inorganic bulk blue PeLEDs were hard to fabricate due to the low solubility of the Cl precursors. To break through the solubility problem, the Cl halides were supplied to form the blue emitting inorganic bulk blue halide perovskite after the fabrication films, not at the start of the fabrication. To supply and exchange the halides, modified halide exchange method in the **Chapter 4** was applied. The inorganic bulk blue PeLEDs were successfully fabricated and recorded highest device performance.

The conclusion and perspective on the field are presented in the last chapter.

CHAPTER 2. Halide Perovskite Material Characteristics and Device Physics of Halide Perovskite Light Emitting Diodes

This chapter provides backgrounds of the halide perovskite material properties and device physics on which there is little discussion in each chapter. It covers from general characteristics of halide perovskites, operating mechanism of LEDs, and figures of merit of each LEDs to get a thorough understanding of device application.

2.1 Properties of Halide Perovskites

The first report on halide perovskite was in 1893, but it started to draw attention in the 1990s.[13, 14] Due to the optical and electrical properties, the halide perovskites were expected as materials for LEDs and transistors. In early 2010, with the high absorption coefficient and carrier mobility, the halide perovskites were widely used in photovoltaic fields and achieved over 20% of power conversion efficiency for now.[15] An enormous amount of research has been conducted on halide perovskite photovoltaics and the deep understand on the halide perovskites were enabled. Based on these understandings, the perovskite LEDs have also made great strides.

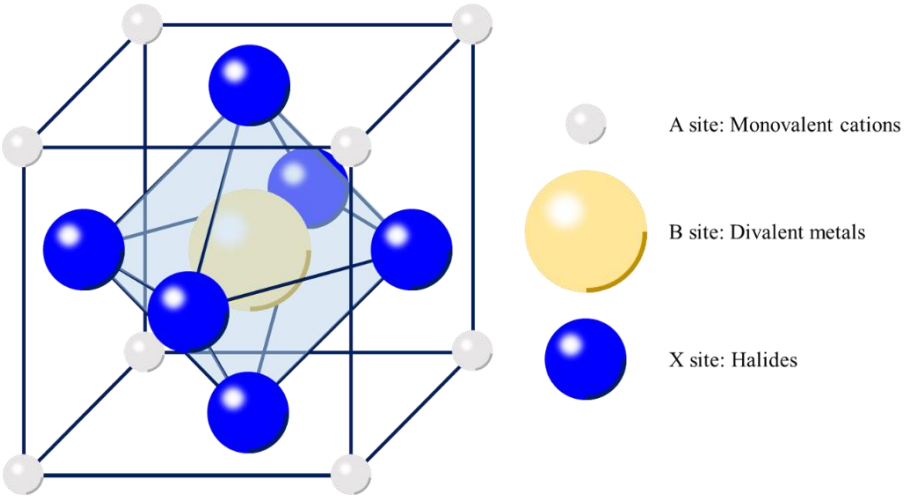

Figure 2.1. Structure of the halide perovskite.

The halide perovskite is a material that has ABX_3 formation and perovskite structure. The perovskite structure is shown in the **Figure 2.1**. The perovskite structure is similar to the face-centered-cubic

structure with additional atom at the body center. Usually, monovalent organic and/or inorganic cation is used for the A site; methyl ammonium (MA), formamidinium (FA), Rb, and Cs are mainly used. For the B site, divalent metals are used. Most of the halide perovskites are using the Pb for the B site. Due to the toxicity of the Pb, attempts have been made to replace the Pb with Sn. For X site, halides are used; I, Br, and Cl.

There are various possible combinations to form the halide perovskite, but for cubic structure, the size of components should be considered. With the effective ionic radii of components at A, B, and X sites in the perovskite as R_A, R_B, and R_X, respectively, the Goldschmidt tolerance factor (t) and the octahedra factor (μ) determines the formation of stable cubic structure.

$$t = (R_A + R_X)/\sqrt{2}(R_B + R_X) \tag{2-1}$$

and

$$\mu = R_B/R_X \tag{2-2}$$

To make perovskite-like structures, μ should be between 0.44 and 0.9 and the t should be in the range from 0.8 to 1.11. In detail, if the t value is in the range of from 0.8 to 0.89, the structure becomes distorted and forms rhombohedral, orthorhombic, or tetragonal structure. To obtain clear cubic structure, the t value should be in the range of from 0.9 to 1.[16, 17] The possible combinations with general variations and there expected structures are shown in **Figure 2.2**.

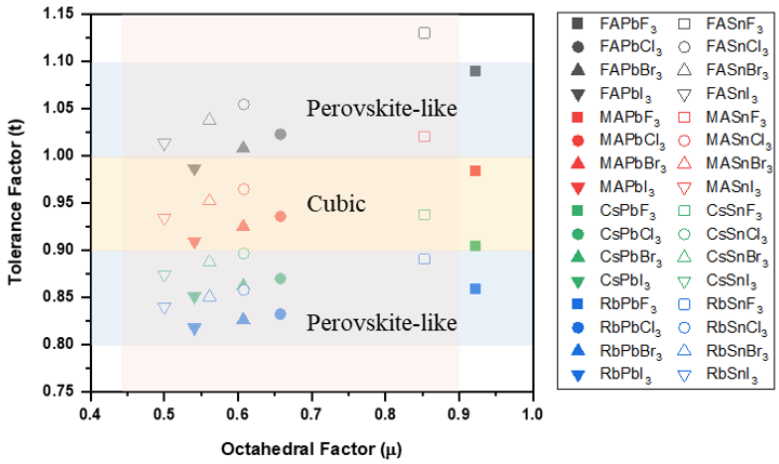

Figure 2.2. Calculated tolerance factor and octahedra factors for combinations of commonly used halide perovskite components.

If the perovskite structure is successfully constructed, most of the halide perovskite materials present great optoelectrical properties, such as high carrier mobility, high absorption coefficient, high photoluminescence quantum yield (PLQY), easily tunable optoelectronic bandgap, defect tolerant, long carrier lifetime and diffusion length, light weight, low price, and solution processability. These special properties were come from the peculiar band structure of halide perovskite. The band structure around the bandgap is constructed from the orbitals of halides and Pb atoms.[18] The conduction band is constructed from the Pb atom and the valence band is constructed from the halides with partial contribution of Pb atoms. The A site components usually participates deep inside of the valence band and rarely have effect on the bandgap. Therefore, the bandgap size is easily tuned by controlling the halides ratio in the halide perovskites. By tuning of bandgap, the optical bandgap of halide perovskite covers wide range from near IR region to near UV region (i.e. from ~2 eV of $CsPbI_3$ to ~3 eV of $CsPbCl_3$). Additionally, the A site components have less direct effect on the bandgap but change the lattice parameter or create crystal distortion, so bandgap of the halide perovskite could be tuned in small scale. This bandgap tunability enabled the desired color of emission covering all visible wavelength region.

Moreover, the electronic trap states from the defects of the halide perovskite are generated at shallow level of the bandgap. Due to the lack of deep trap states, the halide perovskites have very low non-radiative recombination rates, which is connected to the high PLQY property. Furthermore, the halide perovskites have narrow emission spectra and high color purity, which is necessary property for the next generation displays. The low formation energy is another advantage of the halide perovskites. With ow formation energy, the halide perovskite easily crystallized even at room conditions and solution processing methods.

These advantages made halide perovskites as strong candidate for next generation display material, but there are remaining problems. One of the problems is low exciton binding energy. With the low exciton binding energy, the carriers prefer flow in the crystals than recombine and create the photons and impedes device efficiency. The advantage of low formation energy has another aspect, that causes easily produced ionic defects. At the surface of the halide perovskites, the ionic defects are more easily generated with existence of humidity. These ionic defects sites act as non-radiative recombination centers and damages device efficiency. The produced ionic defects are origin of the low stability of halide perovskites and eventually leads halide perovskites to be destroyed.

Interestingly, the ionic defects are mobile in the halide perovskite crystals. The mobile halide defects can be interpreted as, in other words, the mobile halides. Because of this mobile property of the halide, the halide exchanging post treatments have been researched. By just supplying the different type of the halide to the halide perovskite, the halides in the perovskite starts to be exchanged spontaneously. The

halide exchanging method is additional technique to obtain the desired optoelectronic properties, and widely used to get red or blue emission, which requires mixed halide perovskites.

On the other hand, the mobile property of halides in the halide perovskite causes problem known as halide segregation. In the mixed halide perovskites, the well mixed halides tend to segregate and forms ununiform phases in the material because of the entropy reason. The halide segregation is spontaneous phenomena in the halide perovskite and causes emission peak shifts of the LEDs. Moreover, the halide segregation becomes worse under higher current density condition, which is unavoidable situation for highly efficient devices. Recently, the attempts to suppress the halide segregation have been conducted and the halide perovskites with mixed A site suffer less from the halide segregation, but there should be more advances to obtain stable highly efficient PeLEDs.

2.2 Properties of halide perovskite nanocrystals

The halide perovskite nanocrystals (PeNCs) are single crystals with size of few nanometers. Most of these PeNCs are wrapped with the organic ligands, which prevents severe ionic defects and enhance the stability and optoelectronic properties. Because of small size, the PeNCs show better electronic band structure. In the case of PeNCs, the electronic trap states are not created at shallow level but created inside of the conduction/valence bands. Because of this characteristic, the PeNCs are called as defect tolerant. The defect tolerant does not mean the PeNCs are free from the defects, rather that defects have low effect on the material. The small size has another fancy effect, the quantum confinement effect. If the size of nanocrystal is smaller than the exciton Bohr radius, the quantum confinement effect occurs.[19] By the quantum confinement effect, the bandgap of the PeNCs can be increased and this is another way to tune the bandgap of halide perovskites.

Most of advantages of the halide perovskites were maintained, however there are differences from the organic ligands in the PeNCs. Importantly, the exciton binding energy of the PeNCs is increased due to the electrically insulating ligands confines the charge transport behavior. The increased exciton binding energy directly enhances the radiative recombination rates, because of this most of PeNCs shows higher PLQY result than the bulk halide perovskites. The PeNCs are dispersed in the organic solvents due to the organic ligands and could be used with solution processing methods. Unlike the usual bulk halide perovskites, the PeNCs solutions are hydrophobic and have more choices of interlayers. In past decades, great advances happened in the OLED and QLED fields, with advanced interlayers. The PeNCs can directly apply those advanced interlayers to fabricate the PeLEDs which is hard for the bulk halide perovskite.

The first synthesis of PeNCs was reported by the Protesescu et al. in 2015.[20] Then various researches on synthesis, treatments, and device applications were published. The typical synthesis of the PeNCs was based on the hot-injection method, which was well known and widely used method in the quantum dot fields. The hot-injection method has advantages of yielding nanoparticles with uniform size and the size of the nanoparticles is easily controlled. With the existing knowhow of the hot-injection method, the size and shape of the PeNCs could be freely controlled. The properties of synthesized PeNCs could be enhanced with post synthetic treatments. Through the post-treatments, such as ligand exchange or halide exchange, the optoelectronic properties were tuned to desired purposes. With the development of post-treatment methods, the PLQY of the PeNCs is getting close to the 100%, and the devices with these nanocrystals achieved more than 10% of external quantum efficiency of PeLEDs.

2.3 Synthesis of halide perovskite nanocrystals,

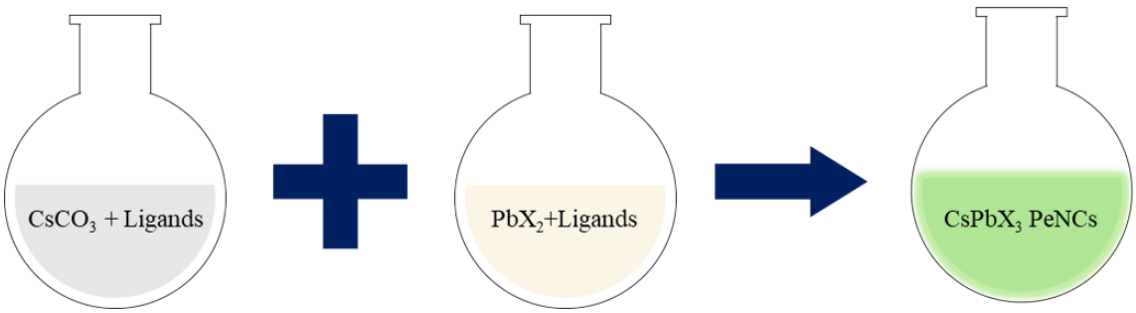

Figure 2.3. Scheme of the synthesis of $CsPbX_3$ PeNCs.

In this thesis, the PeNCs were synthesized through the typical hot-injection method. To provide better understand, usual synthetic steps of $CsPbX_3$ PeNCs are described below (**Figure 2.3**). Overall synthetic process is simple, mixing Cs precursor with PbX_2 precursors. In detail, the Cs precursor is the Cs-oleate, prepared by reaction between Cs_2CO_3 and oleic acid (OA) in octadecene (ODE). With 100 ℃ of heat and vacuum condition, the Cs_2CO_3 reacts with oleic acid and resulting colorless and transparent Cs-oleate solution, and CO_2 and H_2O which are removed by the vacuum. Then the Cs precursor is kept under Ar atmosphere at 120 ℃ until used. The PbX_2 precursor is prepared by mixing PbX_2, oleic acid (OA) and oleyl amine (OAm) ligands in ODE solvent. When using the $PbCl_2$ precursor, due to the low solubility of the $PbCl_2$, the trioctylphosphine (TOP) ligands are additionally used to support the dissolution. The PbX_2 precursor solution is heated up to 120℃ under vacuum to form Pb-oleate and oleylammonium halides. When the formation is done, the PbX_2 precursor solution become yellowish transparent state. Then the PbX_2 precursor is heated up to desired temperature under Ar atmosphere, and this temperature called injection temperature. When the PbX_2 precursor solution reached injection temperature, the Cs precursor is swiftly injected to the PbX_2 precursor solution. After few seconds, the $CsPbX_3$ PeNCs are formed, and the PeNCs solution is cooled down to room temperature with an ice bath. The synthesized pristine PeNCs solution is purified by precipitation and redispersion steps with centrifugation to remove the remaining unreacted precursors. In this procedure, the anti-solvent, such as alcohols or ethers, are optionally used to get pure PeNCs.

In the synthesis process, various parts have effect on the property of the PeNCs. The shape of the PeNCs could be controlled by selecting different type of ligands. The amount of ligand has effect on the perovskite size. Usually, the more ligands lead more nucleation and smaller mean size of PeNCs. The injection temperature governs the mean size of the PeNCs. The higher injection temperature leads less nucleation and faster reaction, resulting bigger PeNCs. Generally, it is known that the growth time influences size distribution of the nanoparticles in quantum dot fields. However, due to the low

formation energy of the halide perovskite, the formation of the PeNCs is done in few seconds, and the growth time has less effect on the size distribution of the PeNCs. The synthesized PeNCs are dispersed in general organic solvents such as chlorobenzene (CB), chloroform (CF), toluene (Tol), hexane, or octane.

2.4 Structure of PeLEDs

The PeLEDs consists of the emissive layer between two electrodes with charge transport layers. Typical structure of the PeLEDs is shown in **Figure 2.4**.

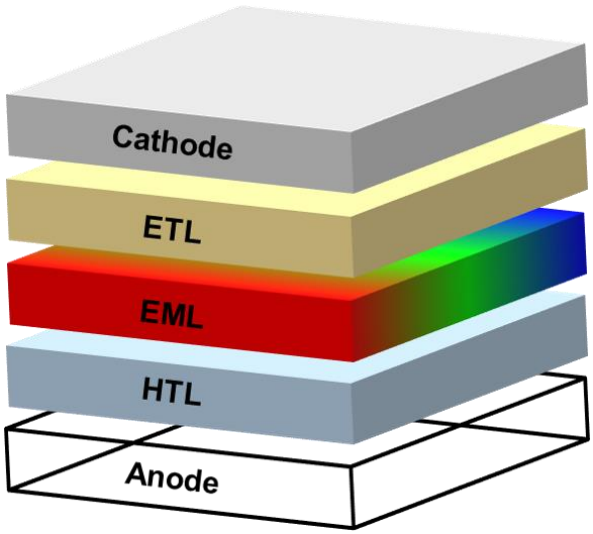

Figure 2.4. Structure of the PeLEDs device.

The PeLEDs consist of the emissive layer (EML), anode, cathode, electron transport layer (ETL), and hole transport layer (HTL). For EML, the halide perovskites with desired emission spectra are used, both bulk perovskite and PeNCs are widely used. For an efficient charge injection, metal cathode with low work function (WF) is used. For anode, transparent electrodes such as indium tin oxide (ITO) or fluorine doped tin oxide (FTO) are used. To improve the device performances, usually charge transport layers are introduced to the devices. The ETL reduces the energy barrier between cathode and emissive layer and block the hole flow from the EML to cathode. The HTL works similarly, reducing energy barrier between anode and emissive layer and block the electrons. With the charge transport layers, more opportunities are given for the charges that have not yet been recombined to be recombined at the EML. Moreover, due to the difference of mobilities of holes and electrons, the charge injection balance is usually out of proportion. With control of ETL and HTL, the mobility of the charges could be tuned, and charge injection balance and related device performance could be improved.

2.5 Operating mechanism of PeLEDs

The light, generated by the PeLEDs, is converted from the charges, which follows below 4 steps.

(1) Charge injection
(2) Charge transport
(3) Recombination
(4) Emission

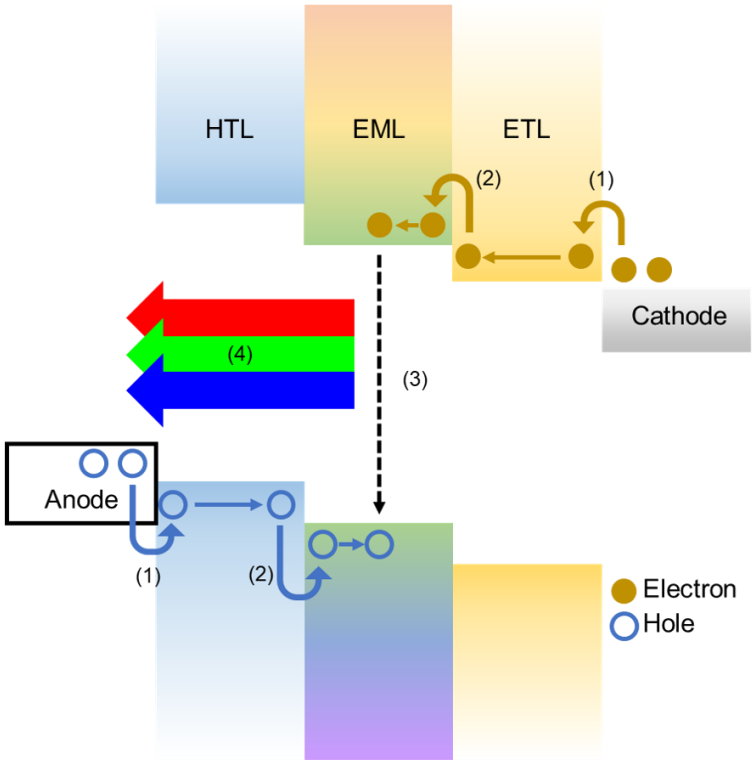

Figure 2.5. Operational mechanism of PeLEDs.

When the voltage is applied to the PeLED, electrons and holes are injected from the electrodes to the charge transport layers. The electrons are injected from the cathode to the ETL, while the holes are injected from the anode to the HTL. The injected electrons are transported to the conduction band of the EML, and the holes are transported to the valence band or the EML. Then the charges are recombined and coupled at emissive layer, forming excitons. Then, the excitons release the energy and converted to photons.

(1) Charge injection

For an efficient electron injection, the low WF electrodes, such as calcium (WF: 3.2 eV), magnesium (WF: 3.7 eV), and LiF/Al (WF: 4.1 eV) are usually applied for the cathode. For similar reason, the ITO (WF: 4.7 eV) and FTO (WF: 4.6 eV) are widely used for the anode to inject hole and used as a transparent electrode that does not interfere the emitted light. Typically, to inject charges, there are energy requirement to over the barrier at the interface. The energy requirement is related to the energy gap between the electrodes and charge transport layers or EML. Therefore, matching the energy levels of layers in the devices is key point of highly efficient PeLEDs.

(2) Charge transport

When the voltages are applied to the device, electrons and holes drift to its opposite electrodes from the injected electrodes. Charge transport layers helps these charges to reach the EML. In many cases, the mobility for electrons and holes are different and causes unbalanced charge injection. Not only efficiency reduction but even also recombination at charge transport layers could be occurred by the charge injection unbalance. Therefore, control of charge mobility in the device and balancing the charge injection should be carried out.

(3) Recombination

The efficiency of the PeLEDs depends mainly on the recombination of charges, which were injected and transported from the electrodes. More opportunity of recombination results more production of the excitons and photons. To make more recombination rates, the charge transport layers act as blocking layers for single carriers. The ETLs are act as hole blocking layer and the HTLs are act as electron blocking layer, then the charges are confined to be recombined at the EML and increases the recombination rates. To avoid non-radiative recombination rates, low trap state density of EML is required for highly efficient PeLEDs.

(4) Emission

There are two type of excitons created by the recombination, singlet and triplet excitons. It is known that when the excitons are generated there are 25% chance of creating singlet exciton and 75 % chance of creating triplet exciton. The halide perovskites have fluorescent property and only singlet excitons have contribution to generate the photons. The energy of emitted photons is determined by the given energy of excitons. Generally, the emitted energy is determined by the bandgap of the material of EML.

2.6 Characterizations of PeLEDs

Turn-on voltage

The schematic band diagram for the PeLEDs with different applied bias is shown in **Figure 2.6**. Carrier injection will not occur in reverse or low forward bias due to the energy barrier between electrodes and EML. When the applied voltage equals to the difference between the WFs of anode and cathode, flat band condition occurs. At the flat band condition, the charges start to be injected and this sis the minimum voltage required for the charge injection, called as turn-on voltage ($V_{turn\text{-}on}$). However, practically, the exact electronic energy levels of the materials are hard to precisely measure and could be affected too many variables. Therefore, in many cases, the turn-on voltages are determined as the applied voltage with minimum detectable brightness (usually ~ 0.1 cd/m^2), and this determination is applied to in this thesis. With this determination, the turn-on voltage could be affected by the charge transport behavior of the device and/or the recombination rates of the EML. If the charge injection or the radiative recombination is disturbed, the turn-on voltage increases to reach the minimum brightness. Thus, devices with lower turn-on voltage is near to the ideal device.

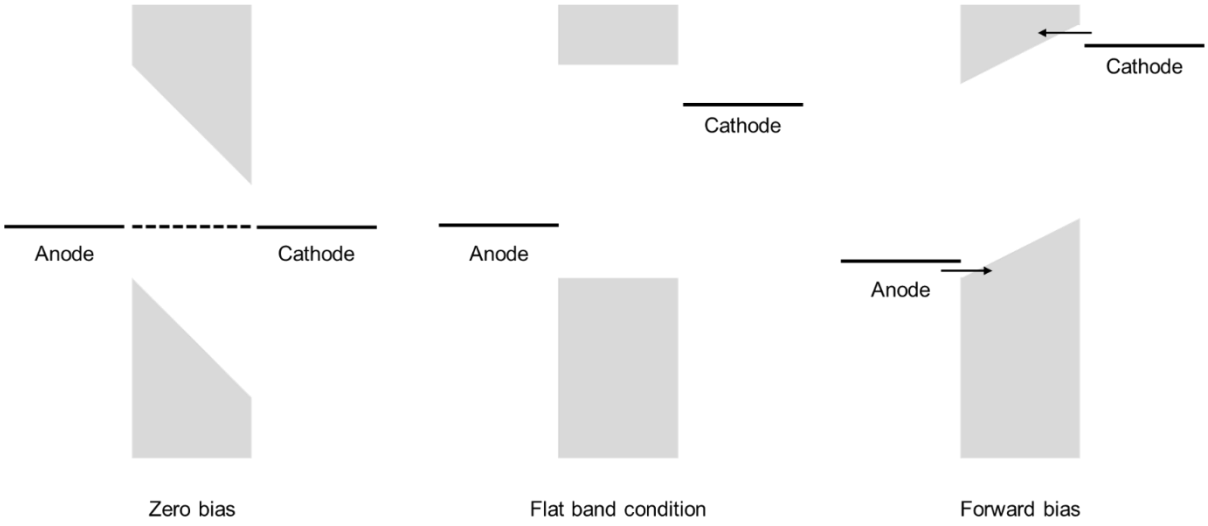

Figure 2.6. Schematic band diagram of PeLEDs with different applied bias.

Device efficiency

The most common factor to characterize the device is the device efficiency. The internal quantum efficiency (IQE) and the external quantum efficiency (EQE) are often used to evaluate how PeLEDs effectively emit the light. The IQE (η_{int}) is the ratio of generated photons of PeLEDs from injected charges, and determined as following equation.

$$\eta_{int} = \gamma \zeta_s q \tag{2-3}$$

where γ is ratio of exciton formulation event, ζ_s is ratio of singlet exciton generation event, and q is ratio of radiative recombination rate of singlet excitons.

The EQE is the ratio of generated photons of PeLEDs into the viewing direction from the injected charges, and determined as following equation

$$\eta_{ext} = \eta_O \cdot \eta_{int} \tag{2-4}$$

where η_O is the outcoupling efficiency, which indicates light extraction efficiency into the viewing direction, and depends on the total internal reflection states. With a classical reflection and refraction theory, η_O can be expressed as

$$\eta_O = 1/(2n^2) \tag{2-5}$$

where *n* is refractive index of the material that generated photons should pass.

The current efficiency (CE) is another term for examine the efficiency of the PeLEDs. The CE is determined as luminance (*L*) of PeLEDs with the current density (*J*) of the device.

$$CE = L/J \tag{2-6}$$

with a unit of cd/A.

Luminance

The luminance of the PeLEDs is the value of the luminous intensity per unit area into the viewing direction. With monochromatic light with ideal case, the luminance (*L*) can be determined as

$$L = \frac{\Phi}{\pi} \tag{2-7}$$

where the Φ is the luminous flux and can be expressed as

$$\Phi = K_m \cdot \int_0^\infty y(\lambda)\Phi_{e,\lambda}(\lambda)d\lambda \tag{2-8}$$

where the K_m is maximum luminosity factor (683.002 lm/W), y(λ) is the luminosity function at wavelength λ determined by the human eye photopic function. And $\Phi_{e,\lambda}(\lambda)$ is the spectral radiant

flux.

Color coordinates and color purity

To express the color in the color space, the emission spectrum of PeLED *S(λ)* could be translated into numbers with following equations

$$X = K\int_{380}^{780} S(\lambda)\bar{x}(\lambda)d\lambda \quad (2\text{-}9)$$

$$Y = K\int_{380}^{780} S(\lambda)\bar{y}(\lambda)d\lambda \quad (2\text{-}10)$$

$$Z = K\int_{380}^{780} S(\lambda)\bar{z}(\lambda)d\lambda \quad (2\text{-}11)$$

where $\bar{x}(\lambda)$, $\bar{y}(\lambda)$, and $\bar{z}(\lambda)$ are the color matching functions, which is sensitivity of human eye to each wavelength. The *K* is determined to be calculated *Y* becomes to equal value to the luminance. Then, the X, Y, and Z values are called as CIE1931-XYZ value. Then the color coordinates (x, y) of the PeLED in the color space are defined as

$$x = \frac{X}{X+Y+Z} \quad (2\text{-}12)$$

$$y = \frac{Y}{X+Y+Z} \quad (2\text{-}13)$$

Then, the color purity (P_e) can be represented as

$$P_e = \frac{x-x_n}{x_d-x_n} \quad (2\text{-}14)$$

$$P_e = \frac{y-y_n}{y_d-y_n} \quad (2\text{-}15)$$

where (x, y) is the color coordinates of testing PeLEDs, (x_d, y_d) is the color coordinates boundary monochromatic wavelength of dominant wavelength of PeLEDs, and (x_n, y_n) is the color coordinates of the achromatic center.

CHAPTER 3. High Performance Perovskite Light-Emitting Diodes with Surface Passivation of $CsPbBr_xI_{3-x}$ Nanocrystals via Antisolvent Triggered Ion-exchange

The content of this chapter is published in *ACS Applied Materials and Interfaces*, **2020**, 12(28), 31582-31590.

3.1 Research background

Lead halide perovskites (LHPs)[21, 22] possess tremendous opto-electrical properties such as tunability of the band gap, high color purity with sharp full-width at half maximum (FWHM) and photoluminescence quantum yield (PLQY) which adequate to be intensively promising material for optoelectronic and display applications.[23-30] Recently, LHPs based optoelectronic device such as solar cells and light-emitting diode (LED) have achieved commercial level performance.[10, 31] Although a LHPs based device recorded high level of performance, there are some factors need to be settled for commercialization in market needs. Due to the low stability of LHPs material, all-inorganic LHPs $CsPbX_3$ was studied for the chemically stable Cs cation using in LHPs $CsPbX_3$. Furthermore, to increase the enthalpy energy of the LHPs, nanocrystals (NCs) $CsPbX_3$ (X = Cl, Br, or I) form have been intensively studied due to its superior stability against to moisture and thermal.[32-34] However, $CsPbX_3$ NCs are more ionic compared with other chalcogenide quantum dots, thereby dynamic bonding characteristics between the surface and capping ligands can occur ligand loss.[35-37] Detached organic capping ligands from the NCs surface can induce surface defect states and resultant rapid drop of colloidal stability in NCs which finally cause the fatal effects in device application. Moreover, induced defects in perovskite NCs also allow triggering reversible phase transition.[38, 39] Thus, it has been reported that capping ligands are closely connected with the NCs surface defect states. Therefore, the study on introduction of ligand engineering is still wandering to minimize surface defect states.

The red-emitting perovskite nanocrystals (PeNCs) aiming to present 620 ~ 650 nm emission wavelength could be synthesized by combination of bromide and iodide halide anions, which inducing an unsteady state of perovskite material, $CsPbBr_xI_{3-x}$ NCs especially among several $CsPbX_3$ NCs owing to substitution of iodide halide anions. Larger ionic radius of iodide and resultant weaker bonding strength of Pb-I lead lattice distortion or strain, partially structural degradation, and defect sites caused by mentioned unfavorable effects.[40-42] They can act as defect-related nonradiative recombination site,

and deteriorate electrical and physical properties. Therefore, for superior quality of PeNCs, suppressing unintended defect states should be surmounted.

Here, we demonstrated a high quality $CsPbBr_xI_{3-x}$ NCs together with high stability against to moisture and superior optical property via a ligand mediated post-treatment (LMPT) method with halide ion-pair ligand, tridodecylmethyl ammonium iodide (TrDAI). From green-emitting $CsPbBr_3$ PeNCs, ionized iodide halide anions from TrDAI ligand are surrounded to the PeNCs and $TrDA^+$ cations capped $CsPbBr_xI_{3-x}$ NCs are spontaneously occurred as diffusion induced anion exchange in PeNCs.[43-46] Through this surface passivation by ion exchange, the impedimental defect states can be filled up by excess ionic residuals which lead to the longer PL lifetime and outstanding optical properties 88.7% of PLQY in comparison olelyamine (OAm) and oleic acid (OA) ligands on CsPbBrxI3-x NCs 56.7% of PLQY. Moreover, the effect of surface treatment of LMPT not only increased the quality of PeNCs but also increased the materials stability. TrDAI ligand treated- $CsPbBr_xI_{3-x}$ NCs display surpassing colloidal stability against to humidity alongside low loss in optical property and sturdy perovskite lattice without structural degradation or phase transition even though it is kept in air for 7 days under humidity up to 70%. These outstanding results induced the high performance and stable PeLEDs. Thus, the optimized TrDAI ligand treated- $CsPbBr_xI_{3-x}$ NCs based PeLEDs exhibit a maximum CE of 7.69 cd/A and an EQE of 6.36% that is tenfold higher that of reference device at 637 ± 2 nm emission wavelength with a sharp FWHM of 31 nm.

3.2 Experimental details

Synthesis of $CsPbBr_3$ Nanocrystals: Synthesis of $CsPbBr_3$ perovskite nanocrystals (PeNCs) followed the method of Protesescu et al. with scale modification.[20] In a usual synthesis, 1.47 mmol of lead bromide ($PbBr_2$) and 40 mL of octadecene (ODE) were placed in a 100 mL three-neck flask and dried under a vacuum for 1 h at 120 °C. 4 mL of oleic acid (OA) and 4 mL of oleylamine (OAm) were added to lead halide solution, then the temperature was raised to injection temperature, 160 °C and kept under Ar atmosphere. 3.2 mL of previously synthesized Cs-oleate (0.163 g of cesium carbonate (Cs_2CO_3) in 8 mL of ODE and 0.5 mL of OA degassed for an hour and kept under Ar atmosphere with a temperature increase to 120 °C immediately prior to injection) was swiftly injected. After 5 s, the PeNCs solution was quickly cooled to room temperature with an ice bath. After then, the crude solution was precipitated via centrifugation at 8000 rpm for 15 min, and the precipitated PeNCs were re-dispersed in 5 mL of toluene. One more purification step with butanol (BuOH) was needed. After adding 5 mL of BuOH, solution was centrifugated again at 12000 rpm for 10 min, and separated precipitate was finally dispersed in 10 mL of toluene. For ligand exchange step, tridodecylmethyl ammonium iodide (TrDAI), 50 μL of OA was added in 0.5 mL of the $CsPbBr_3$ PeNCs under vigorous stirring, and then TrDAI ligand solution was added. 3 mL of BuOH was injected in the mixture solution and centrifugated at 12000 rpm for 10 min to purify, then re-dispersed in 0.5 mL of toluene.

Device Fabrication: Indium tin oxide (ITO) substrates were cleaned in deionized water, acetone, and isopropyl alcohol (IPA) using ultra-sonication and dried in an oven. After treating with ozone with 30 min, PEDOT:PSS solutions were spin coated onto the ITO substrates at 3000 rpm for 40 s, followed by annealing at 150 ℃ for 15 min. After cooling down, the substrates were transferred into a nitrogen glovebox, where Poly(N,N'-bis-4-butylphenyl-N,N'-bisphenyl)benzidine (Poly-TPD) solution (8 mg/mL in chlorobenzene) and $CsPbBr_xI_{3-x}$ NCs (7 mg/mL in toluene) were deposited by spin-coating. Thermal annealing at 140 ℃ for 20 min was needed before $CsPbBr_xI_{3-x}$ NCs solution was spin coated. Finally, 2,2',2''-(1,3,5-Benzinetriyl)-tris(1-phenyl-1-H-benzimidazole) (TPBi) (50 nm), LiF (1 nm), and Al (100 nm) were thermally deposited sequentially under high vacuum ($<10^{-6}$ Torr). The active area of the device was 13.5 mm^2.

Characterization

UV-Vis-NIR Absorption and Photoluminescence (PL) Measurements

UV-Vis NIR absorption spectra were obtained by using a Cary 5000 (Agilent) spectrophotometer and the photoluminescence spectra were measured with an nF900 instrument (Edinburgh Photonics) with a xenon lamp as an excitation source.

Photoluminescence quantum yield (PLQY)

The PLQY values were obtained with QE-2000 from Otsuka Electronics Co., Ltd.

Transmission Electron Microscopy (TEM)

Transmission Electron Microscopy (TEM) images were recorded by using JEM02100 and JEM-2100F from JEOL. The samples which were washed with butanol one time and re-dispersed in toluene dropped onto carbon coated Cu grids from Ted Pella, Inc.

Time-correlated single-photon counting (TCSPC)

Time-resolved and steady-state PL spectra were measured by using FluoTime 300. The samples were photoexcited with a 510 nm continuous wave and pulsed diode laser head (LDH-D-C-510). The PL decay curves were fitted to a biexponential decay model using software, FluoFit.

X-ray Photoelectron Spectroscopy (XPS)

X-ray Photoelectron Spectroscopy (XPS) spectra were obtained using a Thermo Fisher Scientific EXCALAB 250XI at a $1.0*10^{-9}$ Torr based pressure with a monochromated Al-Kα X-ray source.

Fourier Transform Infrared Spectroscopy (FTIR)

Fourier Transform Infrared Spectroscopy (FTIR) spectra were performed using a Cary 670 FTIR spectrometer (Agilent).

High Power X-Ray Diffraction (XRD)

XRD patterns were obtained by using a high-power diffractometer (D/MAX2500V/PC from Rigaku) with settings including 40 kV potential, 200 mA current, Cu-rotating anode, Cu Kα radiation, (λ = 0.1542 nm) using a graphite monochromator and a scintillation counter.

Device Measurement

The electroluminescence (EL) spectra and J-V-L characteristics of LED device were collected with a Keithley 2400 source measurement unit and a Konica Minolta spectroradiometer, CS-2000 (Minolta). The measurements were conducted in the air with encapsulation.

3.3 Result and discussion

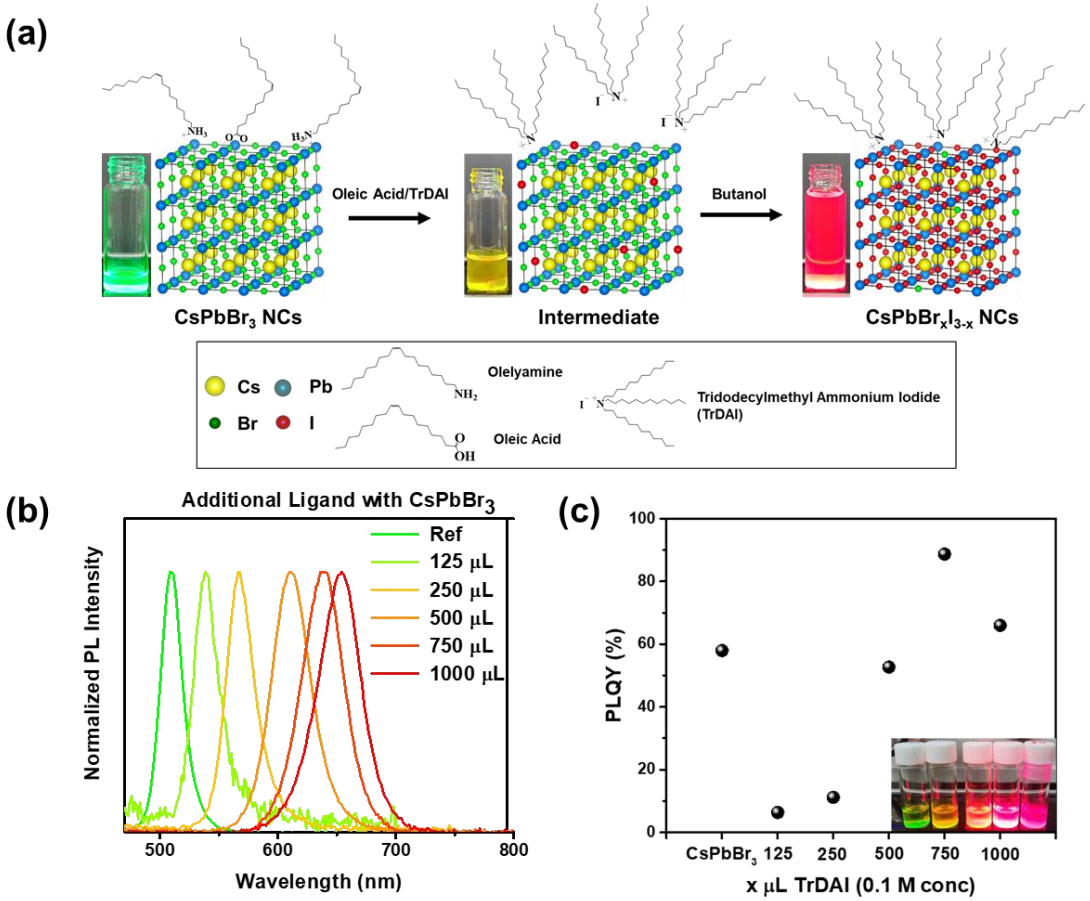

Figure 3.1. (a) Schematic of ligand exchange process and chemical structure of ligand material. And optical properties along with treating the ligand, TrDAI for 0.46 wt % concentration $CsPbBr_3$ NCs; (b) Photoluminescence (PL) spectra and (c) PL quantum yield of TrDAI treated perovskite NCs were washed with butanol first and re-dispersed in toluene. (Inset is photograph of TrDAI treated perovskite NCs with under λ = 365 nm UV excitation)

In this work, PeNCs were synthesized using the commonly reported hot-injection method with long insulating ligands with OAm and OA for capping the PeNCs surface. And then, TrDAI was exchanged to the attached original ligand OAm and OA for the controlling the PeNCs' properties and passivating the surface defects of the PeNCs.[47] This method was commonly used and named as LMPT method which can dissociate the iodide halide ions from TrDAI ligand to the perovskite core. However, the solvent with LMPT method critically affect the exchanged PeNCs quality. Therefore, we systemically studied with polar and non-polar solvent with TrDAI ligand as shown in **Figure 3.1a**.[48, 49] The dissolved solvent according to polarity for TrDAI was particularly considered due to successfully ionizing TrDAI ligand into tridodecylmethyl ammonium ($TrDA^+$) cation and iodide (I^-) anion. Here, we studied the impact of polar solvents according to polarity on LMPT reaction owing to alcohol soluble TrDAI ligand.

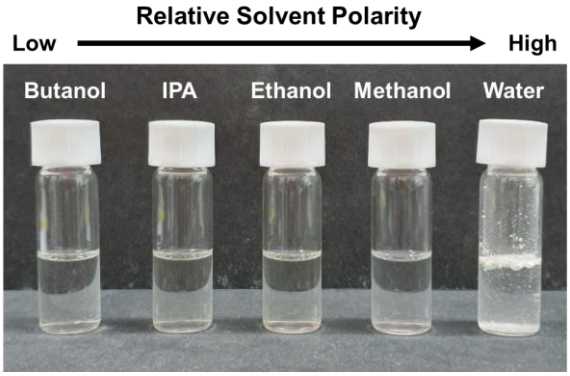

Figure 3.2. Images of TrDAI ligand solution dissolved in different polar solvents; butanol, iso-propyl alcohol (IPA), ethanol, methanol, and water.

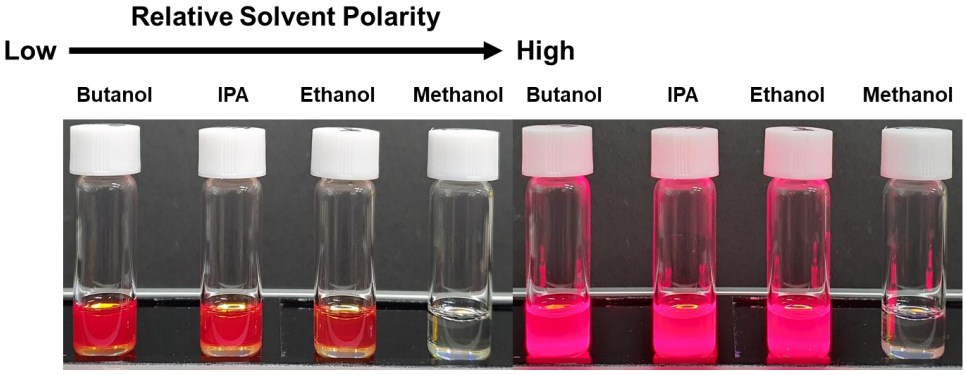

Figure 3.3. Images of TrDAI treated $CsPbBr_xI_{3-x}$ NCs solution were washed with different polar solvents first and re-dispersed in toluene.

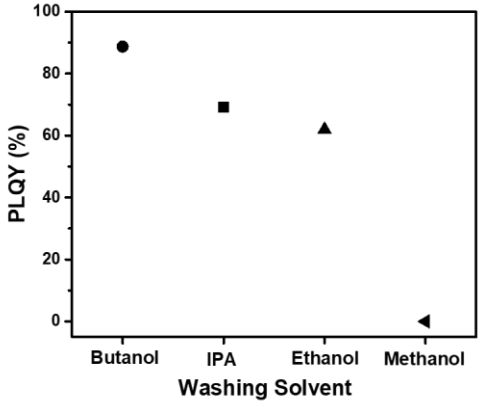

Figure 3.4. Photoluminescence quantum yield of TrDAI treated $CsPbBr_xI_{3-x}$ NCs were washed with different polar solvents first and re-dispersed in toluene.

As shown in **Figure 3.2**, TrDAI ligand is well dissolved in polar solvents; butanol, iso-propyl alcohol

(IPA), ethanol, and methanol, and bright red-emitting PeNCs at 640 nm emission wavelength were shown with synthesized PeNCs except methanol (**Figure 3.3**). Among the TrDAI dissolved solvents, butanol displays outstanding colloidal stability and bright luminescence with highest PLQY of 88.7% (**Figure 3.4** and **Table 3.1**).

Dispersion Solvents	**Butanol**	**IPA**	**Ethanol**	**Methanol**
PLQY (%)	88.74	69.27	61.96	0

Table 3.1. Summarized photoluminescence quantum yield values of TrDAI treated $CsPbBr_xI_{3-x}$ NCs were washed with different polar solvents first and re-dispersed in toluene.

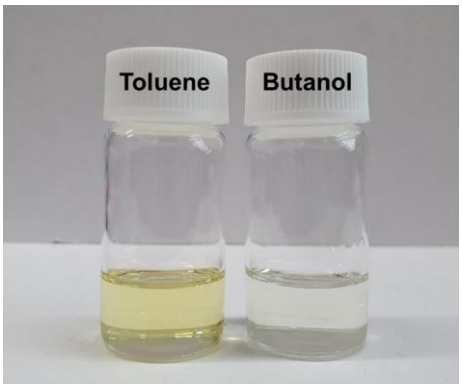

Figure 3.5. Images of TrDAI ligand solution dissolved in toluene (Left) and butanol (Right).

These results directly indicate that the mild property of polar solvent butanol can be a suitable for destabilizing anti-solvent which can also act as a purification solvent through the simple injection step during a LMPT process in this work (**Figure 3.5**). The disconnected fewer I^- anion was passivated PeNCs surface which can enhance the PLQY. And the other ionized materials $TrDA^+$ cations ligand from TrDAI was adsorbed onto the surface of NCs. Solvent in perovskite colloidal system is particularly critical factor, and it can cause damage in surface and surface trap states by ligand loss owing to dynamic binding between the surface ligands and ionic characteristic of PeNCs. Thus, the purification and dispersion solvent are closely connected with characteristic of NCs surface and capping ligand, and choosing them is important.

The optical properties of OA and OAm capped $CsPbBr_3$ NCs were also easily tuned by controlling the amount of TrDAI ligand with LMPT method. As the increased amount of TrDAI ligand from 125 μL to 1,000 μL, the amount of free iodide halide anions were generated which can induce the self-exchanged into CsPbBr3 NCs core. **Figure 3.1b** shows the shifted the photoluminescence (PL) peak position toward the red region from 508 to 653 nm with the TrDAI ligand amount control into $CsPbBr_3$

NCs. As expected, the photoluminescence quantum yield (PLQY) of LMPT treated PeNCs was also enhanced with from 57% to 88% at 750 μL TrDAI ligand condition, which come from halide anion surface passivation effects as explained above (**Figure 3.1c**). However, with low amount of TrDAI ligand 125 and 250 μL conditions, LMPT treated PeNCs PLQY values were dramatically decreased. This phenomenon came from insufficient capping of $TrDA^+$ cation ligand surrounding nanocrystals under low amount of TrDAI since the surface of PeNCs detached original OAm and OA capping ligand points were not fully covered by low amount of $TrDA^+$ cation resulting in surface defects. Thus, inferior colloidal stability and low PLQY values caused by surface defects were severely observed in a colloidal unsteady state during purification step with butanol.[50]

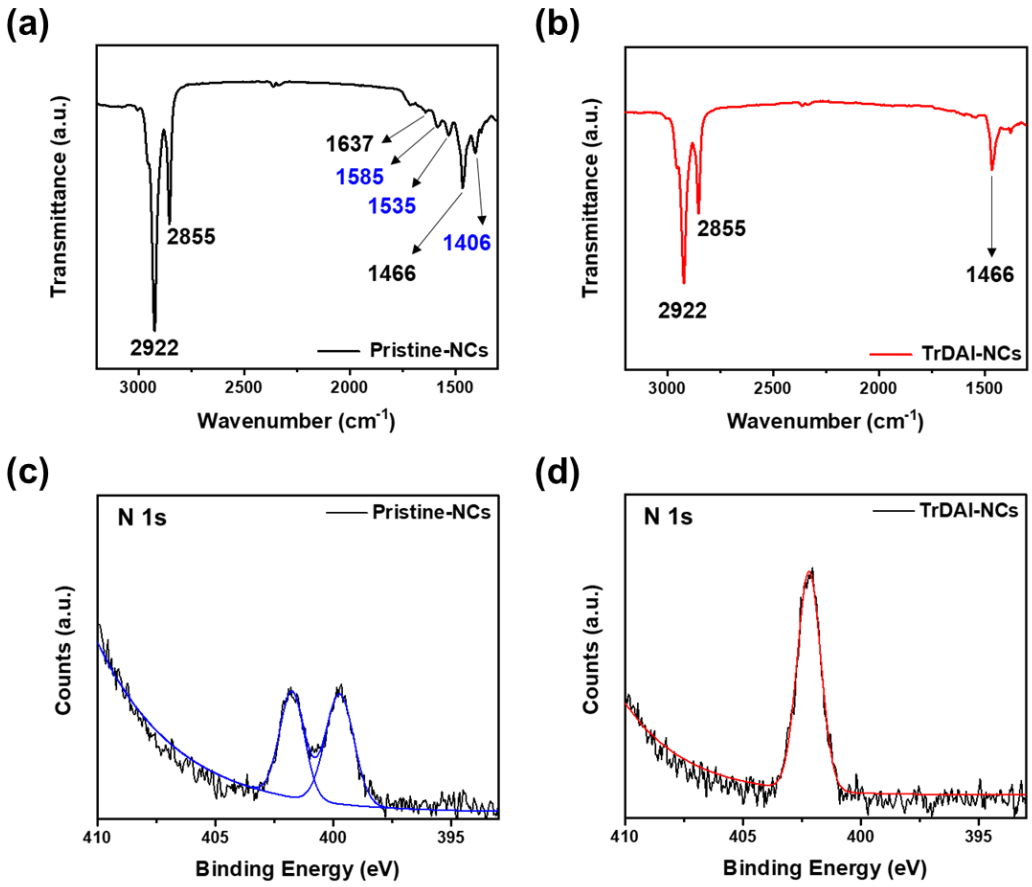

Figure 3.6. (a, b) Fourier transform infrared (FTIR) spectra and (c, d) X-ray photoelectron spectroscopy (XPS) spectra corresponding to N 1s core-level peak of Pristine- and TrDAI treated- $CsPbBr_xI_{3-x}$ NCs.

The successful exchange confirmation of LMPT with TrDAI ligand on PeNCs, the Fourier transform infrared spectroscopy (FTIR) measurement was conducted to investigate the TrDAI ligand exchange process from OA and OAm ligand. After exchange with TrDAI ligand, OA and OAm ligand were detached on PeNCs surface. Therefore, we measured FT-IR with pristine- $CsPbBr_xI_{3-x}$ NCs and TrDAI ligand treated- $CsPbBr_xI_{3-x}$ NCs. **Figure 3.6a** and **b** show the pristine-NCs and TrDAI-NCs respectively

which show the different peak position around 1700 ~ 1300 cm^{-1}. Both PeNCs has the common peaks at 2922 cm^{-1} and 2855 cm^{-1} respectively which indicate the CH_2 symmetric and asymmetric stretching vibrations, respectively. And the peak at 1466 cm^{-1} represents the CH_2 bending vibration, which are usual peaks with hydrocarbon groups. The peaks at 1585, 1535 and 1406 cm^{-1} could be assigned as two asymmetric and one symmetric stretching vibrations of the carboxylate group ($-COO^-$) which indicate the presence of the oleate ligand at the surface of the pristine- $CsPbBr_xI_{3-x}$ NCs (**Figure 3.6a** and **b**).[51, 52] In addition to the OA ligand, the peak at 1637 cm^{-1} could be explained as the asymmetric NH^{3+} deformation from the OAm ligand.[53] These peaks were only shown in the pristine- $CsPbBr_xI_{3-x}$ NCs while they were disappeared in the TrDAI ligand treated- $CsPbBr_xI_{3-x}$ NCs, interpreting the desorption of the OA and OAm ligand from the surface of the PeNCs. Furthermore, X-ray photoelectron spectroscopy (XPS) spectra corresponding to N 1s core-level peak were obtained to identify the presence of the OAm ligand which supporting the FTIR results (**Figure 3.6c** and **d**). For the pristine- $CsPbBr_xI_{3-x}$ NCs, there are two peaks at 401.8 eV and 399.8 eV which signifying the protonated amine groups ($-NH^{3+}$) and the amine groups ($-NH^2$) respectively. These peaks are the evidence of the amine group of the OAm that is originally attached at the surface of the pristine- $CsPbBr_xI_{3-x}$ NCs. On the other hand, TrDAI ligand treated- $CsPbBr_xI_{3-x}$ NCs have only one peak at the 402.2 eV corresponding to the tert-ammonium cation from TrDAI ligand, along with elimination of the OAm ligand at the surface of the NCs during the ligand exchange process.[54] FTIR and XPS spectra results prove that the OA and OAm ligand completely exchanged to the TrDAI ligand.

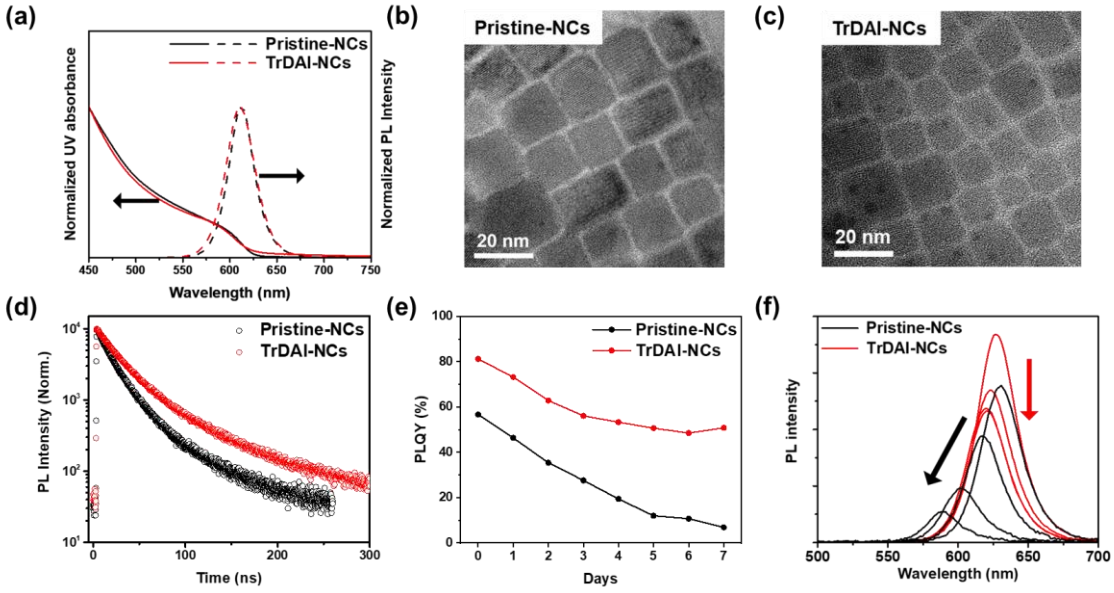

Figure 3.7. (a) Photoluminescence (dashed) and UV-vis absorbance (solid) spectra and (b, c) Transmission electron microscopy (TEM) images of Pristine- and TrDAI treated- $CsPbBr_xI_{3-x}$ NCs. (d) Time-resolved PL lifetime at detection wavelength of 640 nm of synthesized perovskite NCs solution in toluene. Solution stability of $CsPbBr_xI_{3-x}$ NCs; (e) PLQYs and (f) Photoluminescence spectra of the as-prepared Pristine- and TrDAI treated- $CsPbBr_xI_{3-x}$ NCs solution just synthesized and after being kept

in air for 7 days with RH up to 70%.

To directly compare the properties between pristine-$CsPbBr_xI_{3-x}$ NCs and treated LMPT method with TrDAI ligand, the same peak position of PL was studied. The ratio of bromide to iodide was controlled for corresponding to synthesized pristine-$CsPbBr_xI_{3-x}$ NCs and TrDAI ligand treated $CsPbBr_xI_{3-x}$ PeNCs. **Figure 3.7a** showed PL and UV-vis absorption spectra of pristine- and TrDAI treated- $CsPbBr_xI_{3-x}$ NCs with a narrow FHWM of ~ 32 nm. After ligand exchange OAm and OA to TrDAI ligand, transmission electron microscopy (TEM) images still display cubic phase of PeNCs maintained without having any surface damage or structural distortion during LMPT process (**Figure 3.7b, c**). In addition, from **Figure 3.7c**, lattice distance value, 0.642 Å of TrDAI treated- $CsPbBr_xI_{3-x}$ NCs was increased compared to general $CsPbBr_3$ NCs lattice spacing of 0.595 Å, offering proof that TrDAI iodide anions were self-exchanged into a $CsPbBr_3$ NCs during a LMPT process.[55, 56] The geometrical characteristics are confirmed and proved through the measured X-ray diffraction (XRD) patterns corresponding to TEM images as shown in **Figure 3.8**. We measured XRD patterns with pristine-NCs and TrDAI-NCs. Both them show the strong diffraction peaks at 14.6° and 29.5° which indicating cubic phase of PeNCs with (100) and (200) directions, respectively. And we calculated the particle's size distribution and its uniformity from TEM images. The size distribution histograms for pristine-NCs and TrDAI-NCs were exhibited in **Figure 3.9**. The pristine- $CsPbBr_xI_{3-x}$ NCs showed average particle size of 14.15 nm while the TrDAI treated- $CsPbBr_xI_{3-x}$ PeNCs, it showed similar average particle size of 13.51 nm. These results confirmed that LMPT method does not damage PeNCs size and properties.

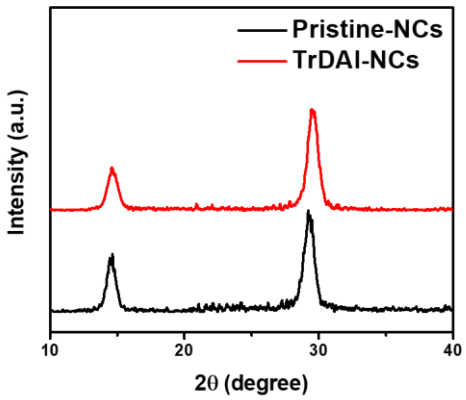

Figure 3.8. X-ray diffraction patterns of the as-prepared Pristine- and TrDAI treated- $CsPbBr_xI_{3-x}$ NCs films.

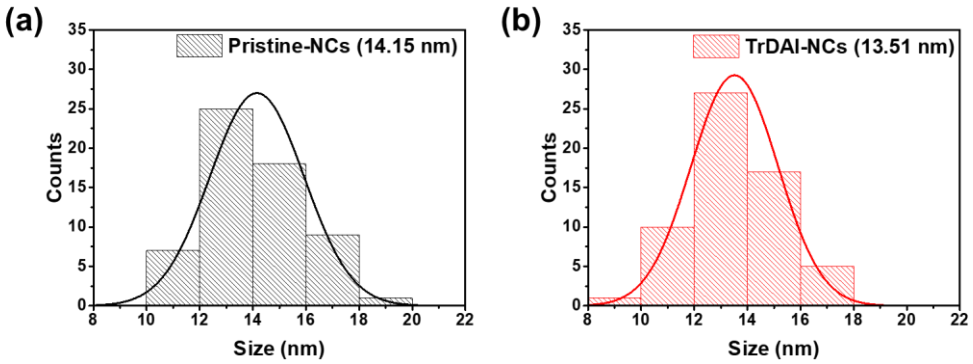

Figure 3.9. Size distribution histograms for the as-synthesized (a) Pristine- and (b) TrDAI treated-$CsPbBr_xI_{3-x}$ NCs.

To confirm the effect of TrDAI-NCs compared to pristine-NCs, a time-correlated single-photon counting (TCSPC) measurement for PL decay was conducted to confirm how the TrDAI ligand treatment affects the PeNCs PL lifetime, and decay curves were fitted to the biexponential model (**Figure 3.7d**). In **Table 3.2**, the measured biexponential fitting parameters are summarized, the average PL lifetime of the PeNCs distinctly increased after the TrDAI ligand exchange process from 20.77 ns to 31.52 ns. This result is well-matched with the measured PLQY data of pristine- and TrDAI treated-$CsPbBr_xI_{3-x}$ NCs, indicating that dissociated iodide halide anions from TrDAI ligand contributes greatly to surface defect states passivation and improvement of optical properties (**Figure 3.10**).

Nanocrystals	τ_1 **(ns)**	f_1 **(%)**	τ_2 **(ns)**	f_2 **(%)**	τ_{ave} **(ns)**	χ^2
Pristine-NCs	15.28	81.07	44.28	18.93	20.77	1.12
TrDAI-NCs	21.72	78.71	67.77	21.29	31.52	1.03

Table 3.2. Summarized biexponential fitting parameters for time-resolved PL lifetime of Pristine- and TrDAI treated- $CsPbBr_xI_{3-x}$ NCs solution in toluene; f_1 and f_2 are percent contributions of lifetimes, fast-decay τ_1 and slow-decay τ_2 respectively.

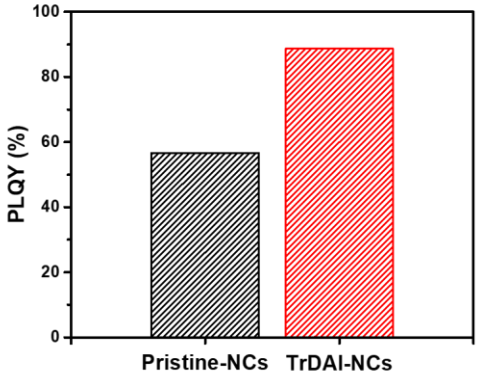

Figure 3.10. Photoluminescence quantum yield of Pristine- and TrDAI treated- $CsPbBr_xI_{3-x}$ NCs were washed with butanol first and re-dispersed in toluene.

The size of halide ion is according to I > Br > Cl order which is also correlated to the perovskite structure stability with decomposition energy.[57] In the mixed perovskite, $CsPbBr_xI_{3-x}$ NCs, the substituted iodine ions have a larger ionic radius than bromine which induces the decrease of decomposition energy owing to weaker bond strength of Pb-I.[40, 58] Thereby, $CsPbBr_xI_{3-x}$ NCs contain mixed halides of iodine and bromine ions have low material stability which can lead decomposition of the perovskite lattice with residue of lead iodide (PbI_2) and cesium iodide (CsI), resulting in rapid drop of PLQY and phase transition. Moreover, $CsPbBr_xI_{3-x}$ NCs degraded to α-phase of $CsPbBr_3$ due to strong bonding of Pb-Br by the following mechanism:

$$3CsPbBr_xI_{3-x} + H_2O \rightarrow CsPbBr_3(\alpha) + CsOH + 2PbI_2 + CsI + HI \quad (3\text{-}1)$$

As Zhang et al. reported, the perovskite decomposition mechanism (3-1), the perovskite NCs surface defect vacancy can induce the perovskite structure stability.[42] Therefore, the efficient surface passivation of PeNCs is critical point to increase the PeNCs stability. We carefully studied the PeNCs humidity stability by statically measured PLQY values of the as-prepared pristine- and TrDAI treated- $CsPbBr_xI_{3-x}$ NCs solution for 7 days in air with humidity up to 70% condition in **Figure 3.7e**. As expected, just synthesized TrDAI ligand treated and optimized $CsPbBr_xI_{3-x}$ NCs exhibited the strikingly enhanced PLQY value than pristine- $CsPbBr_xI_{3-x}$ NCs from 56.7% to 88.7% via halide surface passivation effect. The PLQY is germane to material's defect states and charge recombination in the material, and the measured PL lifetime result proves this optical property enhancement. In case of pristine- $CsPbBr_xI_{3-x}$ NCs, the PLQY value is rapidly decreased to 6.8% within 7 days following structural destruction through above mentioned degradation mechanism, and noticeable difference of $CsPbBr_xI_{3-x}$ NCs solution color is confirmed to the naked eye as shown in **Figure 3.11**.

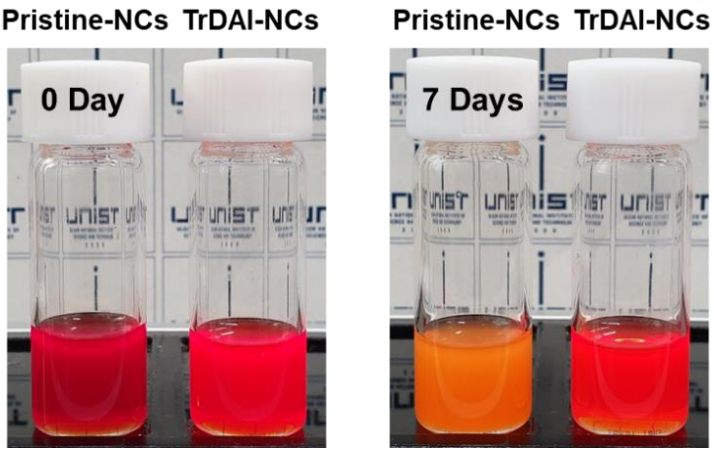

Figure 3.11. Images of Pristine- and TrDAI treated- $CsPbBr_xI_{3-x}$ NCs solution just synthesized and after being kept in air for 7 days with RH up to 70%.

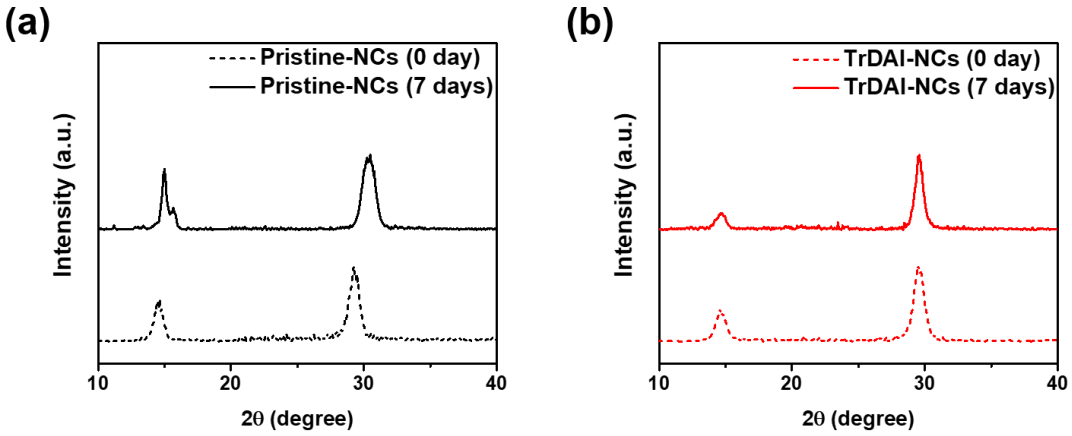

Figure 3.12. X-ray diffraction patterns of the as-prepared (a) Pristine- and (b) TrDAI treated- $CsPbBr_xI_{3-x}$ NCs solution just synthesized and after being kept in air for 7 days with RH up to 70%.

The PL spectra of pristine- $CsPbBr_xI_{3-x}$ NCs stored in air for 7 days showed blue-shifted PL peak position with approximately ~ 64 nm (**Figure 3.7f**). This blue-shifted PL peak position directly tells that above mentioned $CsPbBr_xI_{3-x}$ mixed perovskite degradation mechanism. The strong Pb-Br bonding compared to Pb-I in mixed PeNCs is maintained under high humidity while $CsPbBr_xI_{3-x}$ perovskite lattice decomposed. And $CsPbBr_xI_{3-x}$ mixed perovskite finally goes to $CsPbBr_3$ phase with other residual materials. However, iodide halide passivated $CsPbBr_xI_{3-x}$ NCs with $TrDA^+$ ligand exhibit 50.8% of PLQY value after 7 days even though it stored in high humidity up to 70%. And then, the PL emission spectra corresponding to PLQY results exhibit nearly identical peak position with roughly ~ 4 nm. These phenomena clearly show that TrDAI ligand can be fully passivated of the $CsPbBr_xI_{3-x}$ NCs. The XRD patterns analysis also could verify and support the material structural and phase stability with the TrDAI

ligand exchange process (**Figure 3.12**). The pristine- $CsPbBr_xI_{3-x}$ NCs with OA and OAm ligand present shifted and split XRD patterns after 7 days owing to degradation of perovskite lattice, whereas the $CsPbBr_xI_{3-x}$ NCs with TrDAI ligand show still unwavering and sharp XRD patterns with cubic phase.

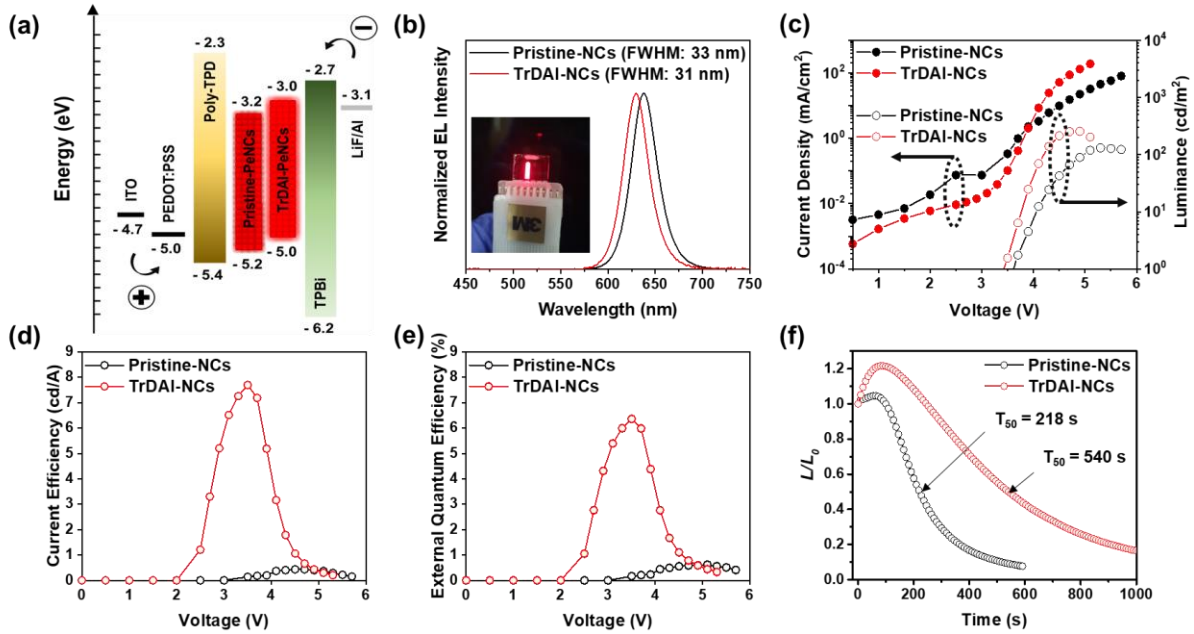

Figure 3.13. Optimized PeLEDs characteristics: (a) Band energy diagram of device, (b) electroluminescence, (c) *J-V-L*, (d) current efficiency, (e) external quantum efficiency, and (f) luminance decay of the device under a constant bias, 4.1 V with Pristine- and TrDAI treated- $CsPbBr_xI_{3-x}$ NCs as emitting layer.

We optimized the TrDAI ligand treated- $CsPbBr_xI_{3-x}$ NCs applicated PeLEDs with PEDOT:PSS and Poly-TPD as hole injection layer (HIL) and TPBi as electron injection layer (EIL). The as-prepared device is comprised of multiple layers in regular sequence; ITO, PEDOT:PSS, Poly-TPD, PeNCs, TPBi, and LiF/Al. The band energy diagram of optimized device structure is presented in **Figure 3.13**. The energy levels of pristine- and TrDAI ligand treated- $CsPbBr_xI_{3-x}$ NCs was calculated respectively by measuring Ultraviolet photoelectron spectroscopy (UPS) and UV-vis-NIR absorption. The UPS measurement was carried out to measure highest occupied molecular orbital (HOMO) energy levels (**Figure 3.14**). The LMPT PeNCs shows the about 0.2 eV higher than pristine PeNCs, meanwhile band gaps estimated from the Tauc plots exhibit similar values of approximately 2.02 eV in both PeNCs (**Figure 3.15**).

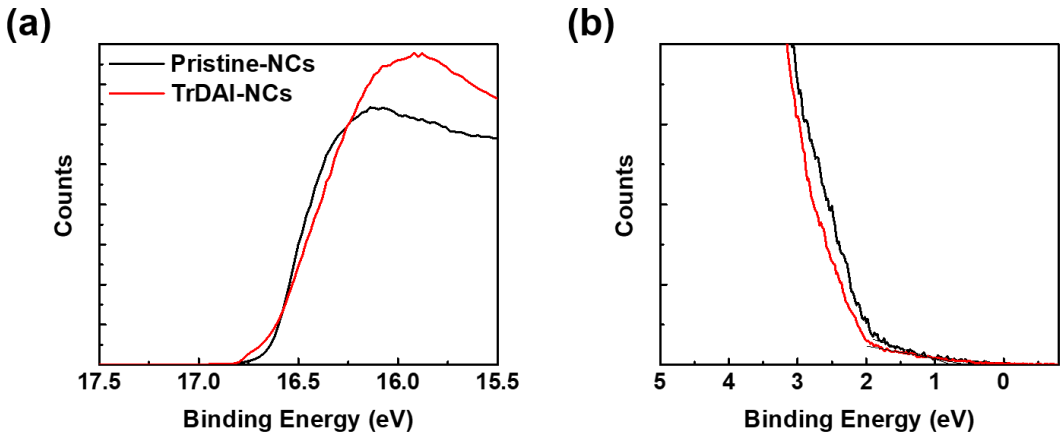

Figure 3.14. Ultraviolet photoelectron spectroscopy (UPS) spectra of Pristine- and TrDAI treated-CsPbBrxI3-x NCs; (a) secondary electron cutoff region and (b) valence band edge, plotted relative to an Au reference.

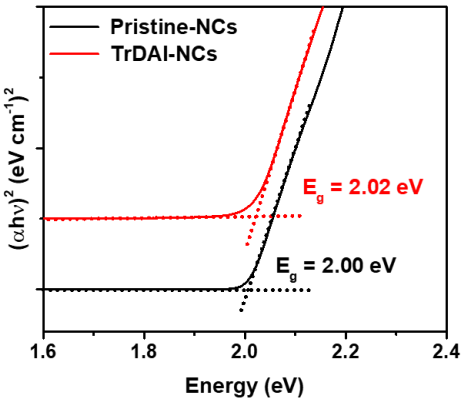

Figure 3.15. Tauc plots of Pristine- and TrDAI treated- NCs and measured optical band gaps are indicated.

In **Figure 3.12b**, the fabricated PeLEDs display electroluminescence peak between 630 and 640 nm with a narrow full width at half maximum (FWHM) of ~ 31 nm. The optimized PeLEDs with pristine-$CsPbBr_xI_{3-x}$ NCs exhibit a maximum current efficiency (CE) of 0.43 cd/A and an external quantum efficiency (EQE) of 0.61%. On the contrary, the PeLEDs performances with TrDAI ligand treated-$CsPbBr_xI_{3-x}$ NCs are outstandingly enhanced performance in comparison with the reference device. The device with TrDAI ligand treated- $CsPbBr_xI_{3-x}$ NCs yield a maximum CE of 7.69 cd/A and an EQE of 6.36% which is tenfold higher than that of the reference device. Detail optimized device characteristics are summarized in **Figure 3.12** and **Table 3.3**. Remarkably improved PeLEDs with TrDAI by LMPT method is mainly contributed to the halide surface passivation effect and efficient charge carrier collection in active layer between HIL and EIL by increased band energy. **Figure 3.12c** shows the one

order of magnitude smaller leakage current could be contributed to inefficient radiative recombination are of interest to the PeLEDs device engineering. As shown in **Figure 3.16**, we further compared both electron and hole current densities of pristine- and TrDAI ligand treated- $CsPbBr_xI_{3-x}$ NCs through electron- and hole- only device. Both electron- and hole- only device show the reduced injection voltage which also confirms the efficient charge transport with LMPT with TrDAI ligand. Furthermore, we measured the luminance decay of the pristine- and TrDAI ligand treated- $CsPbBr_xI_{3-x}$ NCs applicated PeLEDs under a constant bias of 4.1 V and recorded its half-lifetime (T_{50}) in terms of the device long-term stability (**Figure 3.12f**). The reference device shows T_{50} value of 218 s. However, the device with TrDAI shows the longer device stability with T_{50} value of 540 s. A LMPT method with TrDAI ligand makes efficient surface passivation of PeNCs and outstanding optical properties which mainly affect the PeNCs property. The enhanced PeNCs quality with TrDAI is critically contributed to the high PeLEDs performance and operating stability.

PeNCs	L_{max} [cd m^{-2}] @ bias	CE_{max} [cd A^{-1}] @ bias	EQE_{max} [%] @ bias	Turn-on Voltage [V] @ 0.1 cd m^{-2}
Pristine-NCs	130.83@5.3	0.43@4.5	0.61@5.1	3.5
TrDAI-NCs	255.32@4.9	7.69@3.5	6.36@3.5	2.9

Table 3.3. Summarized device performances of optimized PeLEDs with Pristine- and TrDAI treated-$CsPbBr_xI_{3-x}$ NCs as emitting layer; Device structure: ITO/PEDOT:PSS/Poly-TPD/PeNCs/TPBi/LiF/Al.

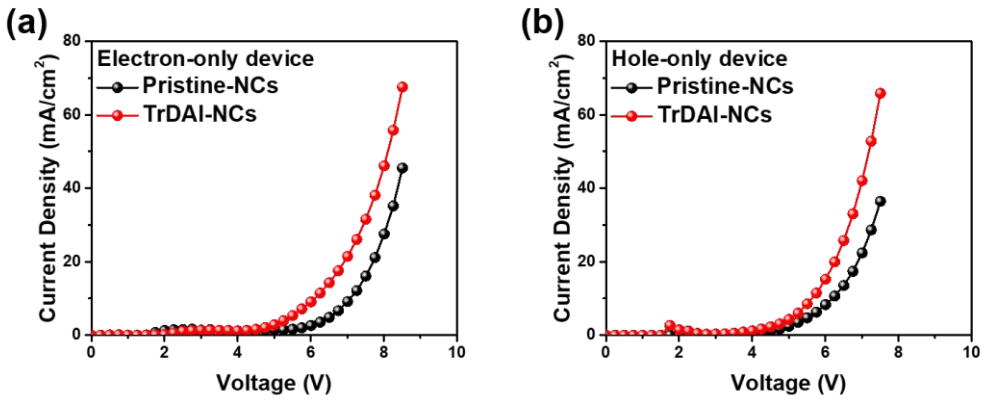

Figure 3.16. *J-V* curves of the (a) electron- and (b) hole-only devices with Pristine- and TrDAI treated-$CsPbBr_xI_{3-x}$ NCs.

3.4 Conclusion

In summary, we have successfully synthesized indefective and structural sturdy $CsPbBr_xI_{3-x}$ NCs via a ligand-mediated post-treatment (LMPT) method with tridodecylmethyl ammonium iodide (TrDAI), and applicated in LED devices. In PeNCs system, surface defect could be directly connected with material stability and resultant lagged optical properties. Moreover, distorted perovskite lattice and point defect occurred by separate halide ionic size and bonding strength with Pb in mixed halide system can induce the rapid structural degradation and the consequent decrease in optical properties. Through the iodide ion surface passivation strategy using a halide ion-pair ligand, TrDAI, the surface trap sites are efficaciously passivated alongside the longer carrier lifetime, allowing the bettered optical properties and structural stability of the PeNCs. In addition, lowered capping ligand density and effective radiative recombination in emitting layer as well as high quality of PeNCs result in dramatical enhancement of the device performance, achieving a maximum CE of 7.69 cd/A and an EQE of 6.36% which is approximately 10-fold high than that of reference device.

CHAPTER 4. Reversible, Full Color Luminescence by Post-treatment of Perovskite Nanocrystals

The content of this chapter is published in *Joule*, **2018**, 2(10), 2105-2116.

4.1 Research background

Hybrid organic-inorganic perovskite-based optoelectronic devices such as photovoltaics and light-emitting diodes have been intensively studied in recent years and achieved remarkably good performance.[59-61] $CsPbX_3$ (X = Cl, Br, I) perovskite nanocrystals (PeNCs) have unique and attractive properties such as the ability to tune their band energies via control of their halide compositions as well as via quantum confinement effects by controlling the size of PeNCs.[20] By adjusting the ratio of halide atoms (Cl, Br, I)in PeNCs, their band gaps can be easily modulated, allowing photoluminescence (PL) emission spectra to be tuned throughout the visible wavelength region from 400 nm to 800 nm.[62, 63] Furthermore, halide PeNCs have the advantage of high photoluminescence quantum yield (PLQY) and narrow emission peak width, which are desirable for light emitting diodes and display applications.[43, 64-69]

Post-treatments, where anions may be exchanged after nanocrystal synthesis, offer the ability to fine-tune nanocrystal compositions and have been introduced as a method to achieve full color spectral emission.[70-73] Parobek et al. reported an anion exchange method by exposure of PeNCs to ultraviolet (UV) light.[74] However, this approach only demonstrated applicability within a limited range of compositions (between Br and Cl). Additionally, exposure to UV light limited the uniformity of the reaction due to the high absorption coefficient of perovskite materials in the UV region. For solution-state anion exchange of $CsPbX_3$ PeNCs, treatment with solutions containing an excess concentration of the desired anion is a general approach to accomplish anion exchange in PeNCs. However, PeNCs are easily altered or destroyed due to their unstable surfaces and highly ionic properties. Generally, post-treatments of PeNCs rely on polar solvents to dissolve anions. However, polar solvents tend to fundamentally alter the nanocrystal structures and result in diminished PL intensity and altered peak positions.[50]

Haloalkane solvents are potentially excellent solvent for ion exchange due to their nonpolar characteristics and minimal effect on PeNCs structures; however, their non-polar characteristics lead to limited solubility of ionic halide sources. Haloalkane solvents, which contain halogen atoms,

additionally offer the unique potential to provide a convenient and abundant source of halide anions, however, the strength of covalent carbon-halogen bonds makes haloalkanes inert as halide sources under typical ion exchange conditions.

In this work, we have discovered, for the first time, a fully reversible ($CsPbCl_3 \rightleftharpoons CsPbBr_3 \rightleftharpoons CsPbI_3$) post-treatment method of anion exchange for $CsPbX_3$ (X = Cl, Br, I) PeNCs using haloalkane solvents, which is facilitated by the presence of a nucleophile. Haloalkane solvents were used as halide sources in combination with nucleophilic phosphine ligands to dissociate the halogen-carbon bond. Trioctylphosphine (TOP) performed the role of a strong nucleophile, facilitating an S_N2 chemical reaction to produce halide anions[75] as well as functioning as an organic ligand.[76, 77] Through fine control of the post-treatment conditions during anion exchange, we have achieved nanocrystals with fine-tunable luminescence, which covers the full visible spectrum from 400 nm ~ 700 nm. These materials were successfully used to fabricate vivid red, green, blue LED devices with outstanding color purity.

4.2 Experimental details

Materials

Following materials were purchased from Sigma-Aldrich: $PbBr_2$, $PbCl_2$, PbI_2, Octadecene (ODE), Oleic acid (OA), Cs_2CO_3, Toluene, Trichloromethane, Ethyl iodide, Trioctylphosphine, Acetonitrile. Oleylamine (OLAM) was purchased from Acros organics, while Tribromomethane and $PbBr_2$ were purchased from Alfa Aesar.

Nanocrystal synthesis

Synthesis of $CsPbX_3$ PeNCs followed an adaptation of the method of Protesescu et al.[20] at 5 times the scale. In a usual synthesis, 345 mg of $PbBr_2$ (0.94 mmol) (or 264/433 mg of $PbCl_2$/PbI_2, respectively) and 25 mL of ODE were placed in a 100 mL 3-neck flask and dried under a vacuum for 1 h at 120 °C. 2.5 mL of OA and 2.5 mL of OLAM were added to lead halide solution, then the temperature was raised to 150 °C (or 180 °C in the case of $CsPbCl_3$ synthesis) and kept under an Ar atmosphere. 2 mL of previously synthesized Cs-oleate (0.163 g of Cs_2CO_3 in 8 mL of ODE and 0.5 mL of OA degassed for an hour and kept under Ar with a temperature increase to 120°C immediately prior to injection) was swiftly injected. After 5 s, the NC solution was quickly cooled to room temperature with an ice bath. After synthesis, the NCs were purified via centrifugation at 4000 rpm for 10 min. After centrifugation of the NCs, they were re-dispersed in 3 mL of toluene at a concentration of ~70 mg/ml.

Anion exchange

PT-$CsPbBr_xCl_y$: The PeNCs solution (~70 mg/ml) was diluted 4-times with $CHCl_3$ and a desired volume of TOP was added. Due to the slow anion exchange rate, the solution was warmed to 60 °C to accelerate the reaction. The reaction time was adjusted to yield NCs with desired band gaps. After the target NC color had been reached, the reaction was quenched by precipitating into 6 volumes of acetonitrile. The precipitated NCs were collected by centrifugation (at 4000 rpm for 10 min) and re-dispersed in toluene.

PT-$CsPbBr_xI_y$: C_2H_5I was added to the PeNCs solution (~70 mg/ml) at 10 vol% and a desired volume of TOP was added. As $CsPbI_3$ PeNCs have weak stability, TOP should not be added at greater than 10 vol% for easy control, and the reaction must be quenched before the NCs change to the delta phase of $CsPbI_3$. Quenching and precipitation were carried out with the same procedure used in the chlorine exchange.

PT-$CsPbBr_yCl_x$ and PT-$CsPbBr_yI_x$: The PeNCs solution (~70 mg/ml) was diluted 2 times with $CHBr_3$ and a desired volume of TOP was added. Quenching and precipitation were carried out with the same procedure used in the chlorine exchange.

Device Fabrication

Device fabrication proceeded following an adaptation of the method reported by Pan et al.[43] Briefly, PEDOT:PSS solutions were spin-coated onto pre-cleaned, glass/ITO substrates at 3000 rpm for 40 s, followed by thermal annealing at 150 ℃ for 15 min in air. After cooling to ambient temperature, ligand-exchanged PeNCs $CsPbX_3$ or PT-$CsPbX_xY_y$ PeNCs were spin-casted at 2000 rpm for 60 s in an N_2-filled glove box. Finally, TPBi (50 nm), LiF (1 nm), and Al (100 nm) were deposited sequentially by thermal evaporation under a high vacuum ($<10^{-6}$ Torr).

Characterization

UV-vis absorption and photoluminescence (PL) measurements:

UV−vis absorption spectra were collected on a Cary 5000 (Agilent) and PL spectra were collected on an NF900 instrument (Edinburg) with a xenon lamp as an excitation source. The samples were diluted with toluene and prepared using 1 cm path length quartz cuvettes.

X-ray Photoelectron Spectroscopy (XPS):

Samples were prepared by spin-coating onto 80 nm thick gold films on Si substrates with a thin native oxide layer. XPS spectra were collected using a Thermo Fisher Scientific ESCALAB 250XI at a base pressure of 1.0×10^{-9} Torr with a monochromated Al-Kα X-ray source.

Device measurement:

LED measurements were performed using a Keithley 2400 source measurement unit and a Konica Minolta spectroradiometer (CS-2000, Minolta Co.).

Transmission Electron Microscopy (TEM):

Transmission Electron Microscopy (TEM) images were collected with JEM02100 and JEM-2100F from JEOL. The samples were prepared from solutions 2-times diluted with toluene and dropped onto carbon coated Cu grids from Ted Pella, Inc.

X-Ray Diffraction (XRD):

XRD samples were prepared in powder form by precipitation in acetonitrile and centrifugation. XRD patterns were measured using a high-power diffractometer (D/MAX2500V/PC from Rigaku) with settings including 40 kV potential, 200 mA current, Cu-rotating anode, Cu Kα radiation, (λ = 0.1542 nm) using a graphite monochromator and a scintillation counter. The instrument was operated from 10° to 60° with a step size of 0.02° (2θ).

Byproduct detection (NMR, FTIR):

Samples were prepared by taking supernatant solvent from centrifuged PT-$CsPbCl_3$ NCs. The supernatant was concentrated by heating at 80 °C, then diluted in $CDCl_3$. 1H nuclear magnetic resonance (NMR) spectra were collected on a VNMRS600 (Agilent) using $CDCl_3$ as solvent at room temperature. Fourier Transform-Infrared spectra (FTIR) were collected on a Cary 620 from Agilent in

ATR mode.

Photoluminescence quantum yield (PLQY):

The PLQY data were collected with QE-2000 from Otsuka Electronics Co., Ltd. The samples were diluted with toluene for a proper concentration to measure.

Calculation details

Density functional theory (DFT) calculation

We performed the density functional theory (DFT) calculations to investigate the role of TOP molecules on the dissociation of halogen atoms from haloalkane solvent molecules. All calculations were carried out using DMol^3 program[78, 79] in Material Studio with the 2017 R2 software version. Generalized gradient approximation (GGA) with Perdew-Burke-Ernzerhof (PBE) functional[80] was used for the exchange-correlation energy. All electron relativistic core treatments and 4.4 version of double numerical plus polarization (DNP) basis set were adopted to describe the core-electrons and the atomic orbital basis set, respectively. Spin-polarized calculations were employed for all model systems and van der Waals interaction between molecules was also considered by implementing Tkatchenko-Scheffler (TS) method.[81] The convergence criteria for the geometry optimization were 1.0×10^{-5} Ha for energy, 0.002 Ha/Å for force, and 0.005 Å for displacement, respectively. Note that the optimization was carried out in non-periodic boundary conditions (non-PBCs). All calculations were performed under implicit environment by using the conductor-like screening model (COSMO) method[82] with the dielectric constant of 1:1 mixture of $CHBr_3$ and $CHCl_3$ (C_2H_5I). Based on dielectric constants of $CHBr_3$,[83] $CHCl_3$,[84] and C_2H_5I[85] at 20 °C, we calculated the dielectric constant of 1:1 mixture of $CHBr_3$ and $CHCl_3$ (C_2H_5I) (*i.e.*, 4.595 ($CHBr_3$:$CHCl_3$ = 1:1) for $CHBr_3$ and $CHCl_3$ systems and 5.941 ($CHBr_3$:C_2H_5I = 1:1) for C_2H_5I system) through the mixing rule.[86]

To calculate the transition state (TS) of S_N2 reaction between TOP and haloalkane molecules, the complete single linear synchronous transit/quadratic synchronous transit (LST/QST) method[87, 88] was performed with 0.002 Ha/Å root mean square (RMS) convergence. This method firstly performed LST search on the reaction path between adjacent sites followed by conjugate gradient minimizations and subsequently QST maximization was followed. To calculate the accurate energy barrier, we repeated this methodology with TS optimization process until only one imaginary frequency was detected at TS.

The effect of TOP molecule on the dissociation of halogen atom was studied by calculating the changes of energy (ΔE) and Gibbs free energy (ΔG) of each system. ΔE was calculated by the energy difference to the referenced state for each system (*i.e.*, referenced state for the system of haloalkane; the state of converged point, and for the system of haloalkane with TOP; the initial state, as shown in **Figure 4.6**. ΔG of each system at T=20 °C was calculated by following equation,

$$\Delta G^{20\ ^\circ C} = \Delta H^{20\ ^\circ C} - T\Delta S^{20\ ^\circ C} \quad (4\text{-}1)$$

where, ΔH20 °C and ΔS20 °C indicates the changes of enthalpy and entropy from reference state, respectively. In addition, $\Delta G^{20\,^{\circ}C}$ can be expanded as,

$$\begin{aligned}\Delta G^{20\,^{\circ}C} &= H^{20\,^{\circ}C} - H_{ref}^{20\,^{\circ}C} - T(S^{20\,^{\circ}C} - S_{ref}^{20\,^{\circ}C}) \\ &= (U + PV) - (U_{ref} + P_{ref}V_{ref}) - T(S^{20\,^{\circ}C} - S_{ref}^{20\,^{\circ}C})\end{aligned} \quad (4\text{-}2)$$

where, U is the molar internal energy, P is the pressure, V is the molar volume, and S is the molar entropy, respectively. The subscript 'ref' indicates the reference state for each system. By introducing motional degrees of freedom (*i.e.*, vibration, rotation, and translation) and ΔE, the equation (S2) could be rewritten as follows,

$$\Delta G^{20\,^{\circ}C} = \Delta E + (U' + PV) - (U'_{ref} + P_{ref}V_{ref}) - T(S^{20\,^{\circ}C} - S_{ref}^{20\,^{\circ}C}) \quad (4\text{-}3)$$

where, $U' = E_{vib} + E_{trans} + E_{rot}$, and $U'_{ref} = E_{ref,\,vib} + E_{ref,\,trans} + E_{ref,\,rot}$. Note that all these terms are calculated once the system is optimized to the ground state.

Model systems

Three types of TOP configurations, depending on the orientation of the lone pair of electrons on phosphorus and direction of interaction with haloalkane molecules, were considered to find the optimal interaction configuration (**Figure 4.7**). The type I interaction, where the lone pair on the P atom stands out in front (away from octyl chains) to interact with haloalkane molecules (**Figure 4.9a**), was found to be the most stable configuration due to the favorable interaction energy.

4.3 Result and discussion

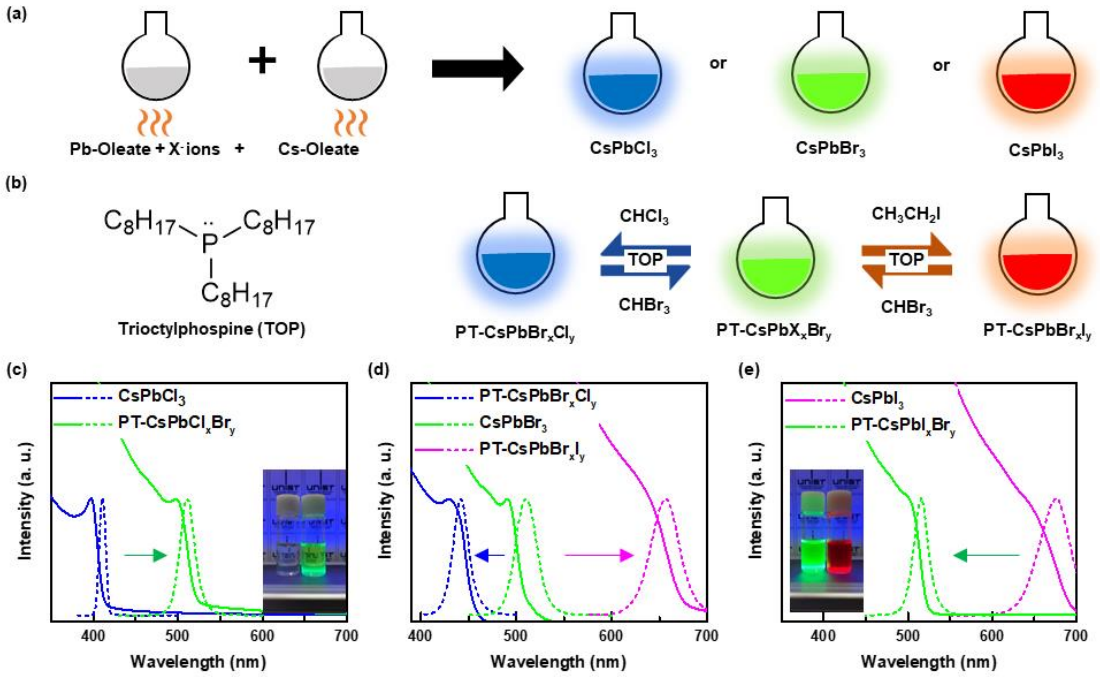

Figure 4.1. Schematic illustration of overall procedure and optical properties of anion exchanged perovskite Nanocrystals (NCs). (a), Schematic of the $CsPbX_3$ NCs synthesis and (b), haloalkane post-treatment using a nucleophile (TOP) for anion exchange of $CsPbX_3$ NCs. Absorption (solid line) and photoluminescence (dashed line) of anion exchanged NCs starting from (c), $CsPbCl_3$ to $CsPbBr_3$ NCs, (d), $CsPbBr_3$ to $CsPbCl_3$ or $CsPbI_3$ NCs, (e), $CsPbI_3$ to $CsPbBr_3$ NCs.

In detail, $CsPbX_3$ PeNCs were synthesized according to a previous method with scale modification,[20] then functionalized with organic ligands (oleic acid and oleylamine) allowing dissolution in nonpolar organic solvents such as trichloromethane, toluene, octane etc., followed by anion exchange. A brief schematic of the synthetic procedure of the PeNCs and anion exchange procedure is shown in **Figure 4.1**. The anion exchange generally proceeded as follows: A haloalkane solvent was added to the synthesized oleic acid : oleylamine decorated $CsPbX_3$ PeNCs to dissolve them, then TOP was added to the $CsPbX_3$ PeNCs / haloalkane solution to initiate the reaction. When TOP was added, anion exchange of the PeNC solution began spontaneously and was visible as a pronounced color change of the solution (Supplemental Movie), resulting in a solution of post-treated PeNCs with compositions described by the notation PT-$CsPbX_xY_y$, (where X represents the original halide, Y represents the new halide and the subscripts x and y represent the relative molar fraction of each halide. The sum of the subscripts x + y is 3 and x approaches zero while y approaches 3 as the reaction reaches completion). Because the nucleophilic substitution mechanism is well understood, we could easily control the reaction speed and responsiveness by adjusting the concentration of TOP, reaction time and temperature. Furthermore, we could easily terminate the reaction by precipitating the PeNCs with a suitable antisolvent. The solvent-

generated halide anions which formed upon adding TOP reactant spontaneously exchanged with the anions of the PeNCs as has been demonstrated in previous reports.[73, 89]

The anion exchange could be observed with the naked eye as a dramatic color change, corresponding to shifted absorption and PL peaks, respectively, as shown in **Figure 4.1c**, **d**, **e**. The changed optical properties are in excellent agreement with the optical properties of as-synthesized $CsPbCl_3$, $CsPbBr_3$, and $CsPbI_3$ PeNCs before anion exchange. For example, $CsPbCl_3$ PeNCs were synthesized and tribromomethane ($CHBr_3$) was added with TOP to yield PT-$CsPbCl_xBr_y$ PeNCs, as shown in **Figure 4.1c**. Likewise, $CsPbBr_3$ PeNCs were synthesized and trichloromethane ($CHCl_3$) or ethyl iodide (C_2H_5I) with TOP were added to make PT-$CsPbBr_xCl_y$ or PT-$CsPbBr_xI_y$ PeNCs, respectively, as shown in **Figure 4.1d**. $CsPbI_3$ PeNCs were synthesized and $CHBr_3$ was added with TOP to make PT-$CsPbI_xBr_y$ PeNCs, as shown in **Figure 4.1e**. The changed optical properties clearly demonstrate that through this simple solvent post-treatment method, the absorption onsets and visible emission spectra can be continuously tuned throughout the 400 nm ~ 800 nm spectral region, and the changes are fully reversible ($CsPbCl_3$ ⇌ $CsPbBr_3$ ⇌ $CsPbI_3$). Furthermore, the full width at half maxima (FWHM) of PeNCs PL spectra were not significantly broadened after any one of the anion exchanges, indicating that the solvent post-treatment reaction is not destructive to the PeNCs structures.

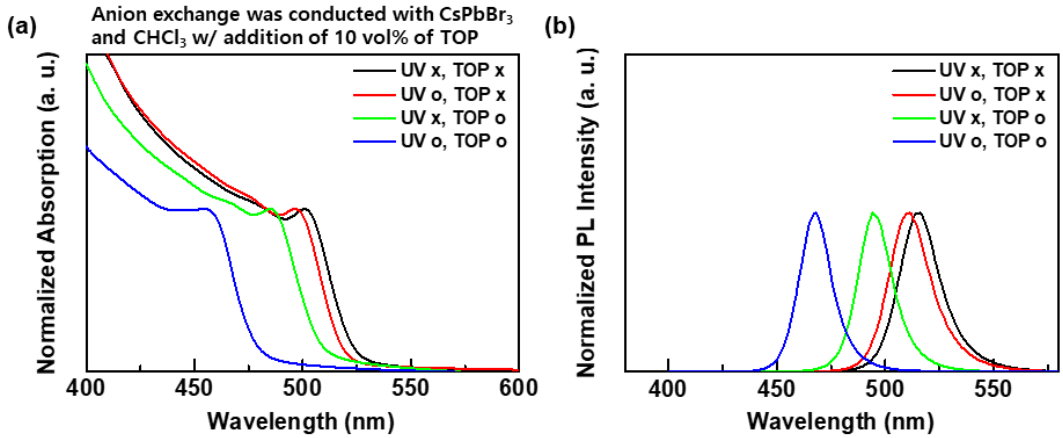

Figure 4.2. (a). Absorption and (b). PL of PT-$CsPbBr_yCl_x$ PeNCs with control of existence of TOP and UV-light. Uv-light was induced with 365nm, 6W UV-lamp at ~10 cm.

In order to rule out the possibility of UV-light induced halide exchange, or other influence of UV light on the reaction, the optical properties of PT-$CsPbBr_xCl_y$ PeNCs were collected using UV-light exposure in place of TOP. However, anion exchange occurred only in the presence of TOP and the PeNC properties were not affected by UV-light exposure, as shown in **Figure 4.2**.

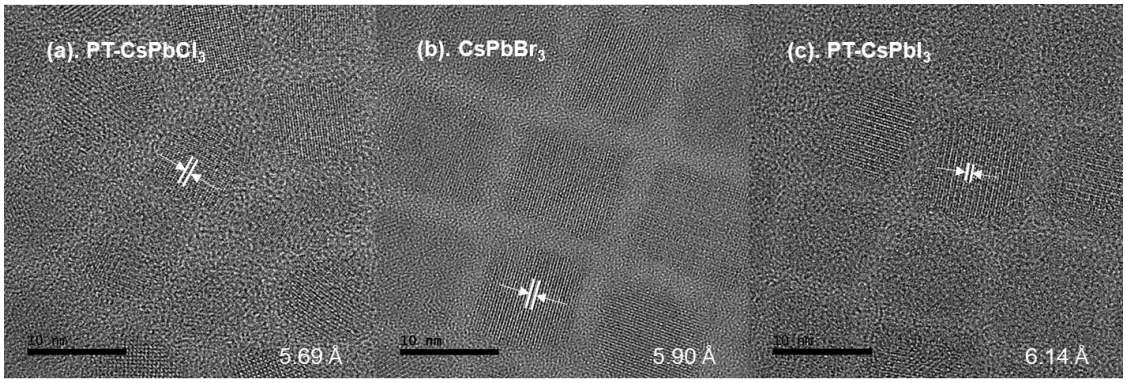

Figure 4.3. HRTEM image of the anion exchanged nanocrystals. HRTEM image of (a), PT-$CsPbCl_3$ NCs (after halide exchange), (b), pristine $CsPbBr_3$ NCs (before halide exchange), and (c), PT-$CsPbI_3$ NCs (after halide exchange).

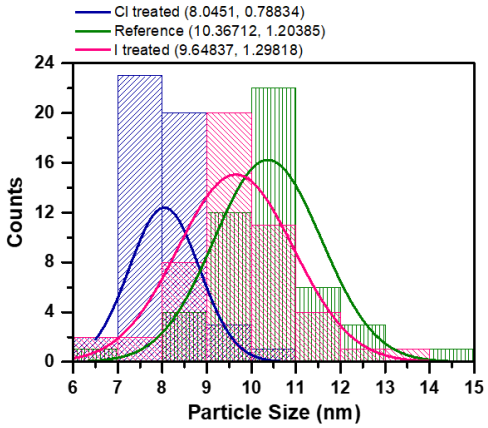

Figure 4.4. Size distribution of $CsPbBr_3$, PT-$CsPbCl_3$, and PT-$CsPbI_3$ NCs, determined by TEM.

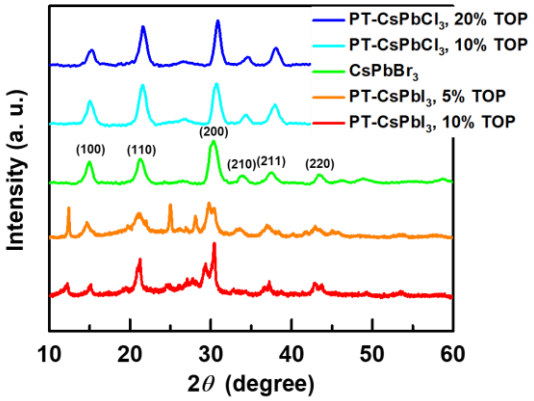

Figure 4.5. XRD patterns of anion exchanged NCs (PT-$CsPbCl_3$ and PT-$CsPbI_3$) with various TOP concentrations from $CsPbBr_3$ NCs.

After the anion exchange, the lattice distances of PT-$CsPbBr_xCl_y$, $CsPbBr_3$ and PT-$CsPbBr_xI_y$ PeNCs were measured by high-resolution transmission electron microscopy (HR-TEM) as shown in **Figure 4.3**. The size distributions of PT-$CsPbBr_xCl_y$, $CsPbBr_3$ and PT-$CsPbBr_xI_y$ PeNCs are summarized in **Figure 4.4**. As expected, anion exchange altered the lattice parameters of the PeNCs in agreement with the halide species: as-synthesized $CsPbBr_3$ PeNCs showed a spacing of 5.90 Å, PT-$CsPbBr_xCl_y$ PeNCs showed a spacing of 5.52 Å and PT-$CsPbBr_xI_y$ PeNCs showed a spacing of 6.07 Å, respectively. To clearly confirm the changed lattice distance of the PeNCs, X-ray diffraction (XRD) patterns were measured as shown in **Figure 4.5**, with indexed diffraction peaks confirming that the cubic perovskite phase was obtained in all cases (as-synthesized $CsPbBr_3$, PT-$CsPbBr_xCl_y$ and PT-$CsPbBr_xI_y$ PeNCs). Additionally, the anion exchanged PeNCs showed changed lattice parameters; a lattice spacing of 5.952 Å was observed for as-synthesized $CsPbBr_3$ PeNCs, while spacings of 6.095 Å and 5.876 Å were observed for PT-$CsPbBr_xCl_y$ and PT-$CsPbBr_xI_y$ PeNCs, respectively. The XRD parameters are in excellent agreement with HR TEM results and previous reports.[73, 89]

We observed that the anion exchange took place rapidly in the presence of TOP, but did not take place, or proceeded very slowly (over the course of weeks) in the absence of TOP. In order to understand how TOP facilitated anion exchange, we considered that the combination of haloalkane and phosphine resembles the materials used in the production of phosphorous ylides in the Wittig reaction.[90] The first step of this procedure is an organic S_N2 chemical reaction in which a nucleophilic phosphine molecule attacks a haloalkane to yield an alkylphosphonium halide intermediate. We presume that the TOP and haloalkanes used in our procedure undergo the same S_N2 reaction, which makes the halogen atoms in the solvent available for exchange as anions. To confirm this, we investigated the use of other nucleophiles and found that TOP as well as trioctylphosphine oxide, and tributylphosphine coordination ligands all facilitated the anion exchange with $CHCl_3$. Based on these observations we assume that the anion exchange occurs via the following sequence of reactions:

$$\text{1st step: } SN + RC\text{-}Y_n \rightarrow SN\text{-}CRY_{n-1}^{+} + Y^{-} \quad (4\text{-}4)$$

$$\text{2nd step: } CsPbX_3 + Y^{-} \rightarrow PT\text{-}CsPbX_xY_y + X^{-} \quad (4\text{-}5)$$

$$\text{3rd step: } SN\text{-}CRY_{n-1}^{+} + X^{-} \rightarrow SN + RCY_{n-1}X \quad (4\text{-}6)$$

SN: strong nucleophile, R: Alkyl chain, X: Original PeNCs halide, Y: Exchanging (solvent) halide.

First, when a strong nucleophile (phosphine) meets a haloalkane, a strong nucleophile-haloalkane complex $SN\text{-}CRY_{n-1}^{+}$ is generated via an S_N2 mechanism with the concomitant displacement of a halide anion Y^- (Reaction 4-4). Second, the PeNCs ($CsPbX_3$) interact with halide anions in solution which spontaneously produces the anion-exchanged PeNCs (PT-$CsPbX_xY_y$), with the concomitant ejection of the halide anion X^- from the PeNCs (Reaction 4-2). Koscher et al.[91] reported a self-anion exchange

mechanism with different halide anions, which closely resembles the reaction (4-2) and substantiates the suggested mechanism. Third, the strong nucleophile / haloalkane complex ($SN\text{-}CRY_{n-1}^{+}$) may interact with the halide anion X^- which was ejected from the PeNCs to regenerate the strong nucleophile and leave the halide anion substituted haloalkane ($SN + RCY_{n-1}X$) and PT-$CsPbX_xY_y$ PeNCs in solution (4-3). Because the solvent ($RC\text{-}Y_n$) is present is a large molar excess relative to the PeNCs, the PeNCs tend to become fully substituted with Y^- anions over time.

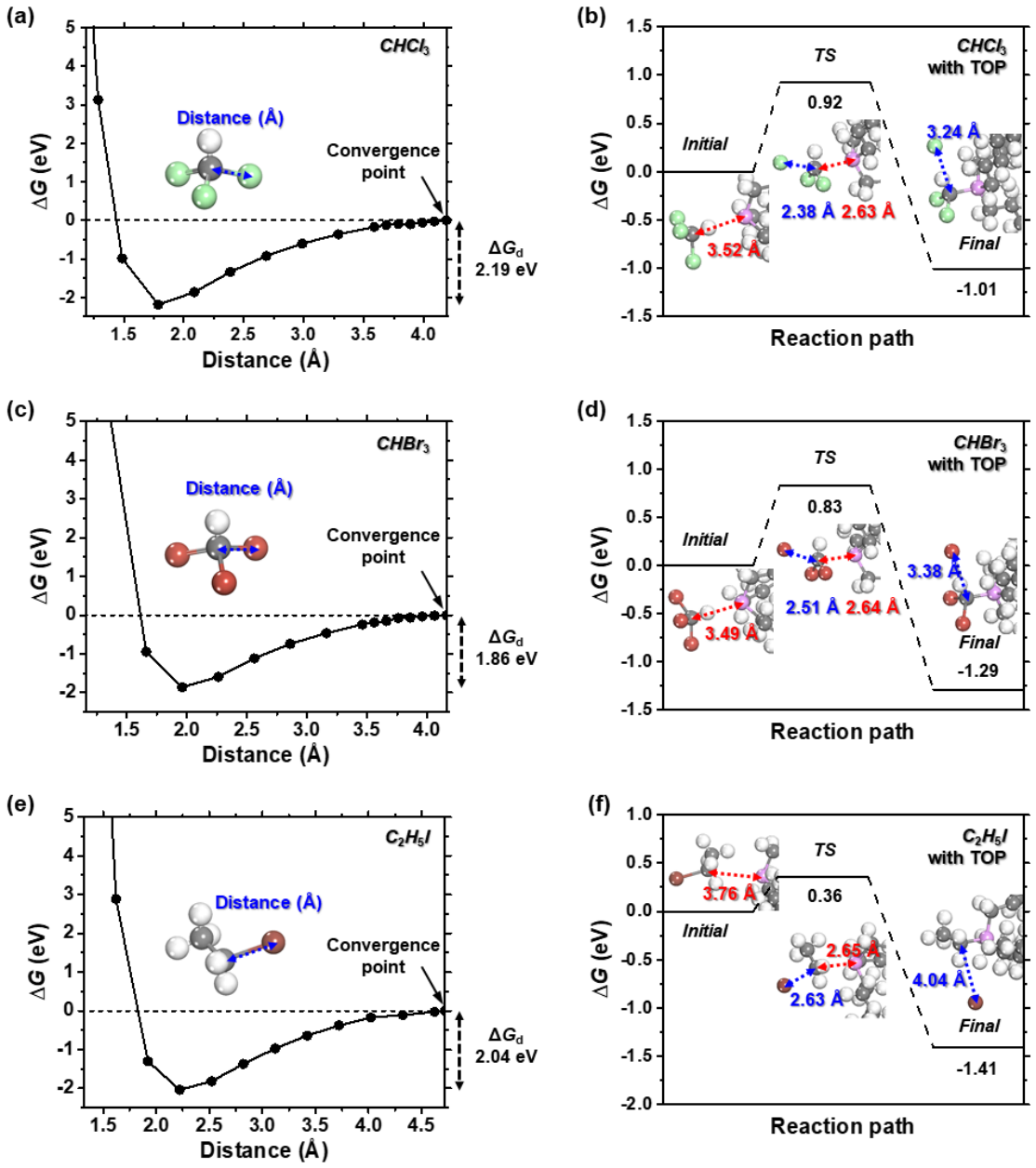

Figure 4.6. Changes of Gibb free energy of haloalkane molecules in dissociation condition. (a), (c), (e), Changes in Gibbs free energy (ΔG's) of haloalkane molecules (*i.e.*, $CHCl_3$, $CHBr_3$, and C_2H_5I) at 20 °C as a function of distance between halogen atom and carbon center of the solvent molecule. The reference state for calculating ΔG is the converged point of each system, or dissociated carbon-

halogen bond. (b), (d), (f), ΔG diagrams for dissociation of halogen atoms from haloalkane molecules mediated by TOP molecules via an S_N2 transition state, referenced to the initial state of each system. Note that red dashed arrows indicate the distance between P of TOP and the carbon center of the solvent molecule, while blue dashed arrows correspond to the distance between halogen atoms the carbon center of the solvent molecule.

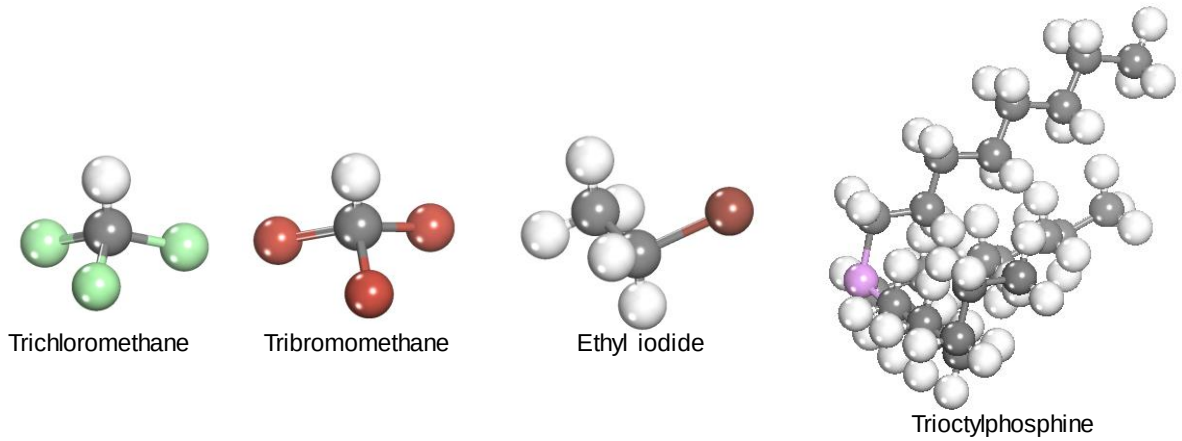

Figure 4.7. Molecular used systems for DFT calculations. From left to right, trichloromethane ($CHCl_3$), tribromomethane ($CHBr_3$), ethyl iodide (C_2H_5I), and trioctylphosphine (TOP, $C_{24}H_{51}P$), respectively. Note that gray, white, light green, brown, dark brown, and light purple colored spheres indicate C, H, Cl, Br, I, and P, respectively.

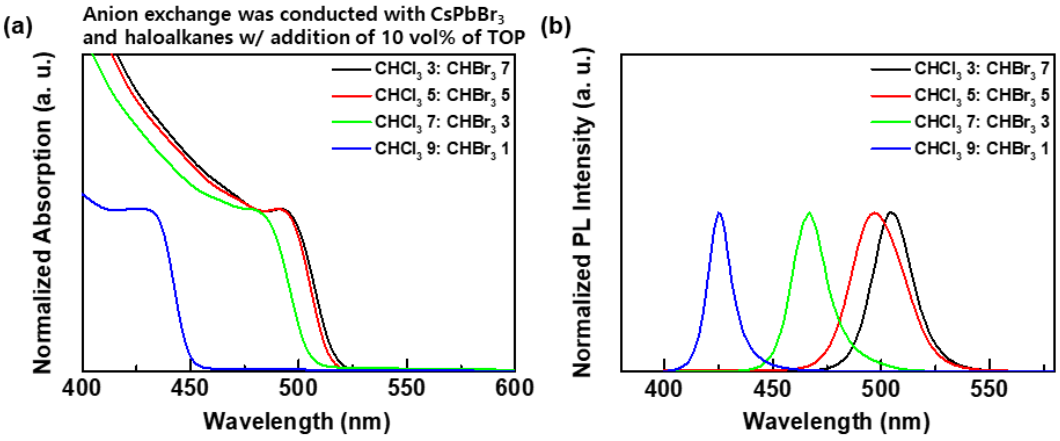

Figure 4.8. (a). Absorption and (b). PL of PT-$CsPbBr_yCl_x$ PeNCs in mixed haloalkane ($CHCl_3$ and $CHBr_3$) condition. The haloalkane solvents were mixed in volume ratio, due to their similar molecular density.

To elucidate the influence of phosphines (TOP) on the dissociation of the haloalkane molecules (Reaction 4-4), we calculated the change in Gibbs free energy (ΔG) for the dissociation of halogen atoms from haloalkane molecules (i.e., $CHCl_3$, $CHBr_3$ and C_2H_5I) in the presence or absence of TOP

molecules (**Figure 4.6** and **Figure 4.7**). For this calculation, we employed density functional theory (DFT, details in Supporting Information). In the absence of TOP, the dissociation free energy (ΔG_d) of halogen atoms was obtained as the relative free energy with respect to the distance of each halogen atom and the C of the alkyl group (**Figure 4.6a, c, e**). The results (i.e., 2.19 eV for $CHCl_3$, 1.86 eV for $CHBr_3$, and 2.04 eV for C_2H_5I) indicate that the dissociation of halogen atoms is energetically unfavorable. In terms of the effect of TOP, however, the dissociation reactions (via S_N2 mechanism) are expected to spontaneously occur with negative ΔG values (-1.01 eV for $CHCl_3$, -1.29 eV for $CHBr_3$, and -1.41 eV for C_2H_5I) through the reaction path (**Figure 4.6b**, **d, f**). The activation energy (E_a) to transition states for all haloalkanes were even smaller than the ΔG_d of each haloalkanes (0.92 eV for $CHCl_3$, 0.83 eV for $CHBr_3$, and 0.36 eV for C_2H_5I), which indicate the dissociation of halogen atoms is more energetically favorable with existence of TOP. In the case of anion exchange of $CsPbBr_3$ PeNCs using a mixture of $CHCl_3$ and $CHBr_3$, optical properties of the PeNCs exhibited Br dominant features (**Figure 4.8**), which is consistent with the DFT results shown in **Figure 4.6**. The reaction of $CHBr_3$ with TOP is more energetically favorable than the reaction with $CHCl_3$, leading to a preferential ion exchange of PeNCs with $CHBr_3$.

Note that the most probable TOP configuration to react with haloalkane molecules was determined to be type I (Model systems in Experimental details and **Figure 4.9**), with the lone pair of electrons on the phosphorus atom protruding away from the octyl chains. DFT indicates that after a transition state is formed, a halogen atom dissociates from the alkyl group, and the carbon atom forms a covalent bond with the electron donating (**Figure 4.10**) P atom in the TOP (i.e., the intermediate $SN\text{-}CRY_{n-1}^{+} + Y^{-}$). This mechanism involves transition states with significantly lower E_a than the ΔG_d's of haloalkane molecules without TOP molecules. In particular, the C_2H_5I system is predicted to be the most thermodynamically and kinetically favorable among the haloalkanes studied in this work. We also evaluated the effect of different initial orientations of $CHBr_3$ and $CHCl_3$ molecules relative to the TOP molecule to investigate the whether the relative orientations halogen and hydrogen atoms on the haloalkanes (**Figure 4.11**) influenced the energetics of the reaction. The effect of the position of the halogen on the haloalkane was marginal, with a slight elevation of E_a when H and halogen atoms were switched. Consequently, our DFT calculations provide theoretical confirmation that TOP molecules should accelerate the dissociation of halogen atoms from haloalkane solvents by providing a low-energy S_N2 transition state.

We sought to confirm whether halides from the PeNCs became incorporated into the solvent molecules. FTIR measurements can easily detect the presence of different halogen-carbon bonds in the region of 600 ~ 800 cm^{-1}. **Figure 4.12** shows FTIR spectra of supernatant solutions after centrifugation of PT-$CsPbBr_xCl_y$ PeNCs. FT-IR spectra of possible haloalkane by-products including $CHCl_2Br$, $CHClBr_2$, and $CHBr_3$ were collected as reference spectra. Using $CHCl_3$ as a source for anion exchange,

the supernatant liquid after anion exchange beginning with $CsPbBr_3$ PeNCs showed new peaks in the range of 650 cm-1 to 750 cm^{-1} in FTIR spectra. The bromine-containing trihalomethane reference spectra showed corresponding peaks in the same region indicating that new carbon-bromine bonds had formed after the anion exchange, as explained with the formula $RY_{n-1}X$ in reaction (4-6), where Y is Cl and X is Br.

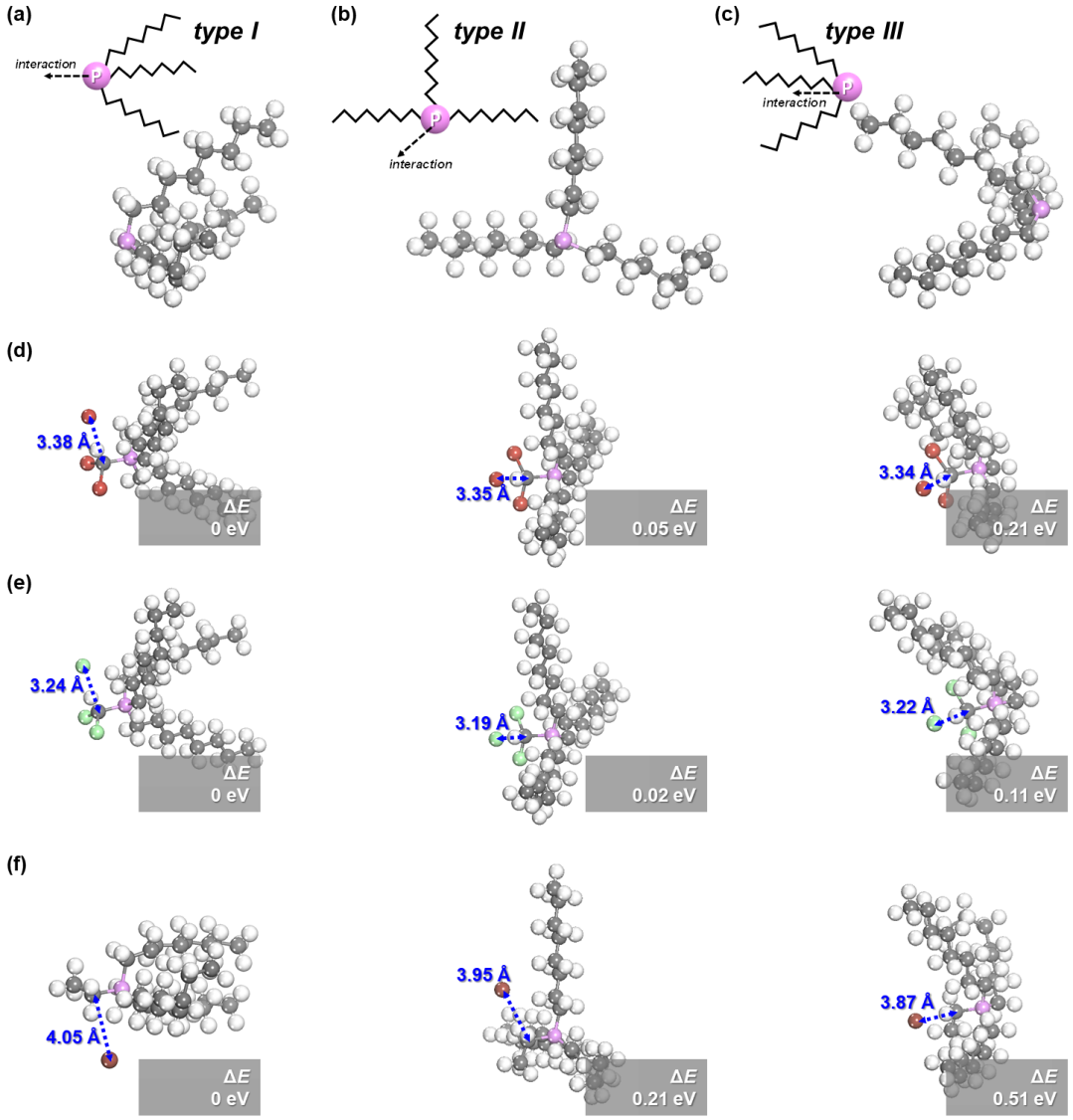

Figure 4.9. (a-c) Three general conformations used to calculate transition state energies with variable orientations of alkyl chains and lone electron pairs relative to haloalkane molecules ($CHBr_3$, $CHCl_3$, and C_2H_5I). (d-f) Relative transition state energy (ΔE) during dissociation of halogen atoms from haloalkane molecules depending on the three types of TOP orientation. Note that for calculating the ΔE, the reference energy is the type I interaction, or lowest energy transition state, for each system (*i.e.*, first figures of d, e, and f). Blue dashed arrows indicate the distance between halogen atom and carbon center of the solvent molecule, which was originally bonded with the halogen atom.

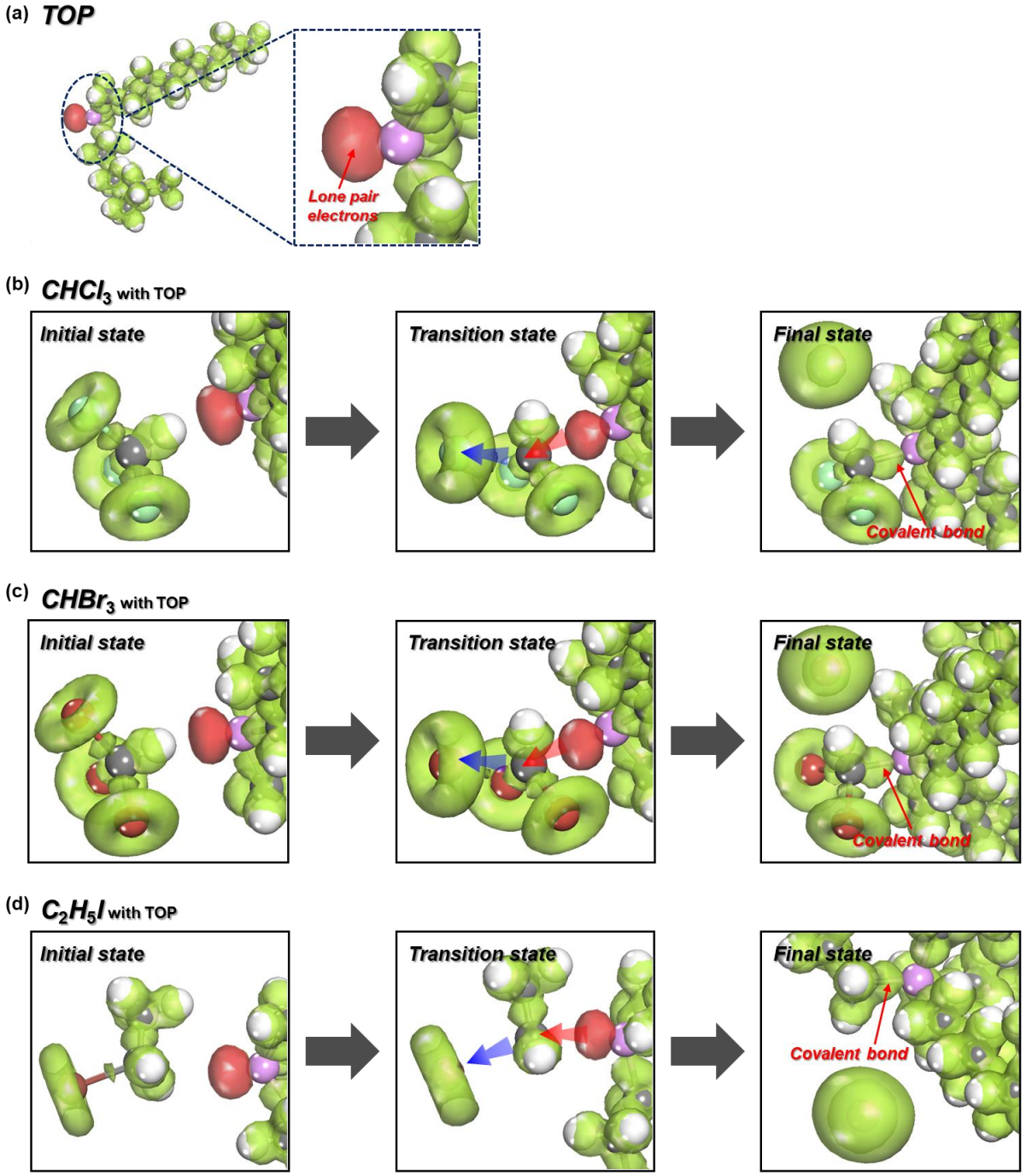

Figure 4.10. Isosurfaces (green and red colors) for deformation densities of (a), TOP, as well as reaction paths for (b), $CHCl_3$ with TOP, (c), $CHBr_3$ with TOP, and (d), C_2H_5I with TOP. Red colored isosurfaces depict the lone pair of electrons on P atoms of TOP molecules. Red and blue colored arrows indicate the interaction between P and C atoms and the dissociation of halogen atoms from haloalkanes, respectively. Note that through the deformation density analysis, the chemical bond formation can be investigated as it reflects subtracted electronic charge density of the isolated atoms from total charge density. In the final state of each haloalkane with TOP system, a covalent bond has formed between the P atom of TOP and C atom of the haloalkane due to movement of the lone pair electrons on the P atom into a new bonding orbital. In these calculations, the isosurfaces are described with the isovalue of 0.025 $e/Å^3$.

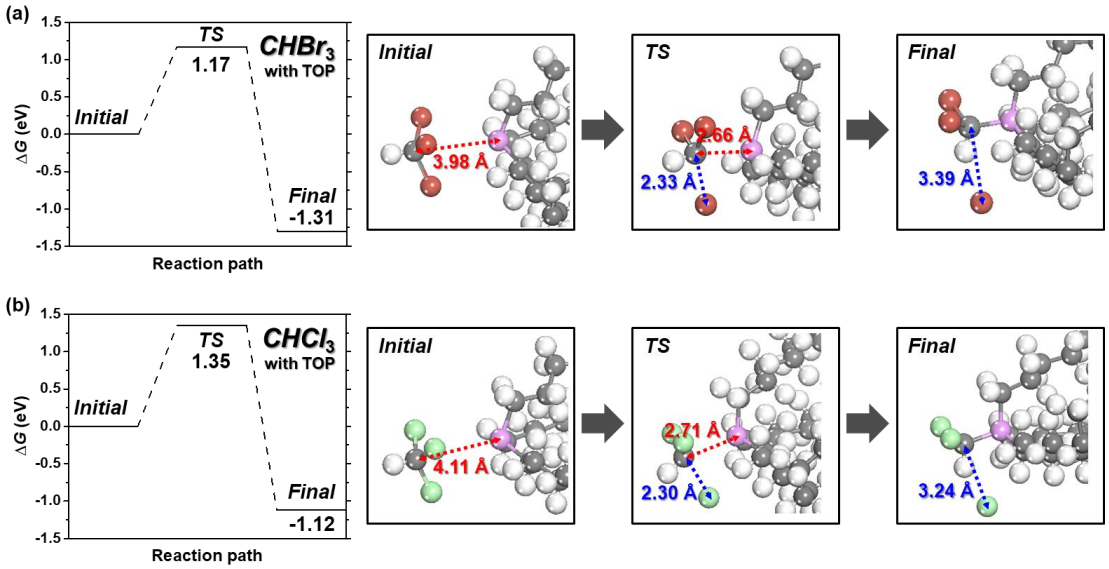

Figure 4.11. Change of Gibbs free energy (ΔG at T=20 °C) for dissociation of halogen atoms from haloalkane molecules (*i.e.*, a, $CHBr_3$ and b, $CHCl_3$) with TOP molecules, referenced to the initial state of each system. Note that red dashed arrows indicate the distance between P of TOP and the carbon center of the solvent molecule, while blue corresponds to the distance between the halogen atom and the carbon center of the solvent molecule.

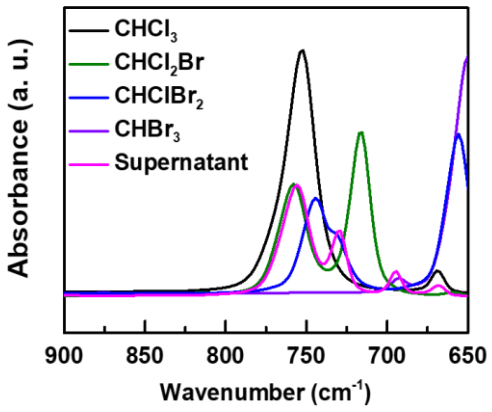

Figure 4.12. FTIR spectra of the supernatant solvent of PT-$CsPbBr_xCl_y$ PeNCs after halide exchange and reference spectra of trihalomethanes. The supernatant was collected after precipitation and centrifuging of PT-$CsPbBr_xCl_y$ PeNCs.

To clearly identify the presence of halide-exchanged solvent molecules formed during the reaction, ^{1}H-NMR spectra were also collected. **Figure 4.13** shows a ^{1}H-NMR spectrum of a supernatant solution after PT-$CsPbBr_xCl_y$ PeNCs were removed by centrifugation, plotted alongside a reference $CHCl_2Br$

spectrum; both spectra show peaks ad δ = 7.43 ppm, providing strong evidence that $CHCl_2Br$ was formed by migration of bromine from the original PeNCs to the solvent molecule during the anion exchange. The intensity of expected by-product $CHCl_2Br$ was relatively weak, indicating a low concentration, which is consistent with the thermodynamically uphill nature of the reverse formation of haloalkane from a phosphonium halide (Reaction 3). Our DFT calculations indicate that the formation of mixed haloalkane by-products from phosphonium halides generated from $CHCl_3$ (i.e., $CHCl_2\underline{Br}$ and $CHCl\underline{Br}_2$ in **Figure 4.14**) and $CHBr_3$ (i.e., $CH\underline{Cl}Br_2$ and $CH\underline{Cl}_2Br$ in **Figure 4.15**), where the underlined atom indicates the substituted atom, were all thermodynamically somewhat unfavorable. Moreover, relative to the reaction (1), the E_a are about twice as high reflecting the stability of phosphonium halides. The presence of mixed haloalkanes ($CHCl_2Br$) in the supernatant confirms that haloalkanes are regenerated from the phosphonium halide to some extent, however, we conclude that the phosphonium halide ($SN\text{-}CRY_{n-1}+ X^-$) was preferentially produced compared to re-generated phosphine and mixed haloalkane by-products (i.e., $SN + RCY_{n-1}X$) in reaction (4-6).

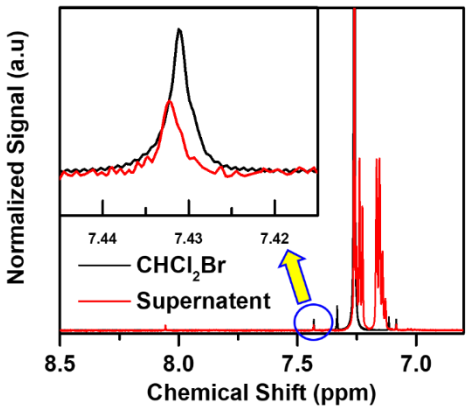

Figure 4.13. ^{1}H-NMR spectra of the supernatant solvent collected from PT-$CsPbBr_xCl_y$ PeNCs after anion exchange compared to a reference $CHCl_2Br$ solution.

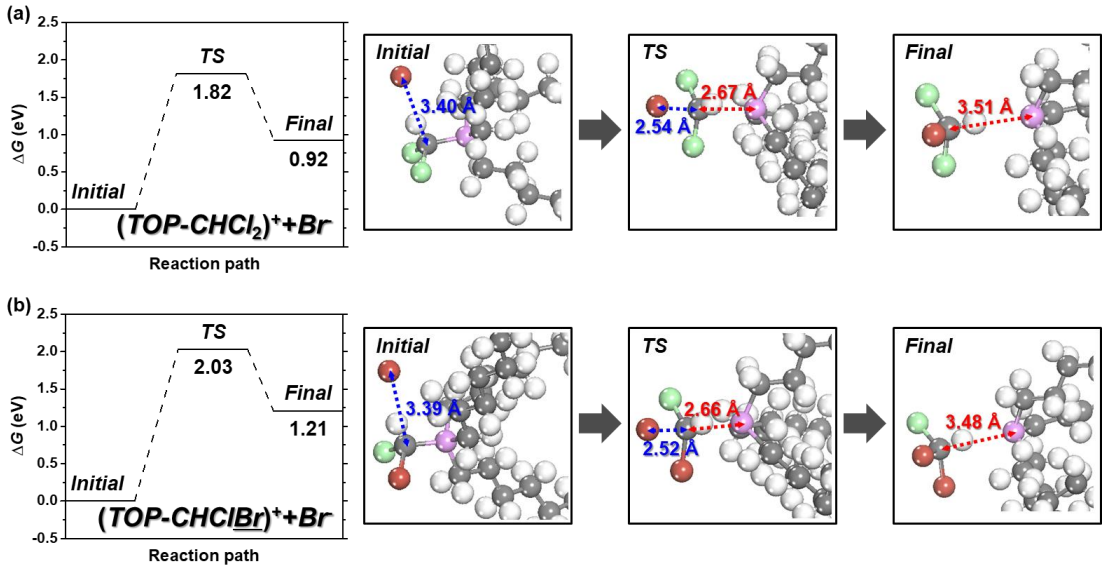

Figure 4.14. Change of Gibbs free energy (ΔG at T=20 °C) for generation of mixed haloalkane by-products from alkyl phosphonium halides, in which (a), $CHCl_2\underline{Br}$ and (b), $CHCl\underline{Br_2}$ are generated from $(TOP\text{-}CHCl_2)^+ + Br^-$ and $(TOP\text{-}CHCl\underline{Br})^+ + Br^-$, respectively. The reference state for calculating Δ*G* is the convergence point of each system. The underlined atom indicates the substituted atom. Note that red dashed arrows indicate the distance between P of TOP and the carbon center of the solvent molecule and blue for that between the halogen atom and the carbon center of the solvent molecule.

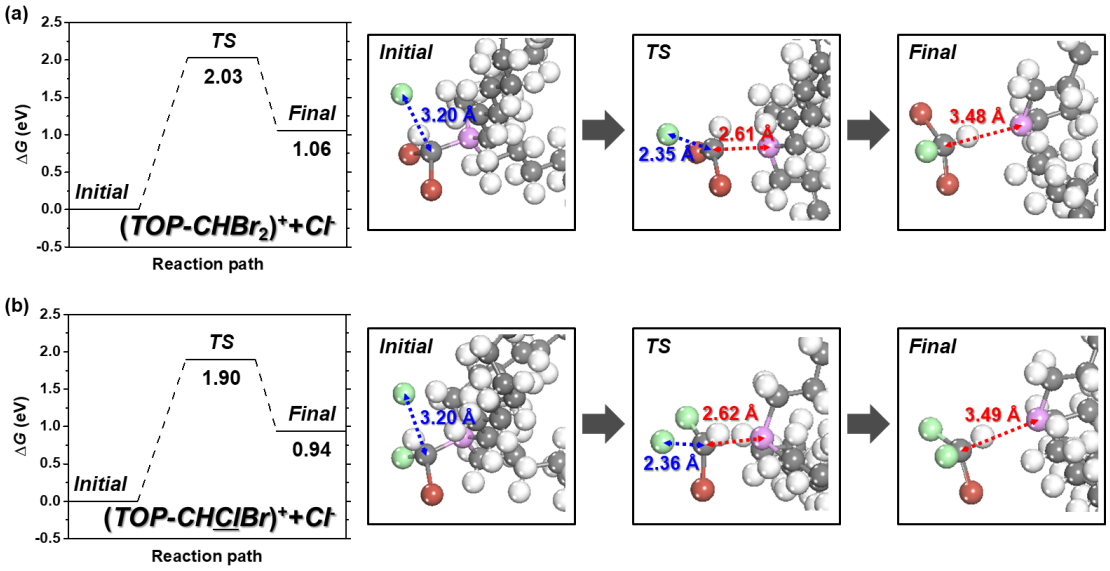

Figure 4.15. Changes of Gibbs free energy (ΔG at T=20 °C) for generation of mixed haloalkane by-products from alkyl phosphonium halides, in which (a), $CH\underline{Cl}Br_2$ and (b), $CH\underline{Cl_2}Br$ are produced from $(TOP\text{-}CHBr_2)^+ + Cl^-$ and $(TOP\text{-}CHCl\underline{Br})^+ + Cl^-$, respectively. The reference state for calculating ΔG is the convergence point of each system. The underlined atom indicates the substituted atom. Note that red dashed arrows indicate the distance between P of TOP and the carbon center of the solvent molecule and blue for that between the halogen atom and the carbon center of the solvent molecule.

	$CsPbBr_3$	TOP 1%	TOP 5%	TOP 10%	TOP 20%
Br (%)	100	72.9	48.0	22.2	15.8
Cl (%)	0	27.1	52.0	77.8	84.2

Table 4.1. Relative halide ratio calculated from XPS survey spectra of PT-$CsPbBr_xCl_y$ PeNCs varying TOP concentration.

To determine the atomic ratio of the chemically reacted PeNCs relative to the amount of TOP, XPS measurements were conducted. **Figures 4.16a**, **b** show XPS spectra of PT-$CsPbBr_xCl_y$ PeNCs using different concentrations of TOP and fixed reaction times; XPS survey spectra are shown in **Figure 4.17**. As expected, Br 3d peaks at around 67 ~ 70 eV are weakened with increasing TOP concentration. Moreover, in the region of 195 ~ 200 eV (corresponding to Cl 2p), the intensity of the peaks increased with increasing TOP concentration, clearly indicating that the anion ratio in PT-$CsPbBr_xCl_y$ is affected by TOP concentration. The relative halide ratio in anion exchanged PeNCs was calculated and is summarized in **Table 4.1**. Given that the anion ratio in PT-$CsPbBr_xCl_y$ PeNCs was strongly affected by the concentration of TOP at fixed reaction times, it is clear that the concentration of TOP affects the reaction rate of the anion exchange process, supporting the suggested S_N2 reaction mechanism.

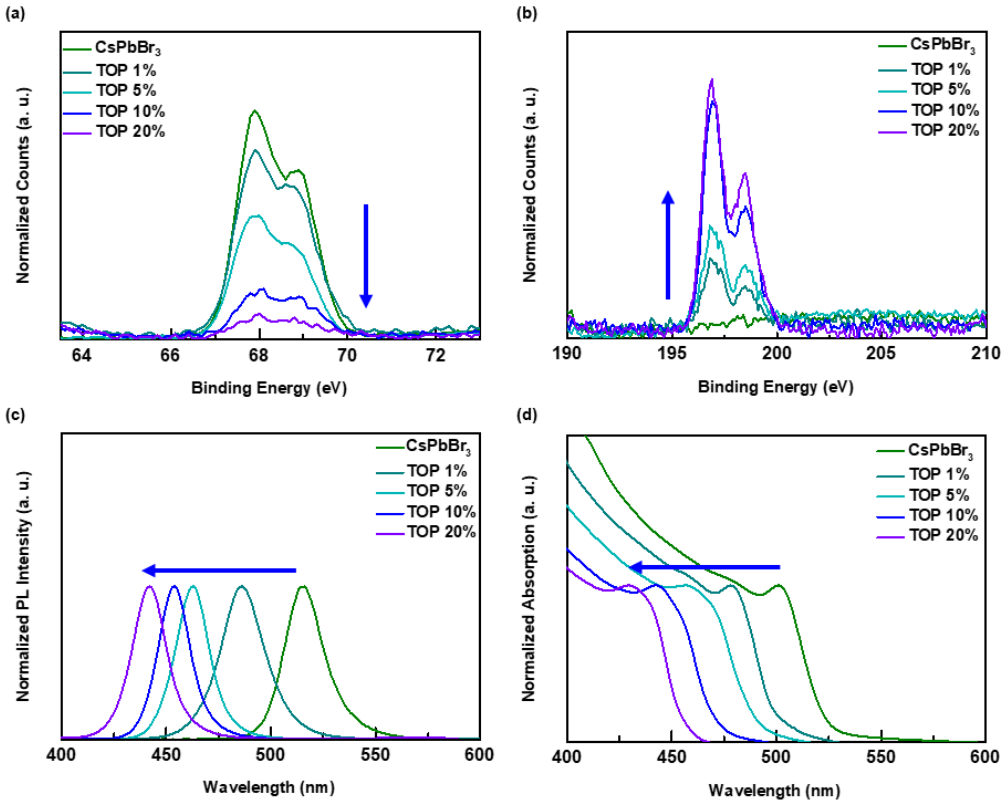

Figure 4.16. Influence of TOP concentration on atomic and optical properties of PT-$CsPbBr_xCl_y$ PeNCs.

(a), XPS spectra (Br 3d peak region) and (b), XPS spectra (Cl 2p peak region), (c), Photoluminescence spectra, (d) Absorption spectra.

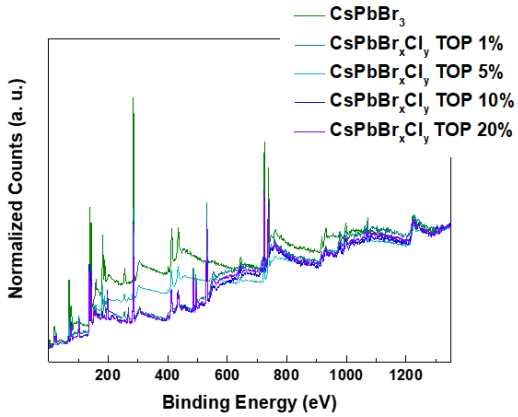

Figure 4.17. XPS survey spectra of PT-$CsPbBr_xCl_y$ PeNCs varying TOP concentration at same reaction time.

Our newly discovered solvent post-treatment method for PeNCs yields similar results compared to previously reported[89] anion exchange methods using halide salts. Previous anion exchange methods controlled the ratio of halides in PeNCs via the concentration of halide containing salt used in the exchange because only PeNCs and salt participated in the reaction. In contrast, the kinetics of our anion exchange method were strongly affected by the nucleophile concentration, following S_N2 chemical reaction kinetics. **Figures 4.16c**, **d** and **Table 4.2** show how the optical properties of PT-$CsPbBr_xCl_y$ PeNCs vary with TOP concentration after 10 min reaction time in $CHCl_3$. At higher concentrations (20%) of TOP, the reaction proceeds rapidly and most of the Br halogen atoms are exchanged after 10 min. At lower TOP concentrations, the absorption onset and PL peak positions of PT-$CsPbBr_xCl_y$ PeNCs could be easily adjusted continuously through the wavelength region of 550 nm ~ 430 nm; between the properties of $CsPbBr_3$ and $CsPbCl_3$ phases. Thus, PeNCs properties could easily be tuned via nucleophile concentration and reaction time.

	$CsPbBr_3$	TOP 1%	TOP 5%	TOP 10%	TOP 20%
Peak Position (nm)	515	486	462	453	441
FWHM (nm)	23	24	18	17	18

Table 4.2. Change in absorption peak positions and full width at half maximum (FWHM) upon PT-$CsPbBr_xCl_y$ PeNCs varying TOP concentration.

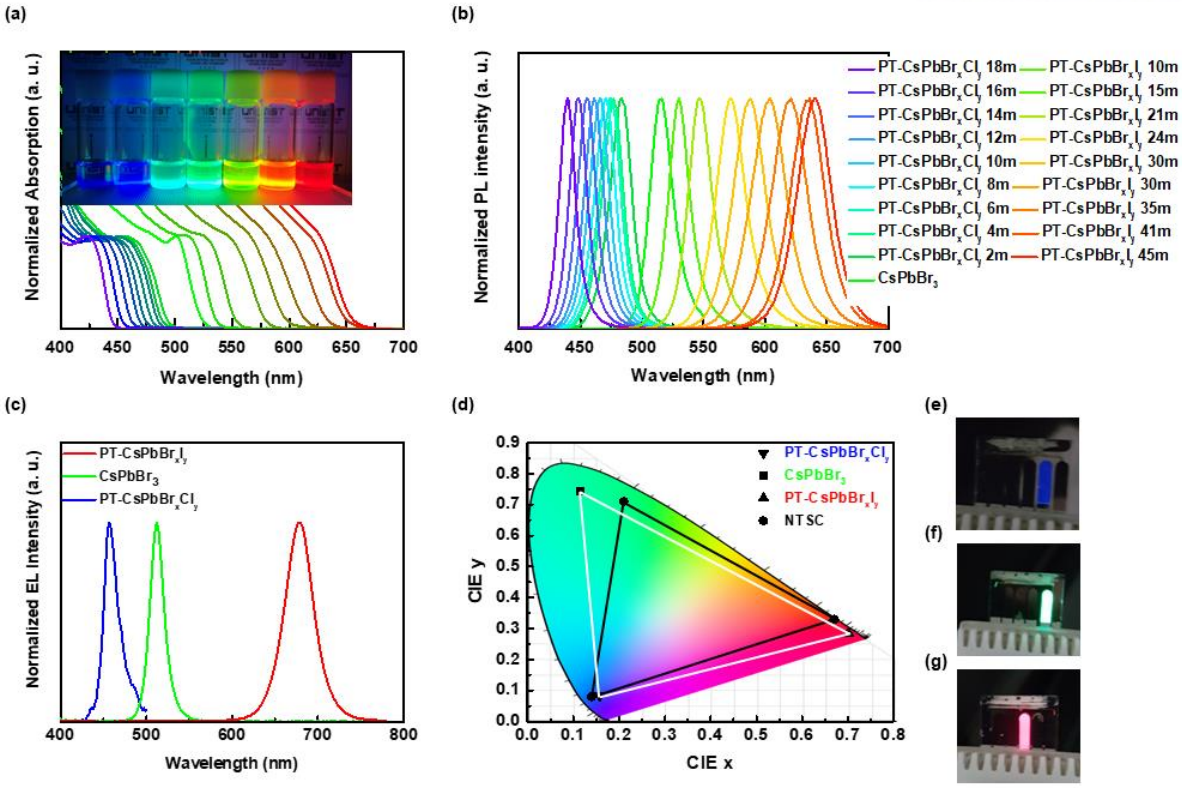

Figure 4.18 Fine control of the optical properties and electroluminescence (EL) of PT-$CsPbBr_xY_y$ PeNCs. (a), Absorption (inset: photograph of solutions of the as-synthesized $CsPbBr_3$ and PT-$CsPbBr_xY_y$ PeNCs) and (b), PL spectra of the PT-$CsPbBr_xY_y$ PeNCs with composition controlled by the reaction time. (c). Red, green and blue EL spectra with emission peaks at 457 nm from PT-$CsPbBr_xCl_y$, 512 nm from $CsPbBr_3$ and 679 nm from PT-$CsPbBr_xI_y$ PeNCs. (d). CIE 1931 color space coordinates of light emitting diodes with anion exchanged PeNCs (down triangle for PT-$CsPbBr_xCl_y$, square for $CsPbBr_3$ and up triangle for PT-$CsPbBr_xI_y$, with white lines) compared to NTSC color standards (circles and black lines). (e-g). photographs of light emitting diodes with anion exchanged PeNCs. (e), for an LED using PT-$CsPbBr_xCl_y$, (f), using $CsPbBr_3$, (g), using PT-$CsPbBr_xI_y$.

Through the fine control of the nucleophile concentration and reaction time, we obtained sharp PL spectra covering the full visible spectrum from 400 nm ~ 700 nm, starting with the same batch of $CsPbBr_3$ PeNCs as shown in **Figure 4,18a** and **b**. Absorption spectra (**Figure 4.18a**) and PL spectra (**Figure 4.18b**) were obtained with a fixed TOP concentration (10%) and fine control of the reaction time. The reaction can be quenched at any time by centrifugation to isolate nanocrystals with intermediate composition. After a reaction time of about 18 minutes with $CHCl_3$, PT-$CsPbBr_xCl_y$ PeNCs exhibited purple luminescence at 440 nm. And after a reaction time of about 45 minutes with C_2H_5I, PT-$CsPbBr_xI_y$ NCs exhibited pure red luminescence at 640 nm as expected.

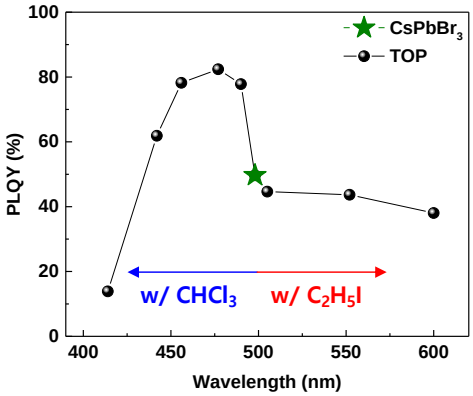

Figure 4.19. PLQY data of PT-CsPbBr$_x$Y$_y$ PeNCs over visible wavelength region. From the as-synthesized $CsPbBr_3$ PeNCs (star-shape symbolled), with TOP, $CHCl_3$ precursor shifts to the blue region and C_2H_5I shifts to the red region (black-circle). UV-light induced PT-CsPbBr$_x$Y$_y$ PeNCs with $CHCl_3$ precursor was labelled as red-square for comparison.

In order to investigate the influence of ion exchange on fluorescence efficiency, PL quantum yield (PLQY) measurements were conducted, these data are summarized in **Figure 4.19**. The overall PLQY were not severely decreased after anion exchange process and even higher PLQY were obtained in the case of PT-CsPbBr$_x$Cl$_y$ PeNCs.

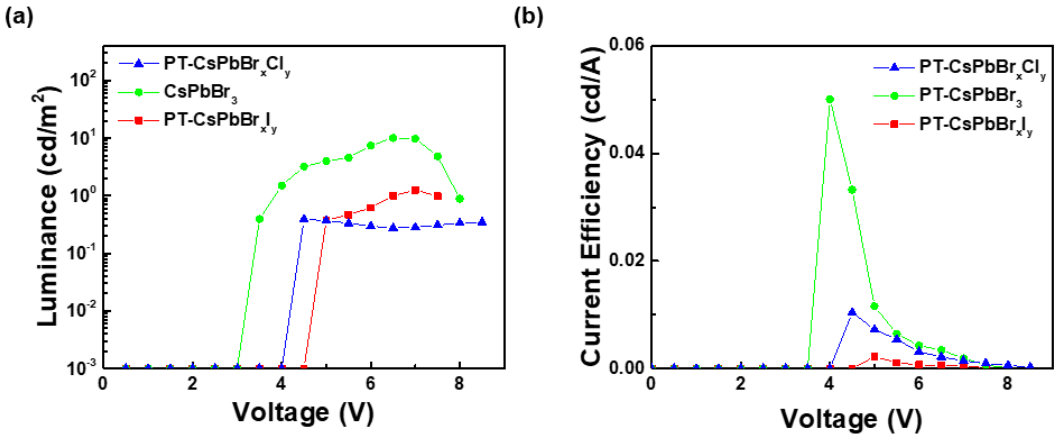

Figure 4.20. Characteristic data of LEDs fabricated with anion exchanged PeNCs. (a), L-V curves, (b), CE-V curves for the RGB-LEDs with PT-CsPbBr$_x$Y$_y$ PeNCs.

PeNCs condition	Max. Luminance [cd/m^2]	Max. Current efficiency [cd/A]	Max.EQE [%]	Voltage @ Max. Luminance [V]
PT-CsPbBr$_x$Cl$_y$	0.391	0.010	0.009	4.5
CsPbBr$_3$	10.8	0.050	0.014	7
PT-CsPbBr$_x$I$_y$	1.26	0.002	0.022	7

Table 4.3 Device parameters with RGB-LEDs with anion exchanged PeNCs.

Electroluminescence (EL) spectra could also be fine-tuned to target Red-Green-Blue (RGB) light emitting devices (LEDs) covering the full-color gamut for display applications. **Figure 4.18c** shows EL of LEDs with emission peaks at 457 nm for PT-CsPbBr$_x$Cl$_y$ PeNCs, 512 nm for CsPbBr$_3$ PeNCs and 679 nm for PT-CsPbBr$_x$I$_y$ PeNCs. Device parameters for these LEDs are summarized in **Figure 4.20** and **Table S3**. The devices were stable about ~20 cycles scanned 0 ~ 6 V operating condition in N_2 filled glove box. The devices were stable up to 7.5 V, 8 V, 8.5 V for each Red, Green, Blue LEDs. The LED devices exhibited very saturated and pure colors, as shown in the International Commision on Illumination (CIE) 1931 color space chromaticity diagram in **Figure 4.18d**. The LEDs produced in this work fully covered the National Television System Committee (NTSC) standard. Photographs of LEDs based on PT-CsPbBr$_x$Cl$_y$, CsPbBr$_3$ and PT-CsPbBr$_x$I$_y$ PeNCs are shown in **Figures 4.18e-g**. The size of the operating area was 13 mm^2 and showed uniform emission across the whole operating area. With our simple, reversible and non-destructive post-treatment method of anion exchange, we succeeded in producing full coverage of the visible region from 400 nm ~ 700 nm with CsPbX$_3$ PeNCs. In addition, very saturated and pure RGB LED devices were successfully fabricated. We expect that this convenient method of exchanging halide anions with non-polar solvents may be widely applied to perovskite materials as a general and non-destructive method to tune halide composition.

4.4 Conclusion

In summary, we have discovered, for the first time, a non-destructive, controlled anion exchange method for $CsPbX_3$ (X = Cl, Br, I) PeNCs in which a strong nucleophile (TOP) triggers the exchange of halides with haloalkane solvents. The exchange method can be repeated in any direction ($CsPbCl_3 \rightleftharpoons CsPbBr_3 \rightleftharpoons CsPbI_3$) to achieve any desired halide composition without losing the original structure of the NCs. To elucidate the exchange mechanism, a variety of experimental and computational techniques were employed to determine that the exchange mechanism proceeds in 3 steps beginning with the nucleophilic attack of a solvent molecule by a strongly nucleophilic phosphine ligand. This new reaction has good reproducibility and can easily be controlled via the concentration of TOP and reaction time. We successfully fabricated the LEDs with finely controlled emission color and RGB LED devices with excellent color purity. Our procedure does not involve exchangeable cations, which prevents unexpected lattice alterations and ensures that halide exchange is the only aspect of the PeNCs which is altered. We expect that this procedure may be of great utility to the field of halide-based perovskites.

CHAPTER 5. Origin of Luminescence Spectra Width in Perovskite Nanocrystal with Surface Passivation

The content of this chapter is published in *Nanoscale*, **2020**, 12, 21695-21702.

5.1 Research background

Optoelectronic devices with metal halide perovskites have been intensively researched over the last decade. Photovoltaic devices based on halide perovskites achieved over 25% of external quantum efficiency (EQE), while light emitting diodes (LEDs) with halide perovskites also achieved over 20% of EQE, due to the excellent optoelectronic properties of high absorption coefficient, high charge carrier mobility, easily tunable bandgap, narrow emission linewidth, and wide colour gamut.[10, 29, 92] $CsPbX_3$ (X = Cl, Br, and I) based perovskite nanocrystals (PeNCs) were synthesized through the hot-injection method, maintaining attractive perovskite properties and enhancing the photoluminescence quantum yield (PLQY) for light emitting applications.[20] The bandgap and correlated colour of the PeNCs could be easily tuned over the entire visible wavelength region by controlling the halide composition to obtain the desired emission. Although the blue colour PeNC-based LEDs (PeLEDs) have been very actively researched and have achieved high performance, they have shown lower device performances than other colour PeLEDs.[26, 28, 93-97]

To improve PeLEDs, the optoelectronic properties of PeNCs were enhanced through surface passivation *via* post-treatment methods, not only for blue color PeLEDs but also for PeLEDs of other colours, including red and green color PeLEDs. Through surface passivation, such as anion passivation and ligand exchanges, PeNCs could be modified to achieve the desired colour, improved device efficiency, and longer device lifetime. With the anion exchange post-treatment methods, full colour emission was achieved starting only with $CsPbBr_3$-based PeNCs with enhanced PLQYs.[55, 73, 74, 89, 98] The ligand exchanging post-treatment methods were heavily researched to obtain enhanced optoelectronic properties and improved device performances.[42, 43, 47] Most of the advantages of post-treatments originated from defect passivation on the surface of PeNCs. The surface defects, generated from the anion and/or ligand vacancies on PeNCs, became non-radiative recombination centres, which impair the emission properties of PeNCs and result in decreased PLQY.

Along with the improved optoelectronic properties by surface passivation, there is another important fascinating property of PeNCs: the narrow emission linewidth, which results in high colour purity that enables the next-generation display applications. It is well known that PeNCs have a narrow emission

linewidth without surface passivation, and there are reasons for the narrow emission linewidth of PeNCs: high defect tolerance, weak phonon coupling, and weak quantum confinement effect at the usual size condition (~10 nm).[20, 99-101] Interestingly, a narrower linewidth was achieved by surface passivation methods.[102-105] However, until now, there have been ambiguous interpretations for the narrowed emission linewidth of PeNCs with surface passivation.

In this work, we sought to find the origin of the narrow emission linewidth of luminescence from blue colour (@470 ± 2 nm) emitting PeNCs with surface passivation. By comparing the emission linewidth between pristine PeNCs (PR-PeNCs) and PeNCs with surface passivation (SP-PeNCs), the differences in the full-width at half-maximum (FWHM) of the emission spectra were focused upon to find out the origin of the emission linewidth. Surface passivation was divided into two parts: anion passivation and ligand passivation. It was revealed that the narrower luminescence spectra originated from ligand passivation, and the improved optoelectronic properties originated from anion passivation.

5.2 Experimental details

General

Characterization: UV-Vis NIR absorption spectra were obtained by using a Cary 5000 (Agilent) spectrophotometer and the photoluminescence spectra were measured with an nF900 instrument (Edinburgh Photonics) with a xenon lamp as an excitation source. The PLQY values were obtained with a QE-2000 system from Otsuka Electronics Co., Ltd. Transmission Electron Microscopy (TEM) images were recorded by using JEM02100 and JEM-2100F systems from JEOL. The samples for TEM measurements were prepared by dropping the nanocrystal solution onto carbon coated Cu grids from Ted Pella, Inc. Fourier Transform Infrared Spectroscopy (FTIR) spectra were recorded using a Cary 670 FTIR spectrometer (Agilent). XRD patterns were obtained by using a high-power diffractometer (D/MAX2500V/PC from Rigaku) with settings including 40 kV potential, 200 mA current, Cu-rotating anode, and Cu Kα radiation ($\lambda = 0.1542$ nm) using a graphite monochromator and a scintillation counter. Time-resolved and steady-state PL spectra were measured by using a FluoTime 300 spectrometer. The samples were photoexcited with a 510 nm continuous wave and a pulsed diode laser head (LDH-D-C-510). PL decay curves were fitted to a biexponential decay model using FluoFit software. The surface morphology was scanned using an atomic force microscope (AFM) of VEECO Dimension 3100 equipped with Nanoscope V. LED measurements were performed using a Keithley 2400 source measurement unit and a Konica Minolta spectroradiometer (CS-2000, Minolta Co.)

Nanocrystal synthesis

The synthesis of $CsPbX_3$ PeNCs followed the method of Protesescu et al.[20] with modification. In a usual synthesis, 0.94 mmol of PbX_2 with the desired halide ratio and 25 mL of octadecene (ODE) were placed in a 100 mL 3-neck flask and dried under vacuum for 1 h at 120 °C. 2.5 mL of oleic acid (OA) and 2.5 mL of oleylammine (OAm) were added to the lead halide solution, and 0.65 ml of trioctylphosphine (TOP) was used to dissolve the $PbCl_2$ precursor. Then the temperature of the mixture was raised to the injection temperature, and the mixture was kept under an Ar atmosphere. 2 mL of previously synthesized Cs-oleate (0.163 g of Cs_2CO_3 in 8 mL of ODE and 0.5 mL of OA degassed for an hour and kept under Ar with a temperature increase to 120 °C immediately prior to injection) was swiftly injected. After 5 s, the PeNC solution was quickly cooled to room temperature with an ice bath. After synthesis, the PeNCs were purified via centrifugation at 8000 rpm for 15 min with butanol. After the centrifugation of the PeNCs, they were re-dispersed in 5 mL of toluene.

Surface passivation

The surface passivation process was modified with a previously reported method.[55] The PeNC solution was mixed with a solvent containing $CHCl_3$ and $CHBr_3$ mixed at an appropriate ratio. Then the desired volume of nucleophilic ligands (TOP, THP, TBP, typically 5 vol%) was added to start the reaction. The solution was warmed to 50 °C to accelerate the reaction. The reaction was quenched by

precipitating into 3 volumes of methyl acetate. The precipitated PeNCs were collected by centrifugation (at 12 000 rpm for 15 min) and re-dispersed in toluene or hexane.

Device fabrication

Device fabrication proceeded following an adaptation of the method reported by Pan et al.[43] Briefly, PEDOT:PSS solutions were spin-coated onto pre-cleaned, glass/ITO substrates at 3000 rpm for 40 s, followed by thermal annealing at 150 °C for 15 min under air. After cooling to ambient temperature, the PeNCs were spincast at 2000 rpm for 60 s in an N_2-filled glove box. Finally, TPBi (50 nm), LiF (1 nm), and Al (100 nm) were deposited sequentially by thermal evaporation under high vacuum ($<10^{-6}$ Torr).

5.3 Result and discussion

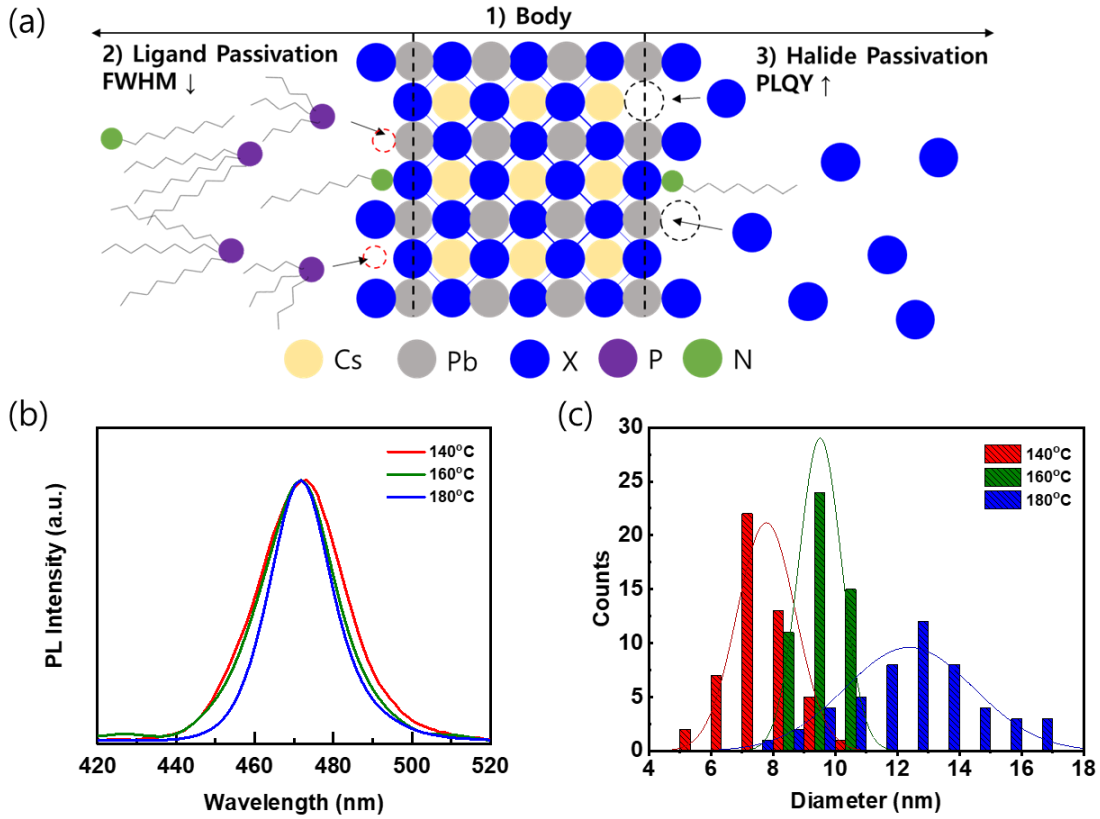

Figure 5.1. (a) Scheme of the parts of PeNCs affecting the optical properties. (b) Photoluminescence (PL) spectra and (c) size distribution of the PeNCs with different injection temperature conditions in the synthesis procedure.

For the systematic investigation of the origin of the emission linewidth, we categorized the parts of PeNCs that could affect the FWHM of the luminescence of PeNCs (**Figure 5.1a**). The first part is the body of the PeNCs. The mean size, size distribution, stoichiometry, and crystal phase of PeNCs mainly affect the FWHM, which could be adjusted during the synthetic processes. The synthetic process includes many factors (concentration of precursor solids and ligands, temperature, growth time, etc.) that might have a large effect on the FWHM.

The second part is the surface of the PeNCs. In general, the surface of PeNCs critically affects the luminescence from the surface defects. The defects could produce trap states and cause broadening of the luminescence spectra and drop in the optoelectronic properties. So, eliminating the defects is one of the important processes for high-quality PeNCs. Even more, the trap states are the main limiting factor of the device performance and colour purity of PeLEDs. In this work, we tried to analyse the surface part as divided parts of anion-related surfaces and ligand-related surfaces and these will be discussed later.

Due to the large contribution for the FWHM in PeNCs, the investigation of the effect of body part control on the FWHM was conducted. The factors affecting the FWHM by the body part were expected to originate from the statistical size factors of the nanocrystals, such as the mean size or size distribution of the nanocrystals. The synthetic conditions were regulated to control those body parts of the nanocrystals. With the hot-injection method, the injection temperature of synthesis controls the mean size of the nanocrystals. The injection temperature was controlled from 180 °C to 140 °C with careful adjustment of the precursor lead halide ratios to obtain a similar blue luminescence peak around 470 nm. For example, PeNCs with the injection temperature at 140 °C were reacted with 0.63 mmol of $PbBr_2$ and 0.31 mmol of $PbCl_2$, but PeNCs with the injection temperature at 180 °C were reacted with 0.58 mmol of $PbBr_2$ and 0.36 mmol of $PbCl_2$. **Figure 5.1b** shows the PL spectra of PeNCs with different injection temperatures, while **Table 5.1** presents the peak position and FWHM. With increasing injection temperature, the FWHM showed a decreasing tendency from 0.151 eV to 0.113 eV (27.06 nm to 20.22 nm).

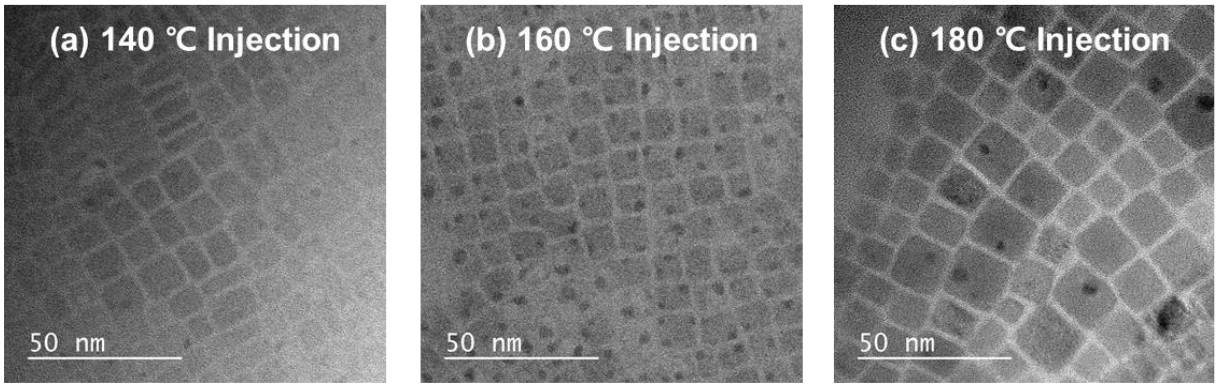

Figure 5.2. TEM images of the blue emissive PeNCs synthesized with (a) 140℃ injection (b) 160℃ injection and (c) 180℃ injection conditions.

Injection Condition	Peak (nm)	FWHM (nm)	FWHM (eV)	PLQY (%)	Mean Size (nm)	SD (nm)
140℃	471.89	27.06	0.151	7.80	7.78	0.94
160℃	471.20	23.80	0.133	6.90	9.51	0.69
180℃	471.86	20.22	0.113	11.26	12.39	2.08

Table 5.1. Summarized peak positions, full width at half maximum of spectra (FWHM), photoluminescence quantum yield (PLQY) and statistics of size distribution of PeNCs synthesized with different injection temperatures.

With the hot-injection method, as the injection temperature increases, the mean size of nanocrystals is known to normally increase. TEM images were obtained to confirm the mean size and the size distribution of the PeNCs (**Figure 5.2**). **Fig. 5.1c** shows the mean size and the size distribution of the PeNCs obtained from the TEM image. The synthesized PeNCs also showed the well-known behaviour that the mean size (diameter) of the PeNCs injected at 180 °C was greater than the mean size of those injected at 160 °C. Interestingly, the PeNCs injected at 140 °C showed that particles have a platelet shape, which was also reported by Alivisatos et al.[106] To compare the size of platelet-shaped PeNCs with cubic-shaped PeNCs, the diameter of platelet-shaped PeNCs was calculated assuming a cubic-shaped PeNCs with a volume equal to the platelet-shaped PeNCs. The mean diameters of the PeNCs are presented in **Table 5.1**. Interestingly, the size distribution seemed to have less effect on the FWHM. There was weak correlation between the size distribution and the FWHM of luminescence, considering that the PeNCs with 180 °C injection temperature have narrower FWHM but broader size distribution.

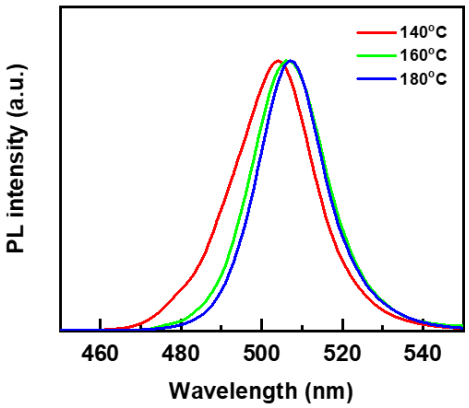

Figure 5.3. PL spectra from the green emissive PeNCs synthesized with different injection temperature. (FWHM: 25.36nm for 140°C, 22.72nm for 160°C, and 20.96nm for 180°C injection temperature condition)

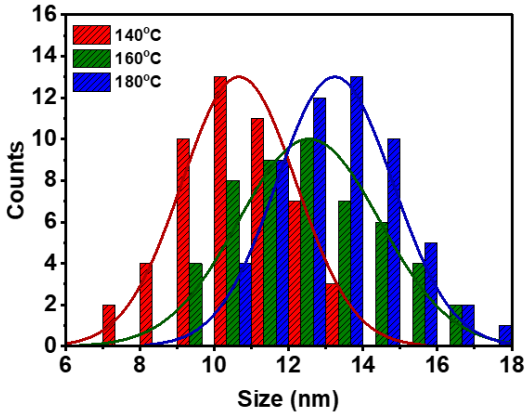

Figure 5.4. Size distribution of the green emissive PeNCs synthesized with different injection

temperature. (mean size: 10.67nm for 140°C, 12.55nm for 160°C, and 13.24nm for 180°C; standard deviation: 1.54nm for 140°C, 1.90nm for 160°C, and 1.57nm for 180°C)

To disentangle the effect of the size of PeNCs from the effect of the compositional variation, a similar comparison was conducted with $CsPbBr_3$-based PeNCs. **Figure 5.3** shows the PL spectra of $CsPbBr_3$-based PeNCs synthesized at different injection temperatures. As shown above, the FWHM of the emission from the $CsPbBr_3$-based PeNCs was narrowed under synthesis conditions with higher injection temperature. **Figure 5.4** shows the mean size and the size distribution of the $CsPbBr_3$-based PeNCs, determined by the TEM measurements. Similarly, the tendency of the FWHM seemed to be correlated with the mean size but not with the size distribution. With these data, the mean size of the PeNCs seemed to have more effect on the FWHM of PeNCs than the size distribution of PeNCs, regardless of the compositional variation.

The bandgap of nanocrystals is the combination result of nanocrystals of different sizes and is affected by the quantum confinement effect. Therefore, the size distribution should affect the bandgap of nanocrystals. However, the experimental results showed that the mean size of PeNCs governs the FWHM. To interpret this result, we focused on the non-linear characteristic of the quantum confinement effect. The bandgap broadening by the quantum confinement effect becomes severe in smaller nanocrystals. This means that nanocrystals with the same standard deviation and different mean sizes will lead to different FWHM of PL. For example, based on the paper by Butkus et al.,[107] for a set of perovskite nanocrystals with the smallest particle of 4 nm and the biggest particle of 8 nm, the difference of the bandgap becomes about 0.1 eV. However, for nanocrystals with the smallest particle of 8 nm and the biggest particle of 12 nm, the difference of the bandgap becomes about 0.05 eV. Therefore, the FWHM broadening by the size distribution could be amplified in PeNCs with a smaller mean size.

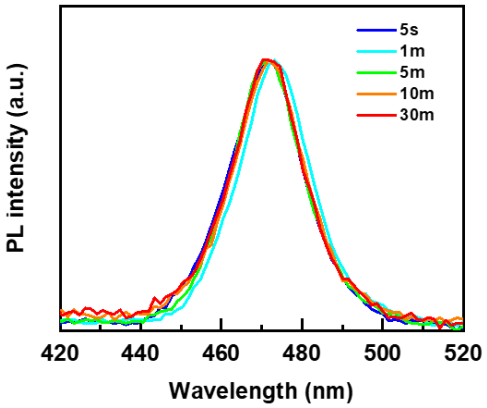

Figure 5.5. PL spectra from the PeNCs synthesized with different growth time conditions.

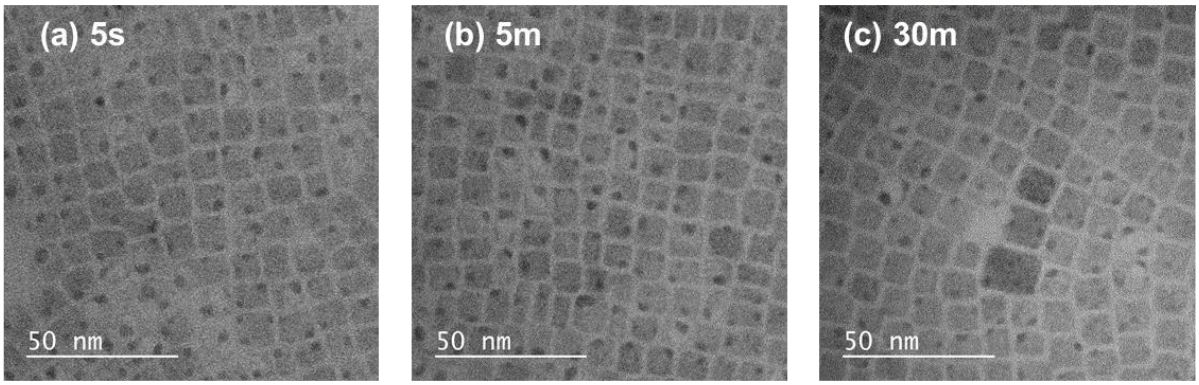

Figure 5.6. TEM images of the PeNCs synthesized with (a) 5 seconds (b) 5 minutes and (c) 30 minutes growth time condition.

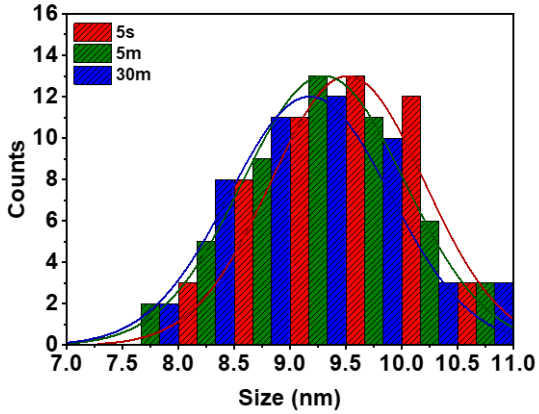

Figure 5.7. Size distribution of the PeNCs synthesized with different growth time.

Growth Time	Peak (nm)	FWHM (nm)	FWHM (eV)	PLQY (%)	Mean Size (nm)	SD (nm)
5s	471.20	23.80	0.133	6.9	9.52	0.69
1m	473.21	22.25	0.123	10.73	-	-
5m	471.48	22.13	0.124	8.6	9.30	0.73
10m	471.90	22.52	0.125	6.9	-	-
30m	471.59	23.23	0.130	6.7	9.18	0.72

Table 5.2. Summarized peak positions, full width at half maximum of spectra (FWHM), photoluminescence quantum yield (PLQY) and statistics of size distribution of PeNCs synthesized with different growth time.

Though the injection temperature governed the mean size and FWHM of PeNCs, there are other factors which could have affected the bandgap and FWHM of PeNCs in the synthesis process. In general, the growth time affects the mean size and size distribution in hot injection methods.[108] The growth time (5 s to 30 min) was controlled by maintaining the injection temperature at 160 °C, but **Figure 5.5** shows that there were no significant differences in PL spectra with growth time control. Furthermore, the size distributions of PeNCs with different growth times were similar (**Figure 5.6**, **5.7** and **Table 5.2**).

Since the halide ratio in perovskites affect the bandgap, the precursor halides in the synthesis process could affect the FWHM. Therefore, the relationship between the FWHM and the precursor halide ratio at the same injection temperature was also investigated, but there was a negligible difference (**Figure 5.8** and **Table 5.3**).

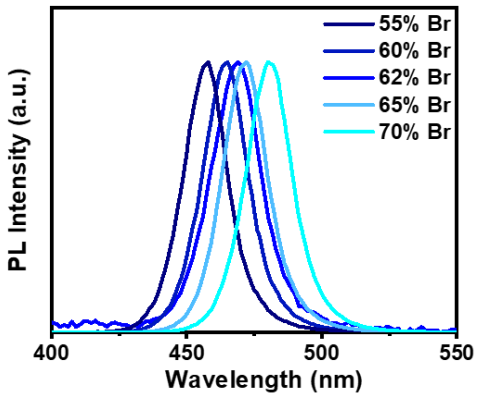

Figure 5.8. PL spectra from the PeNCs synthesized with different ratio of precursor halides at same injection temperature (160 ℃).

Halide Ratio (Br %)	Peak (nm)	FWHM (nm)	FWHM (eV)
55%	456.94	20.28	0.120
60%	464.28	21.07	0.121
62%	471.20	23.80	0.133
65%	471.60	20.79	0.116
70%	480.45	21.17	0.114

Table 5.3. Summarized peak positions and full width at half maximum of spectra (FWHM) of PeNCs synthesized with different precursor halide ratio.

Surface passivation with ligand exchange and anion passivation of PeNCs were widely applied for further improvements. The surface defects could result in the broadening of the FWHM of the emission spectra, due to the disorder of the band structure by trap states, and decrease the luminescence quantum yields as well. We tried to passivate the surface defects with the surface passivation process by using the anion exchange method with some modifications.[55] The surface passivation process was conducted with halide solvents and nucleophilic ligands. The halides were detached from the halide solvents by ligands to passivate the anion defects on the PeNCs. To maintain the luminescence peak, the halide solvent ratio was carefully controlled. To maintain the blue colour emission, mixed halide solvents (chloroform and bromoform) were used as anion sources. Meanwhile, nucleophilic ligands played an important role of passivating ligands and the reaction catalyst. However, the length of the alkyl chain of the ligand might affect the passivation ability, due to steric hinderance. Thus, nucleophilic ligands with different alkyl chain lengths (tributylphosphine (TBP), trihexylphosphine (THP) and trioctylphosphine (TOP)) were applied to see the difference of the ligand passivation ability on the surface of the PeNCs. Pristine PeNCs synthesized at 160 °C injection temperature (PR-160) were used for the comparison because they showed a clear cubic shape and stable dispersity in the solution state. By adjusting the nucleophilic ligands in the surface passivation process, we obtained surface passivated PeNCs (SP-TOP, SP-THP, SP-TBP) while maintaining the original luminescence peak of the PeNCs at around 470 nm.

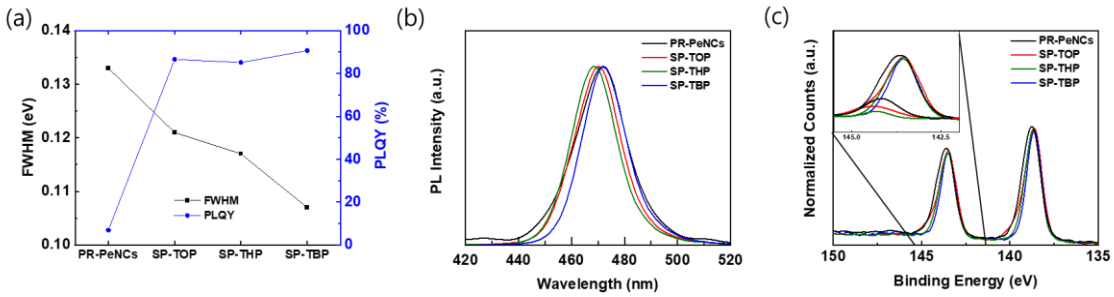

Figure 5.9. (a) Optical property tendency (PLQY and FWHM), (b) photoluminescence (PL) spectra and (c) X-ray photoelectron spectroscopy (XPS) spectra at the Pb 4f peak region (the inset spectra show deconvoluted shoulder defect peaks) of the pristine (PR) PeNCs and the surface passivated (SP) PeNCs with the assistance of ligands with different alkyl chain lengths (i.e., the SP-TOP sample was passivated with the assistance of TOP).

	Peak (nm)	FWHM (nm)	FWHM (eV)	PLQY (%)
PR-160	471.20	23.80	0.133	6.90
SP-TOP	469.86	21.54	0.121	86.57
SP-THP	468.52	20.67	0.117	85.12
SP-TBP	472.42	19.27	0.107	90.66

Table 5.4. Summarized peak positions and full width at half maximum of spectra (FWHM) of PeNCs with surface passivation assist of nucleophiles with different alkyl chain lengths.

As expected, the PLQY value was increased with all three nucleophilic ligands and they showed similar optical values (**Figure 5.9a** and **Table 5.4**). The FWHM of the emission spectra decreased with decreasing alkyl chain length (Fig. 2a and b). We expected that a higher PLQY would be obtained with a narrower FWHM because of passivated defects, but the result showed a weak relation between the PLQY and the FWHM of PeNCs. Thus, we assumed that surface passivation should be categorized as anion passivation and ligand passivation which might affect the PLQY and FWHM separately for deeper analysis.

The anion passivation ability was similarly high, regardless of the ligands, due to the sufficient supply of halide anions. Therefore, the possible anion vacancies were almost passivated for all SP-PeNCs and they showed similar high PLQY results. The ligand passivation ability could be different due to the alkyl chain length of the ligands. The shorter ligands could be attached more on the surface of the PeNCs and more ligand vacancies could be passivated, due to steric hinderance. At this point, we conclude that the FWHM was more related to the defects from the ligand vacancies and the PLQY was more related to the defects from the anion vacancies. This was beyond our expectations because a narrower FWHM could be expected with higher PLQY by filled trap states, but the ligand vacancies seemed to be the main broadening factor of the FWHM of the emission spectra.

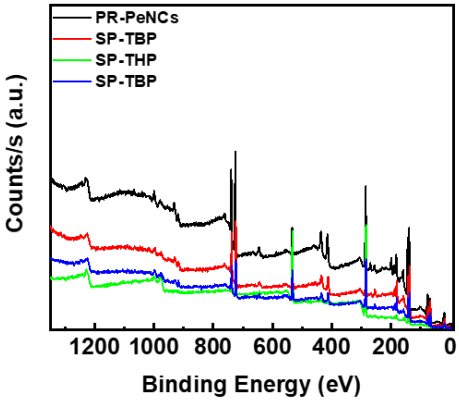

Figure 5.10. XPS Survey spectra of the pristine (PR) PeNCs and the surface passivated (SP) PeNCs with assist of ligands with different alkyl chain lengths, (i.e., SP-TOP sample was passivated with assist of TOP).

	Cs	Pb	Br	Cl
PR-160	1	0.810	1.87	1.39
SP-TOP	1	0.757	2.15	1.57
SP-THP	1	0.791	2.01	1.51
SP-TBP	1	0.780	2.13	1.56

Table 5.5. Summarized atomic ratio of PeNCs with surface passivation assist of nucleophiles with different alkyl chain lengths calculated from the XPS measurement. Normalized with the Cs peak.

To find the evidence of ligand passivation, XPS measurements were conducted (**Figure 5.9**, **Figure 5.10,** and **Table 5.5**). **Figure 5.9c** shows the XPS spectra at the Pb 4f region. The shoulder of the peak of Pb decreased with decreasing alkyl chain length (inset of **Figure 5.9c**). The shoulder peak was mainly oriented from Pb–OH and/or Pb–O, which could be generated from the exposed surface of the PeNCs by vacancies.[109, 110] The result indicates that the shorter ligands passivated the vacancies at the Pb atom on the surface of the PeNCs. The FTIR measurement was also conducted to find the evidence of the ligand passivation (**Figure 5.11**). The peaks from the P–C bond of the unbound ligands appeared at around 720 cm^{-1}, and there was a significant peak from the SP-TOP samples and a weak shoulder from the SP-THP and SP-TBP samples. The peaks from the P–C bond of the bound ligands usually appear at the shorter wavenumber region around 700 cm^{-1}, which were clearly shown with the SP-TBP sample, while SP-TOP and SP-THP samples showed weak shoulder peak.[111] These results support that the shorter ligands were attached more on the surface of PeNCs and induced more ligand passivation.

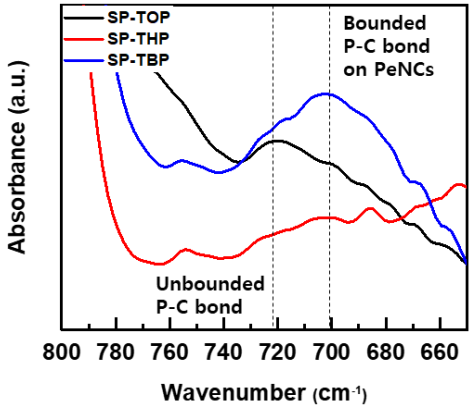

Figure 5.11. FTIR spectra around P-C bond region from surface passivated PeNCs assist of different nucleophiles with varying alkyl chain lengths.

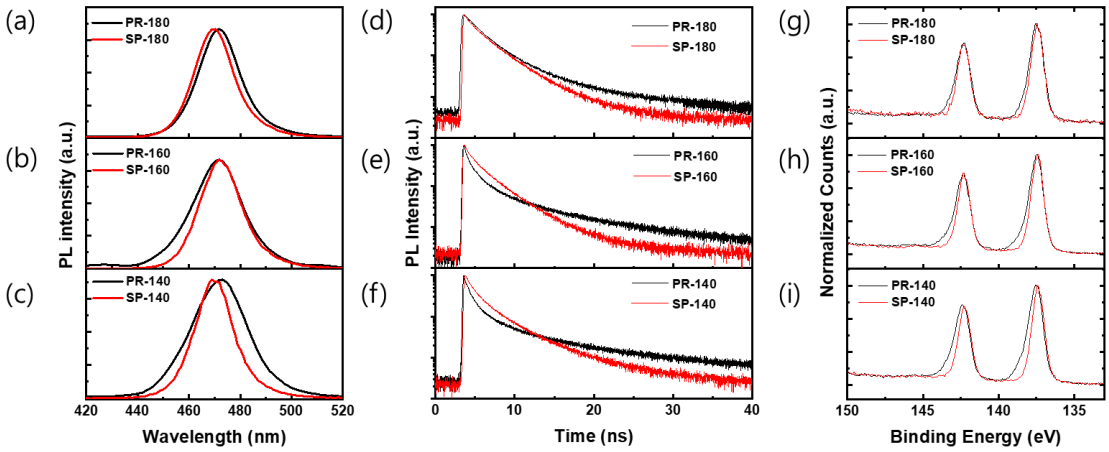

Figure 5.12. (a–c) Photoluminescence (PL) spectra, (d–f) time-resolved PL lifetime and (g–i) XPS spectra of the Pb 4f region from the pristine (PR) and surface passivated (SP) PeNCs with different injection temperature conditions (i.e., PR-140 samples were synthesized at 140 °C and SP-140 samples were the results of the surface passivation of PR-140).

	Peak (nm)	FWHM (nm)	FWHM (eV)	PLQY (%)
PR-140	471.89	27.06	0.151	7.80
SP-140	469.79	18.69	0.105	78.83
PR-160	471.20	23.80	0.133	6.90
SP-160	472.42	19.27	0.107	90.66
PR-180	471.86	20.22	0.113	11.26
SP-180	469.88	19.38	0.109	86.35

Table 5.6. Summarized peak positions and full width at half maximum of spectra (FWHM) of PeNCs before (PR) and after surface passivation (SP) with different injection temperatures.

As the surface passivation with PR-160 PeNCs showed an improved FWHM, a further narrower FWHM was expected with the surface passivation on PR-180 PeNCs. However, the FWHM narrowing effect was less, or there was no effect with PeNCs at higher injection temperatures (**Figure 5.12a–c** and **Table 5.6**). The PR-PeNCs (PR-140, PR-160 and PR-180) showed a narrower FWHM with increasing injection temperatures, as shown above, and all surface passivated PeNCs with TBP (SP-140, SP-160 and SP-180) showed similar FWHM at around the 0.1 eV level, irrespective of the injection temperature. Interestingly, the PeNCs with a wider FWHM from lower injection temperature showed a dramatic decrease in the FWHM after surface passivation (**Figure 5.12c**). The possible origin of the difference might be the surface area of the PeNCs. In the hot-injection method, higher injection temperature induces an increased mean size and mean volume of the nanocrystal. For an equal mass of precursors, the PeNCs with larger mean size have smaller surface area than that of the PeNCs with smaller mean size. Therefore, the surface-to-volume ratio is smaller with PeNCs synthesized at higher injection temperatures. The main origin of the defects of the PeNCs is the vacancies on the surface of the PeNCs, not in the inside of the PeNCs. Thus, with smaller size PeNCs, larger amounts of ligand defects were passivated and dramatic narrowing of the FWHM of PeNCs was observed as shown in **Figure 5.12c**.

	Cs	Pb	Br	Cl
PR-140	1	0.771	2.03	1.38
SP-140	1	0.723	2.19	1.61
PR-160	1	0.810	1.87	1.39
SP-160	1	0.780	2.13	1.56
PR-180	1	0.937	2.02	1.49
SP-180	1	0.851	2.00	1.45

Table 5.7. Summarized atomic ratio of PeNCs before (PR) and after surface passivation (SP) with different injection temperatures calculated from the XPS measurement. Normalized with the Cs peak.

	τ_1 (ns)	f_1 (%)	τ_2 (ns)	f_2 (%)	τ_{ave} (ns)	χ^2
PR-140	1.31	83.24	10.80	16.76	2.90	1.79
SP-140	1.40	69.31	4.88	30.69	2.47	1.27
PR-160	1.39	83.25	9.87	16.75	2.81	1.63
SP-160	1.42	55.95	3.72	44.05	2.44	1.10
PR-180	2.21	88.75	8.34	11.25	2.90	1.54
SP-180	1.79	61.14	4.04	38.86	2.66	1.13

Table 5.8. Parameters of biexponential fitting for time-resolved PL lifetime of pristine (PR) and surface passivated (SP) PeNCs synthesized with different injection temperatures. f_1 and f_2 are percent contributions of lifetimes, fast-decay τ_1 and slow-decay τ_2 respectively.

A time-correlated single-photon counting measurement (TCSPC) was conducted to find the effect of the surface passivation on the surface and body parts of the PeNCs (**Figure 5.12d–f** and **Table 5.7**). **Table 5.8** presents the PL decay times that were fitted to the biexponential decay with parameters of short lifetime, τ_1, long lifetime, τ_2, and the corresponding percent contributions, f_1 and f_2. The PL decay showed a significant difference between PR-PeNCs and SP-PeNCs. The mean lifetime was similar at around 3 ns for all PeNCs, but the ratio of f_1 and f_2 was different. For all SP-PeNCs, the proportion of the surface part of the trap-assisted part (f_1) was remarkably decreased, while that of the body part of the radiative part (f_2) was increased, regardless of the injection temperature.[112] The decreased f_1 directly indicates reduced surface defects on the PeNCs after surface passivation. It seems that the PL decay

properties were not affected by the surface-to-volume ratio but affected only by surface passivation. This result matches with the tendency of the PLQY measurement results, which supports that optoelectronic performances are related to the anion vacancies.

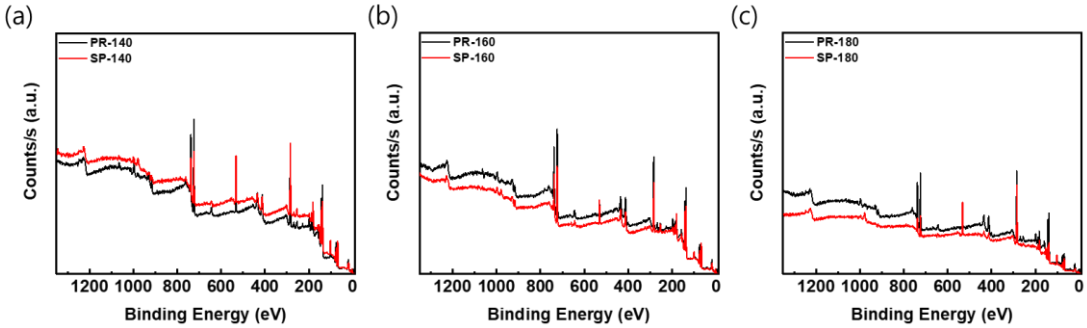

Figure 5.13. XPS Survey spectra of the pristine (PR) and the surface passivated (SP) PeNCs with different injection temperature conditions (i.e., PR-140 samples were synthesized at 140°C and SP-140 samples were surface passivated result of PR-140).

XPS measurement was conducted with PR-PeNCs and SP-PeNCs synthesized at different injection temperatures and this is shown in **Figure 5.12g–i** and **Figure 5.13**. As shown in **Figure 5.9**, the shoulder defect peak of Pb was decreased in the SP-PeNCs. The PR-PeNCs synthesized at higher injection temperature exhibit a weaker shoulder defect peak due to the lower surface-to-volume ratio and resulted in less decrease of the shoulder peak by surface passivation (PR-180 and SP-180 in **Figure 5.12g**). However, the PeNCs which have a higher surface-to-volume ratio showed a dramatic reduction of the shoulder defect peak (PR-140 and SP-140 in Fig. 3i) by surface passivation. The ligand passivation effect of surface passivation reduced the defects on the Pb atoms of PeNCs and narrowed the FWHM of the emission spectra.

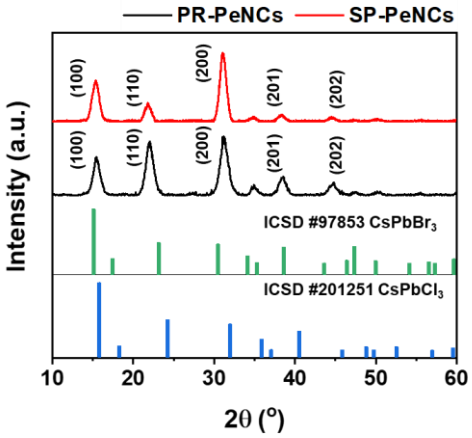

Figure 5.14. XRD pattern of the pristine (PR) and surface passivated (SP) PeNCs.

We tried to apply the improved optoelectrical properties of PeNCs to devices. Before device

fabrication, the non-destructive character of the surface passivation treatment was investigated. The surface passivation process did not alter the crystal structures, as confirmed by the XRD measurement (**Figure 5.14**), and the differences of the mean size and the size distribution between PR-PeNCs and SP-PeNCs were also negligible (**Figure 5.15** and **5.16**). As the surface passivation was non-destructive, a comparison of electrical properties between PR-PeNCs and SP-PeNCs was possible.

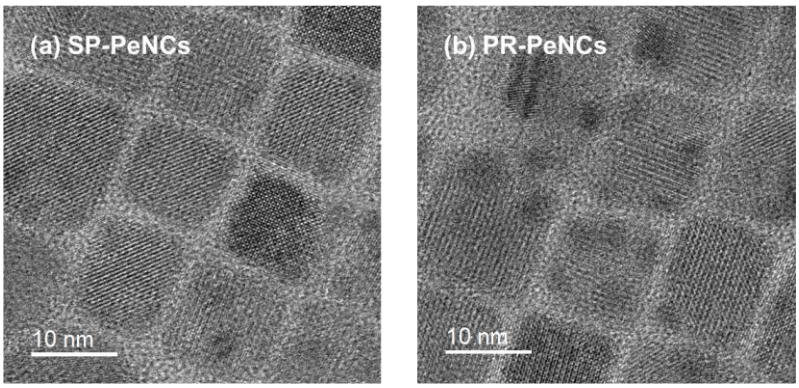

Figure 5.15. TEM images of the (a) pristine (PR) and (b) surface passivated (SP) PeNCs.

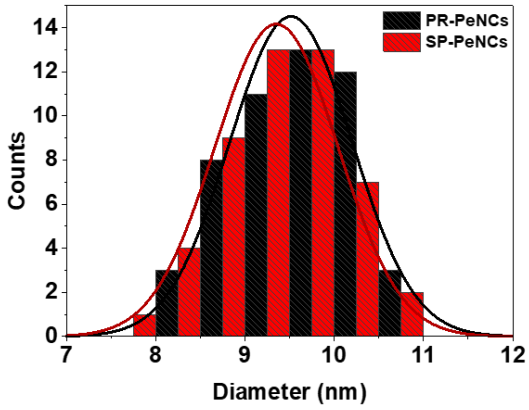

Figure 5.16. Size distribution of the pristine (PR) and surface passivated (SP) PeNCs.

The surface passivation effects on the electrical properties of PeNCs were also observed. **Figure 5.17a** shows the improved conductivity of the PeNCs films with the surface passivation treatment. The space charge limited current (SCLC) measurement was conducted to confirm the enhanced electrical properties of the PeNC film by surface passivation. As shown in **Figure 5.17b** and **c**, an electron-only device was fabricated and measured. The voltage at the trap-filled limit (V_{TFL}) is proportional to the density of the trap states.[104] The V_{TFL} value of the device with surface passivated PeNCs was 0.31 V, which was lower than the V_{TFL} value of the PR-PeNCs, which implies reduced trap states and improved charge transport by surface passivation. We found that surface passivation made the PeNCs have less

aggregation, as confirmed with more ligand coverage (**Figure 5.18**), reduced absorption from the scattering (**Figure 5.19**), and significantly smoother surface of the film of SP-PeNCs (**Figure 5.20**), which supports the reason for improved charge transport behaviour.

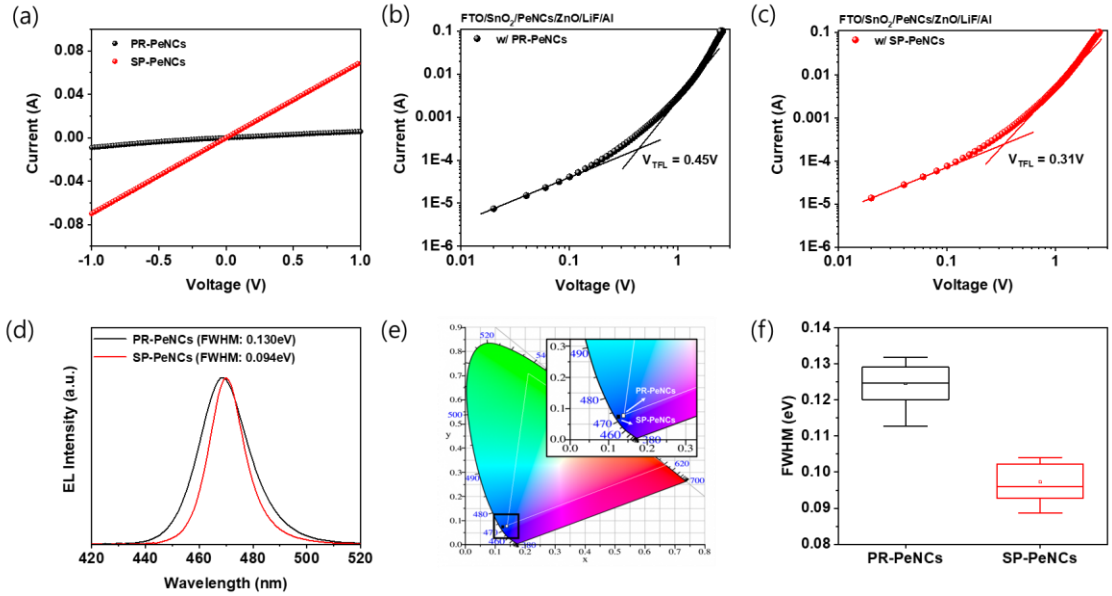

Figure 5.17. Characteristics of PeLEDs. (a) I–V behavior of pristine (PR) and surface passivated (SP) PeNCs. The SCLC response of (b) PR-PeNCs and (c) SP-PeNCs. (d) EL spectra with PR-PeNCs and SP-PeNCs. (e) The CIE chromaticity diagram of PR- and SP-PeNCs. (f) Comparison of the FWHM values, with box plots, PR-PeNC- and SP-PeNC-based LEDs. The standard deviation, a metric for reproducibility, improved from 0.1245 ± 0.0056 eV for PR-PeNC-based PeLEDs to 0.0973 ± 0.0055 eV for SP-PeNC-based PeLEDs.

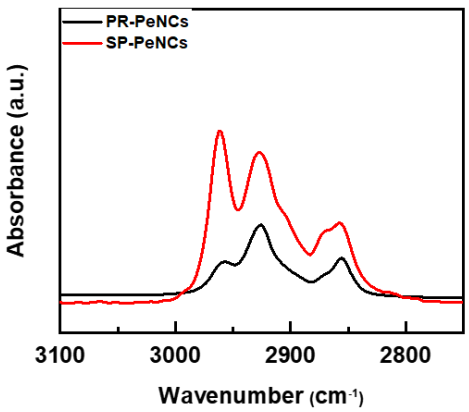

Figure 5.18. FTIR spectra around C-H bond region from surface passivated PeNCs assist of different nucleophiles with varying alkyl chain lengths.

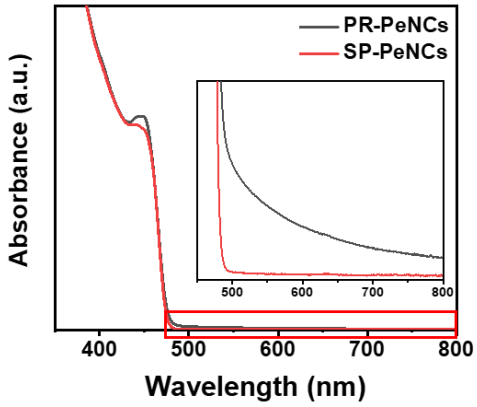

Figure 5.19. Absorption spectra from the pristine (PR) and surface passivated (SP) PeNCs. (inset. lower intensity region of the absorption spectra.)

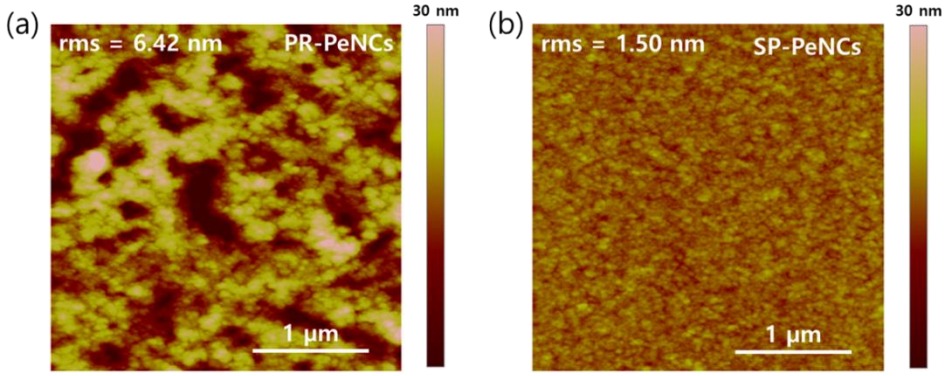

Figure 5.20. AFM topographical images of the (a) pristine (PR) and (b) surface passivated (SP) PeNCs.

The PeLEDs were fabricated with the PR-PeNCs and SP-PeNCs, and their electroluminescence (EL) spectra and related Commission Internationale de l'Eclairage (CIE) chromaticity diagram are shown in **Figure 5.17d** and **e**. As shown in the PL spectra, the PeLEDs with SP-PeNCs showed a narrower EL spectrum (FWHM = 0.094 eV) than that of the PR-PeNCs (FWHM = 0.130 eV). The reproducibility of the EL spectra of PeLEDs was tested for 12 devices, as shown in **Figure 5.17f**. The PeLEDs with SP-PeNCs showed lower mean FWHM and standard deviations. The operational spectral stability was measured and is shown in **Figure 5.21** The PeLEDs based on SP-PeNCs showed a little shift and broadening. However, the PeLEDs based on the PR-PeNCs exhibited a severe peak shift and broadening due to the less coverage of ligands. Through device measurements, the surface passivation treatment resulted in filled trap states, enhanced electrical properties and improved optical properties. From the above results, the quality of the PeLEDs was determined by the surface passivation of PeNCs. The surface passivation of PeNCs eventually increases the quality of PeNCs, which also increases the

quality of PeLEDs.

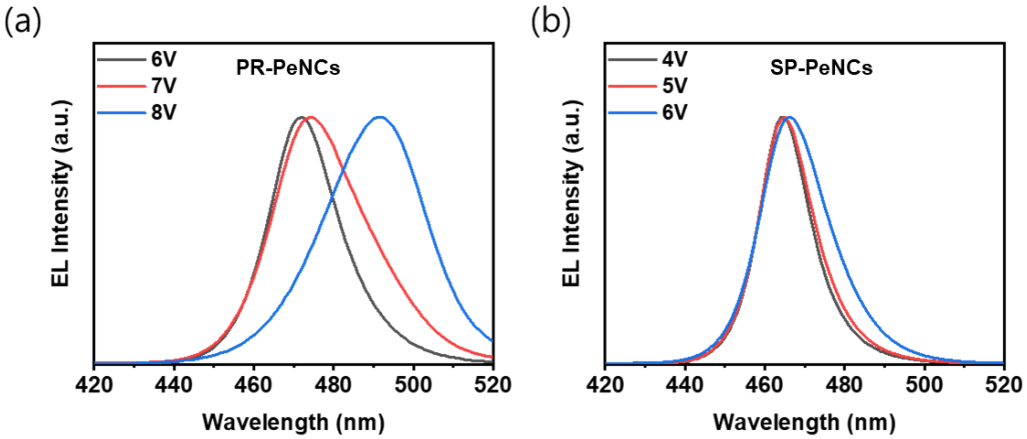

Figure 5.21. Operational spectra stability of the PeLEDs based on the pristine (PR) and surface passivated (SP) PeNCs.

5.4 Conclusion

In summary, we studied the origin of the narrow emission spectra of PeNCs with the surface passivation method. We found that the mean size of PeNCs mainly affects the FWHM of luminescence, but the size distribution of PeNCs does not have much effect. With surface passivation, the optoelectrical properties of PeNCs were improved and the FWHM was narrowed. The surface passivation was analysed in two parts: anion passivation and ligand passivation. The ligand passivation affected the ligand vacancies and the FWHM. For the shorter alkyl chain ligands, higher ligand passivation was observed. The anion passivation had less effect on the FWHM but had more effect on the optoelectronic properties. The passivated defect sites were confirmed by TSCPC, XPS and SCLC response measurements. We successfully fabricated blue PeLEDs with narrow FWHM (0.094 eV, 16.72 nm). Our study could provide clues to achieve PeLEDs with highly saturated colours for further display applications.

CHAPTER 6. Cs-base Inorganic Bulk Blue Perovskite LEDs with Anion-exchange Method

The content of this chapter is in preparation for the publication in a journal.

6.1 Research background

Lead halide perovskites have been intensively researched for optoelectronic devices applications due to the advantages of cheap precursor materials, easy process and superior optoelectronic properties.[15, 24, 31, 92] Especially, the perovskite light-emitting diodes (PeLEDs) are considered as promising candidate for the next generation displays with attractive properties, such as easily tunable bandgap, high color purity and high carrier mobility.[113, 114] Recently, the PeLEDs are rapidly developed and the external quantum efficiency (EQE) of the PeLEDs were achieved over 20% for green and red color.[10, 12] However, the blue PeLEDs are showing relatively slow development. The highest EQE of PeLEDs are just over 10% for sky-blue color (~490nm) and below 5% for deep-blue color (~470 nm). Most of research on the blue PeLEDs are based on the low-dimensional perovskites, such as quasi-2D structure and nanoparticles.[26, 47, 93, 105, 115, 116] The blue PeLEDs based on the low-dimensional perovskite structure could control the bandgap by controlling the size of the perovskite crystal and achieved wide bandgap for blue emission. However, the low-dimensional perovskites contain organic molecules which limits electronic properties and exhibits wider or extra peaks in luminescence spectra.

Though the blue PeLEDs with low-dimensional perovskites with organic molecules showed better performance than the bulk perovskites for now, but the bulk PeLEDs still have potential in the process cost and better electrical properties from the absence of the organic molecules. For comparison, the hole mobility of $MAPbI_3$ perovskite nanocrystals was reported as 3.83×10^{-4} $cm^2V^{-1}S^{-1}$,[117] while the bulk $MAPbI_3$ perovskite films reported the value as 2.83 $cm^2V^{-1}S^{-1}$,[118] and single crystalline $MAPbI_3$ perovskite recorded the value of 164 $cm^2V^{-1}S^{-1}$ with the space-charge limited current (SCLC) measurements.[119] The mobility tendency was predictable results, because the electrical charge should hop the gap between the perovskite crystals to flow. Therefore, the less gap between the crystals of the perovskites, the better device performance could be achieved.

However, there are few reports on blue PeLEDs with bulk structure with limited performances.[120, 121] One of big huddles to overcome to fabricate the bulk perovskite film for blue emission is hard to make high-quality films. With the inorganic precursors, perovskite films showed low film coverage due to the low solubility of inorganic precursors. To overcome the coverage problem, organic cations, such as

methylammonium (MA) or formamidinium (FA), were used and the device performances were improved with higher film coverage.[121] However, degradation with environmental factors is the remaining issue of the organic cation base perovskites, while the Cs-based or Cs-participated perovskite reported advanced long-term stabilities.[122] Therefore, for the higher device performance and the device stability, the bulk inorganic perovskites could be the suitable material for perovskite optoelectronics.

In this work, we have developed fabrication method for the blue perovskite LEDs with the bulk inorganic halide perovskite with anion exchange method. Because the inorganic chlorine source is hardly soluble in most of solvents, we applied anion exchanging technique to obtain the chlorine containing blue emissive perovskite film. The halides of bulk film were exchanged maintaining the genuine properties of perovskites. The anion exchanged bulk film showed nice spectral stability from the suppressed halide segregation. We have successfully fabricated blue PeLEDs with these films with 494 cd/m^2 of maximum luminance in 470 nm emission condition and 1.80% of EQE in 490 nm emission condition.

6.2 Experimental details

Anion Exchange Treatment

The anion exchange treatment was based on the Yoon et al.[55] with adjustments. Overall process was conducted in N_2-filled glove box. To exchange the bromines in the perovskite films, the 0.1% tributylphosphine in chloroform solution was used as reaction solution. The perovskite films were dipped into the reaction solution. The reaction time was tuned to targeted emission condition. Then the anion exchanged films were washed with toluene.

Device Fabrication

The precleaned patterned ITO glass substrates were treated with UV-ozone for 15 min to make the surface hydrophilic, and poly(3,4-ethylenedioxythiophene):polystyrene sulfonic acid (PEDOT:PSS) solution as hole injection layer (HIL) was spin-coated at 3000 rpm for 40 s and annealed at 150 °C for 15 min. In N_2-filled glove box, the as-prepared perovskite precursor solution was deposited onto the HIL film through a one-step process at 4000 rpm for 1 min and annealed at temperature of 120 °C for 10 min to remove the residual DMSO solvent. After perovskite deposition, anion exchange treatment was conducted. Finally, TPBi (40 nm), LiF (1 nm), and Al (100 nm) were thermally deposited sequentially under high vacuum (< 10^{-6} Torr). The active area of the device was 13.5 mm^2.

Characterization

UV-Vis-NIR Absorption and Photoluminescence (PL) Measurements

UV-Vis-NIR absorption spectra were obtained by using a Cary 5000 (Agilent) spectrophotometer and the photoluminescence spectra were measured with an nF900 instrument (Edinburgh Photonics) with a xenon lamp as an excitation source.

Photoluminescence quantum yield (PLQY)

The PLQY values were obtained with QE-2000 from Otsuka Electronics Co., Ltd.

Transmission Electron Microscopy (TEM)

Transmission Electron Microscopy (TEM) images were recorded by using JEM02100 and JEM-2100F from JEOL. The samples which were washed with butanol one time and re-dispersed in toluene dropped onto carbon coated Cu grids from Ted Pella, Inc.

Fourier Transform Infrared Spectroscopy (FTIR)

Fourier Transform Infrared Spectroscopy (FTIR) spectra were performed using a Cary 670 FTIR spectrometer (Agilent).

High Power X-Ray Diffraction (XRD)

XRD patterns were obtained by using a high-power diffractometer (D/MAX2500V/PC from Rigaku) with settings including 40 kV potential, 200 mA current, Cu-rotating anode, Cu Kα radiation, (λ = 0.1542 nm) using a graphite monochromator and a scintillation counter.

Time-correlated single-photon counting (TCSPC)

Time-resolved and steady-state PL spectra were measured by using FluoTime 300. The samples were photoexcited with a 375 nm continuous wave and pulsed diode laser head (LDH-D-C-375). The PL decay curves were fitted to a biexponential decay model using software, FluoFit.

Time of flight- Secondary Ion Mass Spectrometry (TOF-SIMS measurement)

TOF-SIMS measurements were conducted by using TOF-SIMS 5 from ION TOF.

Xray and Ultraviolet photoelectron spectroscopy (XPS and UPS)

XPS and UPS measurements were conducted with ESCALAB 250XI.

Surface characterization

The surface morphology was scanned using an atomic force microscope (AFM) of VEECO Dimension 3100 equipped with Nanoscope V.

Device measurement:

LED measurements were performed using a Keithley 2400 source measurement unit and a Konica Minolta spectroradiometer (CS-2000, Minolta Co.)

6.3 Result and discussion

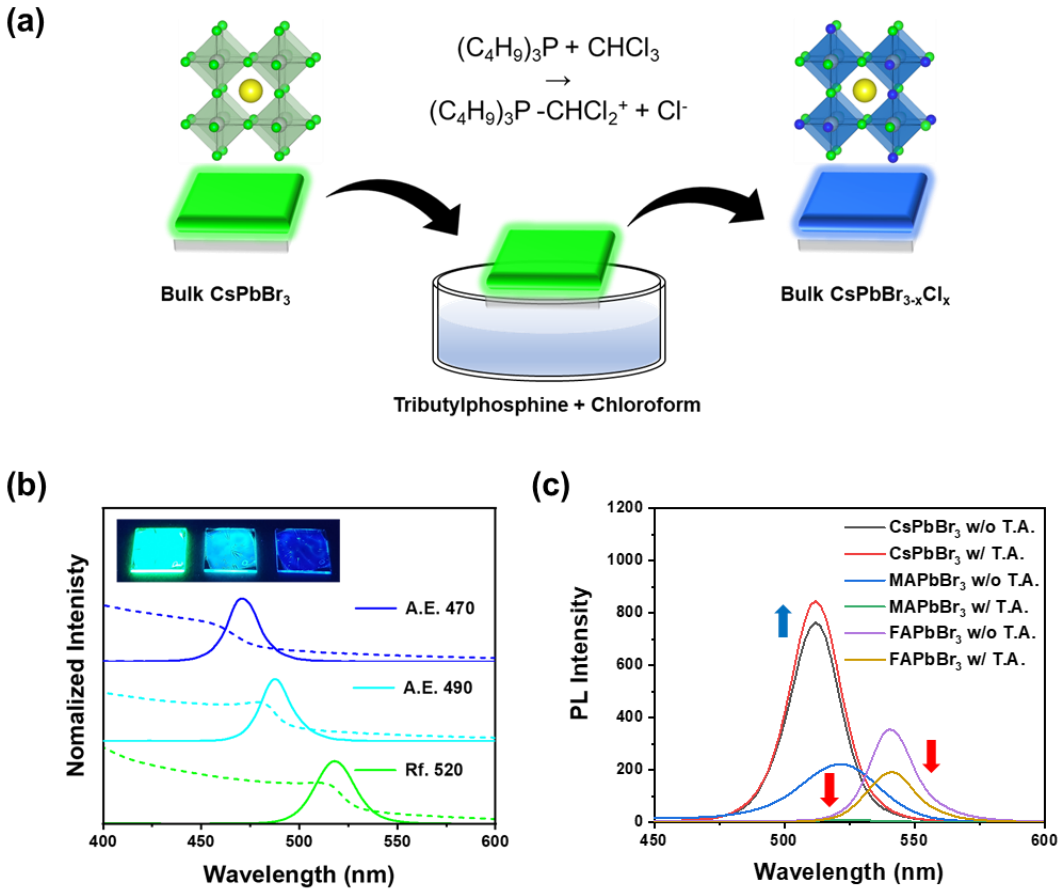

Figure 6.1. Scheme and optical properties. (a). Scheme of the anion exchange method for blue-emitting bulk perovskite films. (b). Uv-vis absorption and photoluminescence spectra of reference (Rf. 520) and anion-exchanged bulk perovskite films (A.E. 470 and A.E. 490 conditions). (c). Thermal stability measurements; PL spectra evolution of deposited $CsPbBr_3$, $MAPbBr_3$ and $FAPbBr_3$ perovskite films without and with thermal annealing at 100 °C.

We developed pathway to fabricate blue color emissive halide perovskite film with anion exchange method. The overall procedure was shown in the **Figure 6.1a**. In detail, the bulk $CsPbBr_3$ perovskite films were fabricated by the typical spin coating method.[123] The fabricated films were dipped into the reaction bath, chloroform (CF) and tributylphosphine (TBP) mixed solution, to exchange the halides.[55] The chlorines were detached from the CF by the TBP and exchanged with the bromines in the perovskite. Detailed exchange procedure is described below

1st step: $TBP + CHCl_3 \rightarrow TBP\text{-}CHCl_2^+ + Cl^-$ (1)

2nd step: $CsPbBr_3 + Cl^- \rightarrow CsPbBr_xCl_y + Br^-$ (2)

3rd step: $TBP\text{-}CHCl_2^+ + Br^- \rightarrow TBP + CHCl_2Br$ (3)

The TBP molecule have role of triggering the reaction and boosting the detachment of the chlorines. Then, the anion exchanged blue emissive bulk perovskite film is produced.

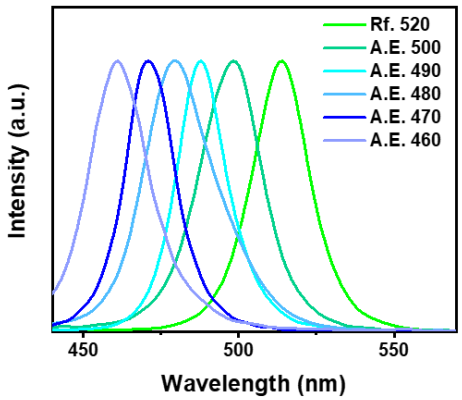

Figure 6.2. Photoluminescence spectra of reference (Rf. 520) and anion-exchanged bulk perovskite films.

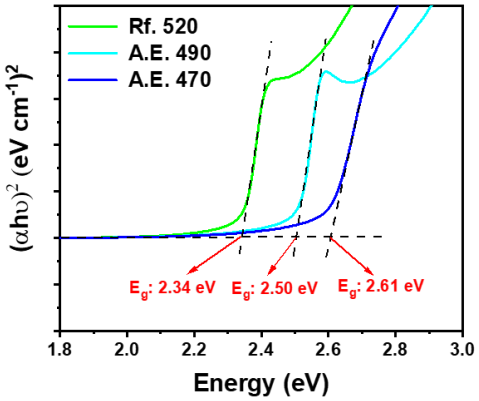

Figure 6.3. Tauc plot of reference (Rf. 520) and anion-exchanged bulk perovskite and measured optical band gaps are indicated.

The anion exchanged bulk perovskite films shows blue-shifted photoluminescence (PL) peaks (**Figure 6.2**). As the reaction proceeds with additional reaction time, the more halides in the perovskite were exchanged and the optical property of the perovskite could be tuned to near Uv region. Optical property of the anion exchanged perovskite films could easily be adjusted by reaction condition, and we focused on perovskites with emission wavelength at 470 nm and 490 nm for blue color emissive application (A.E. 470 and A.E. 490) with control of reaction time and concentration of the TBP. The optical properties, such as absorption and PL spectra, Tauc plot, of anion exchanged with targeted emission spectra were shown in **Figure 6.1b**, **Figure 6.3**. Especially, the emission widths of the perovskite films were also maintained after the halide exchange treatment.

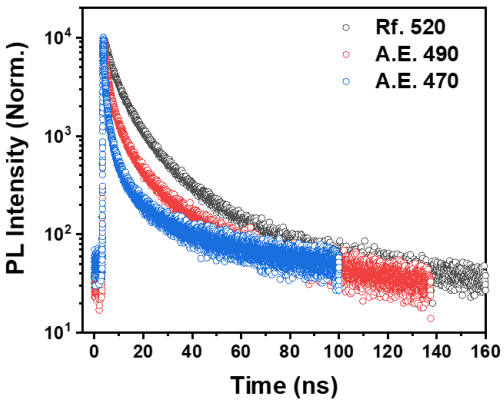

Figure 6.4. Time-resolved photoluminescence lifetime at detection wavelength 520, 490, and 470 nm of reference (Rf. 520) and anion-exchanged bulk perovskite films deposited on glass/PEDOT:PSS.

Condition	τ_1 (ns)	f_1 (%)	τ_2 (ns)	f_2 (%)	τ_{ave} (ns)	χ^2
Rf. 520	4.91	79.62	19.96	20.38	7.98	1.63
A.E. 490	2.71	80.20	16.38	19.80	5.42	1.74
A.E. 470	1.46	84.14	11.93	15.86	3.12	1.74

Table 6.1. Summarized biexponential fitting parameters for time-resolved PL lifetime of pristine and anion-exchanged bulk perovskite films deposited on glass/PEDOT:PSS; f_1 and f_2 are percent contributions of lifetimes, fast-decay τ_1 and slow-decay τ_2 respectively.

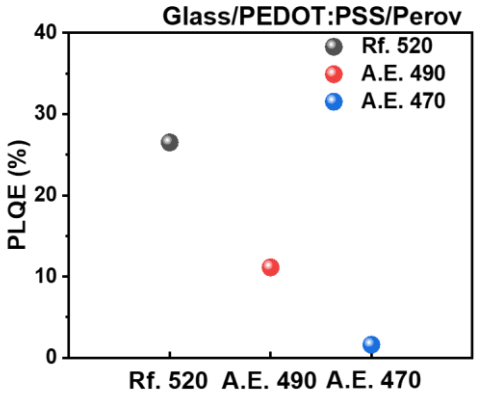

Figure 6.5. Photoluminescence quantum yield of reference (Rf. 520) and anion-exchanged bulk perovskite films.

Time-resolved PL measurements were conducted to explore the PL decay properties (**Figure 6.4** and **Table 6.1**). The PL lifetime was reduced after the anion exchange (emission wavelength of 520 → 490 or 470 nm), which is obvious result due to the increased bandgap, but interesting point was that proportion of trap-assisted part (f_1) was decreased and proportion of radiative part (f_1) was increased after the anion exchange treatment in time-resolved PL measurements. The anion exchange treatment

conducted additional treatment of supplying excess halides to the perovskites. The halide defects of the perovskite could be passivated by this effect and resulted improved PL decay property.[124] The related film photoluminescence quantum yield was also measured (**Figure 6.5**). We tried to fabricate the blue emissive bulk $CsPbX_3$ films with mixed halide precursors to compare the optical properties, however the precursors were insoluble with the DMSO solvent as mentioned (**Figure 6.6** and **6.7**), and the films were not successfully fabricated.

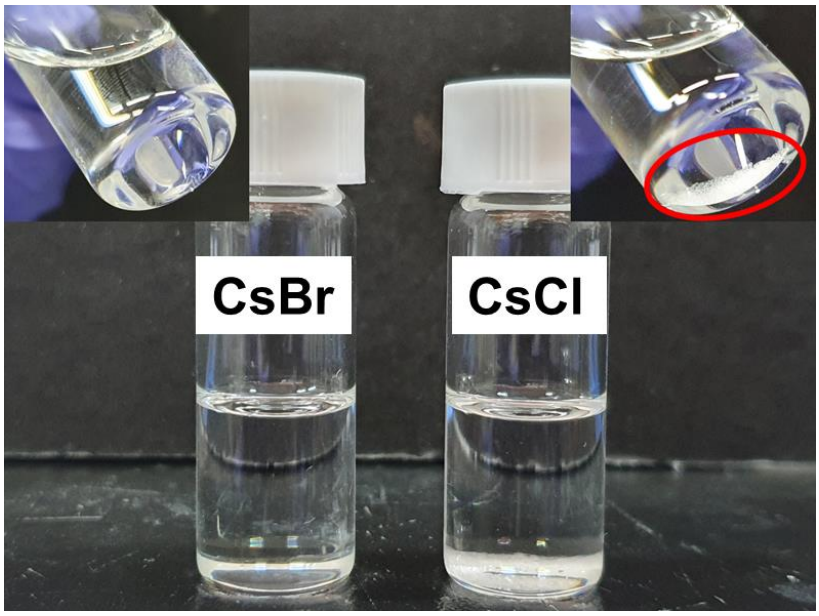

Figure 6.6. Photographs of CsBr and CsCl solution dissolved in DMSO. The concentration of CsX solutions were 30 mg mL^{-1}, respectively.

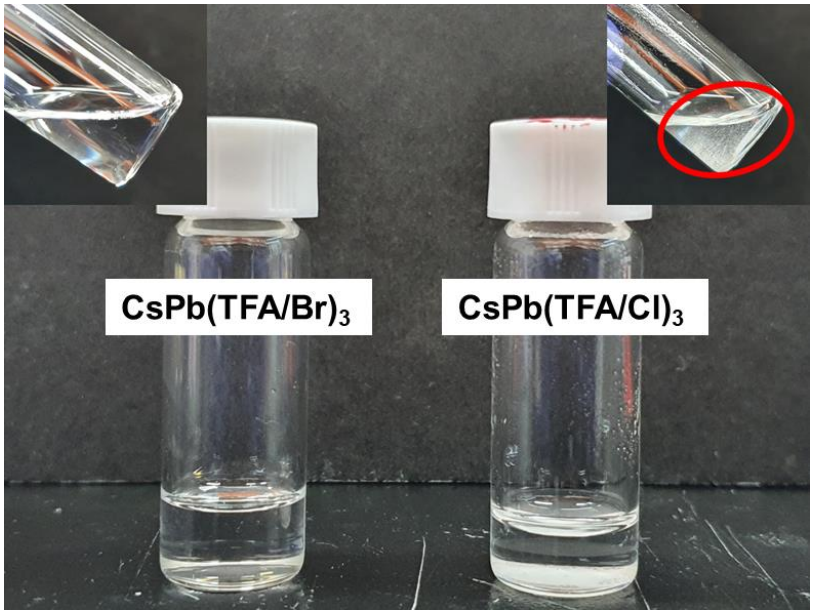

Figure 6.7. Photographs of $CsPb(TFA/Br)_3$ and $CsPb(TFA/Cl)_3$ solution dissolved in DMSO. The concentrations of solutions were 0.2M respectively.

The organic cation-based hybrid perovskite films ($MAPbBr_3$ and $FAPbBr_3$) were tested to compare

the optical properties with inorganic-cation-based perovskite ($CsPbBr_3$) films. The organic-cation-based perovskites showed relatively weaker PL spectra, and the organic-cation-based perovskite exhibited low stability to proceed the anion exchange process. The PL intensity of organic cation-based perovskite was severely damaged after 5 minutes of annealing at 100°C, while Cs base inorganic perovskite maintained original intensity and peak position (**Figure 6.1c**).

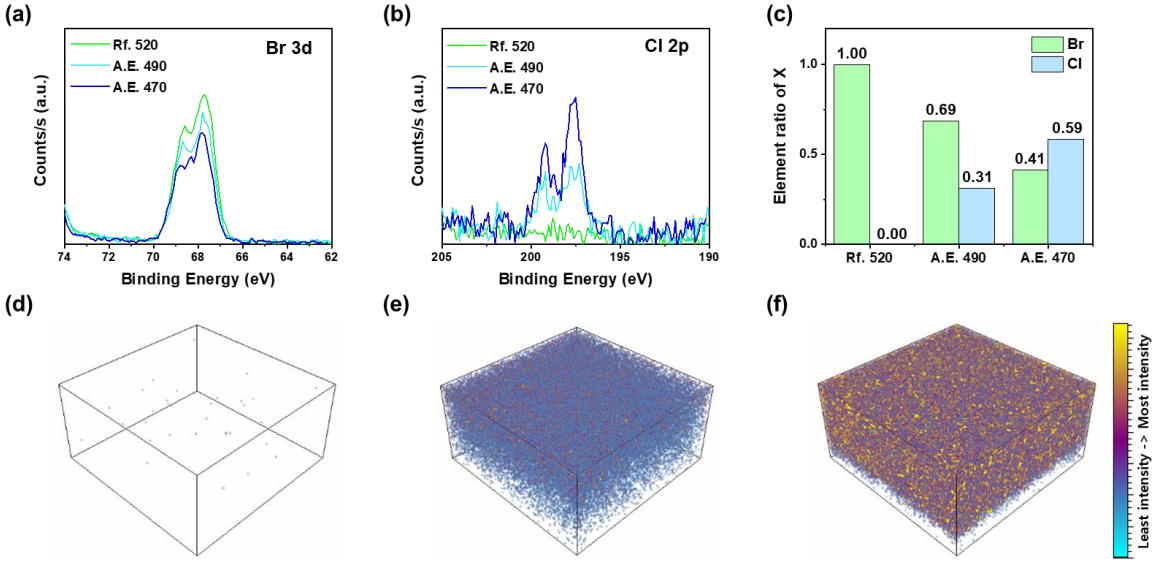

Figure 6.8. X-ray photoelectron spectroscopy (XPS) spectra corresponding to (a). Br 3d, and (b). Cl 2p, and (c). halide ratio in reference and anion-exchanged bulk perovskite films based on XPS measurement. Reconstructed TOF-SIMS elemental 3D maps for Cl^- halides traced in the depth profile; (d). reference (Rf. 520) and anion-exchanged bulk perovskite films, (e). A.E. 490 and (f). A.E. 470 conditions. The image size is 100 μm x μm in the x-y plane.

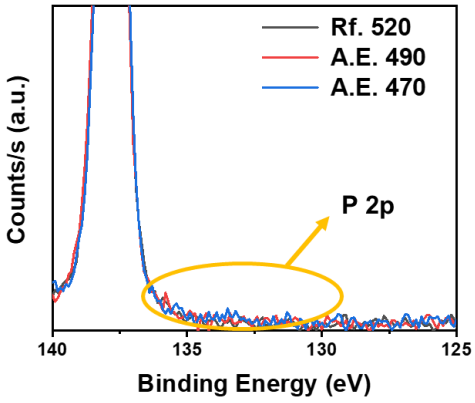

Figure 6.9. X-ray photoelectron spectroscopy (XPS) spectra corresponding to P 2p of reference (Rf. 520) anion-exchanged bulk perovskite films

To confirm the exchange of the halides in the bulk perovskite films, XPS measurements were

conducted. The XPS spectra of anion exchanged bulk perovskite films were shown in **Figure 6.8a** and **6.8b**. The peaks of anion exchanged perovskite films in the Br 3d region were weaker than the pristine $CsPbBr_3$ films and the A.E. 470 condition have weakest result, as expected. In the Cl 2p peak region, the A.E. 470 condition showed strongest peak which indicates the more chlorine contents in the films than the A.E. 490 condition and pristine films. The halide ratio was summarized in the **Figure 6.8c**. The chlorine contents in the films were increasing with more reaction time, exhibiting the more blue-shifted emission result. The TBP could be attached on the surface of the perovskite film and might passivate the A site vacancies,[124] or might disturb the current flow. We confirmed that the TBP was clearly removed with rinsing steps with XPS measurement. **Figure 6.9** displays the P 2p region of XPS spectra and anion exchanged samples did not showed any signal of phosphine elements, ensuring no obstacles to inject current to the perovskite emissive layer.

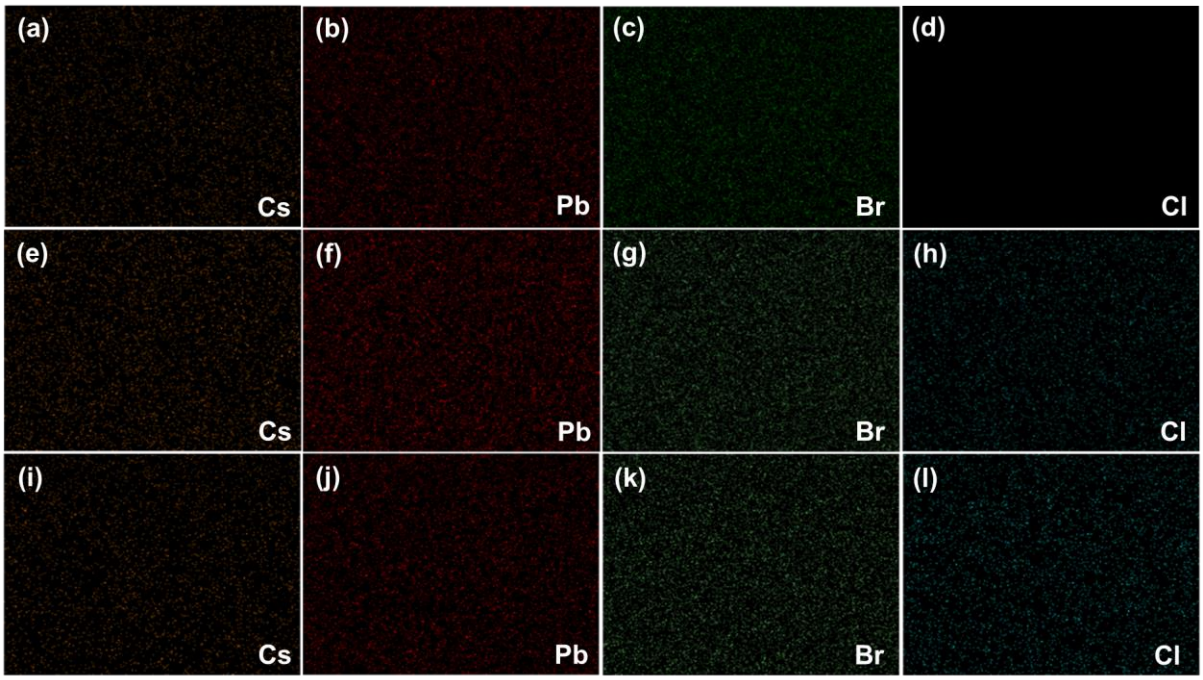

Figure 6.10. Energy-dispersive X-ray (EDX) spectroscopy images corresponding elemental mapping of Cs, Pb, Br, and Cl in (a-d) reference (Rf. 520), (e-h) anion-exchanged bulk perovskite films, A.E. 490 condition and (i-l) anion-exchanged bulk perovskite films, A.E. 470 condition.

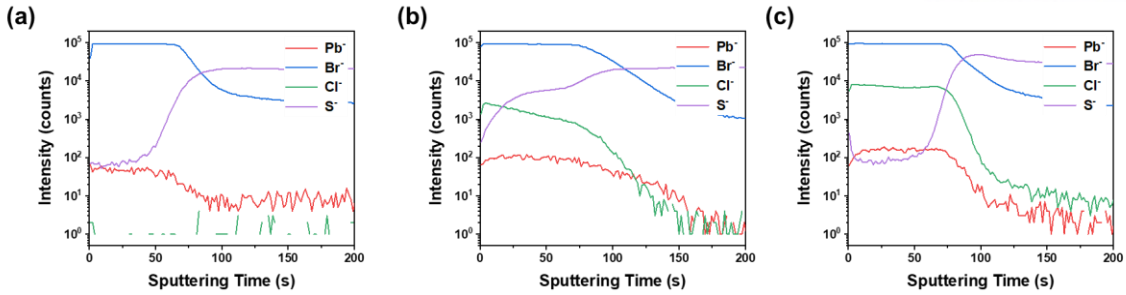

Figure 6.11. Negative ion TOF-SIMS spectra and depth profiles of (a). reference (Rf. 520) and anion-exchanged bulk perovskite films, (b). A.E. 490 and (c). A.E. 470 conditions.

To prove the anion exchange, TOF-SIMS measurement was conducted evenly over the film. **Figure 6.8d-6.8f** shows the TOF-SIMS tomography result of the anion exchanged bulk perovskite films for the chlorine contents, blueish color indicates the lower contents and yellowish color indicates the higher contents. The result clearly shows the chlorines were exchanged evenly over the surface. This result also supports the EDX measurement (**Figure 6.10**). Moreover, the halides were fully exchanged into the deep films, not only on the surface of the films. Seeing the depth profile result of TOF-SIMS measurement, the chlorines were evenly exchanged into the films and showed similar chlorine contents regardless of depth (**Figure 6.11**). Considering the mechanism of the anion exchange, the anion exchange occurs at the surface of the perovskite film. Then, the exchanged halides are easily mixed into the perovskite crystals, and this phenomena were reported with the nanocrystals.[55, 98, 125-127] Our result ensures that the exchanged halides were easily mixed into the inside of crystals even in the solid film states.

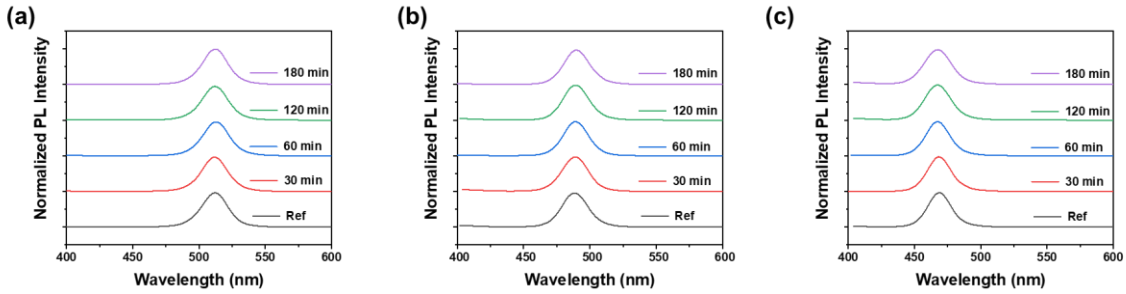

Figure 6.12. Spectral stability measurements; PL spectra evolution of (a). reference (Rf. 520) and anion-exchanged bulk perovskite, (b). A.E. 490 and (c). A.E. 470 conditions after continuous thermal annealing at 100 °C for different times.

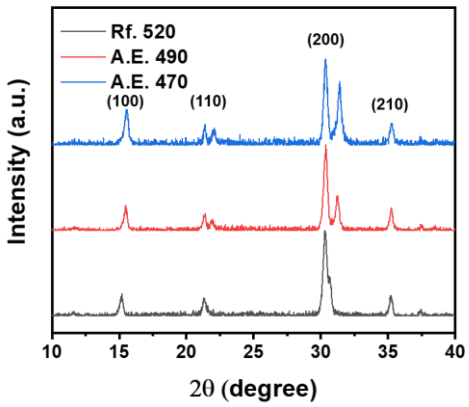

Figure 6.13. XRD pattern of reference (Rf. 520) and anion-exchanged bulk perovskite films.

As a halide segregation is a big issue in the mixed halide perovskites,[105, 128-131] the thermal spectral stability was tested **(Figure 6.12**). The anion exchanged perovskite films were annealed at 100℃ in ambient condition to accelerate the movement of halides. The PL peaks of anion exchanged bulk perovskite[129] films were maintained at original position for hours which suggests the suppressed halide segregation. The XRD measurement also supports the suppressed halide segregation (**Figure 6.13**). The peak from the (100) plane shifted by participation of chlorines into the perovskite crystals. The peaks from the (110) and (200) plane looks like double peak by the halide segregation, but these peaks were originated from the TFA derived perovskite crystals on the surface[123] and normal halide perovskite inside the crystals. The peaks from the halide perovskites showed clear single peak, which also supports suppressed halide segregation. The TFA derived peaks in the XRD result implies the surface of the perovskite crystals is decorated by the TFA anions. The TFA anions might passivate the halide defects on the surface and reduced defect induced halide mobility and segregation.

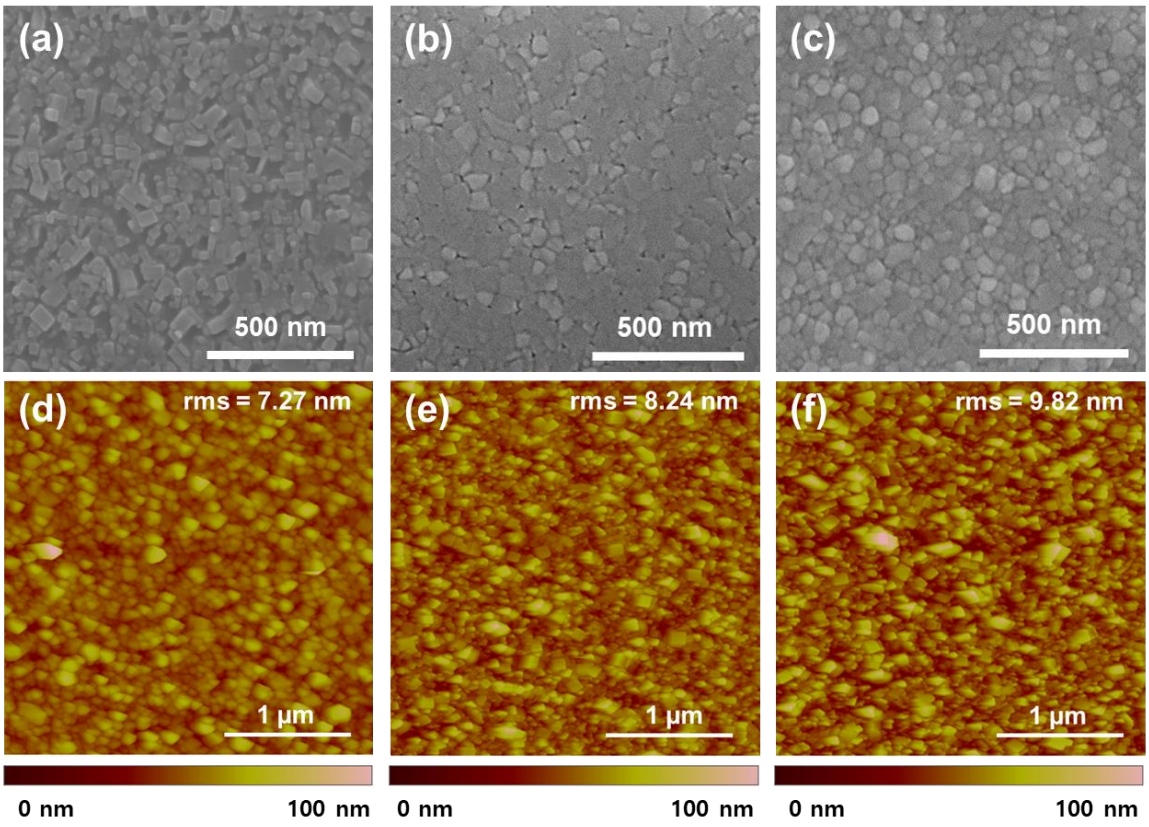

Figure 6.14. Scanning electron microscope (SEM) surface images of (a). reference (Rf. 520) and anion-exchanged bulk perovskite films, (b). A.E. 490 and (c). A.E. 470 conditions. Atomic force microscopy (AFM) surface images of (d). reference (Rf. 520) and anion-exchanged bulk perovskite films, (e). A.E. 490 and (f). A.E. 470 conditions.

To explore the change of the surface properties, surface analysis was conducted. The anion exchanged bulk perovskite films showed better morphology than the pristine $CsPbBr_3$ films. The surface images of pristine (**Figure 6.14a**) and anion exchanged bulk perovskite films (**Figure 6.14b** and **6.14c**) were obtained from the SEM measurements. The pristine $CsPbBr_3$ film showed low coverage and pinholes in the surface while anion exchanged films showed fully covered surface. Moreover, the grain size of the perovskites seemed not altered by the anion exchange. The result suggested that the anion exchange procedure is non-destructive method for not only for the perovskite nanocrystals, but also for the bulk perovskites. The AFM measurement was also conducted to support the surface result. The covered region of the surfaces was measured, and there was small difference in roughness between the pristine film and anion exchanged films (**Figure 6.14d-6.14f**). All films, regardless of anion exchange treatment, showed smooth surface with roughness of few nanometers. The cross-section SEM measurement (**Figure 6.15**) also conducted to check the change of the film thickness. Interestingly, seeing the cross-section image, the thickness of film was decreased more than the lattice parameter reduction after the anion exchange, which suggests partially dissolved crystals.

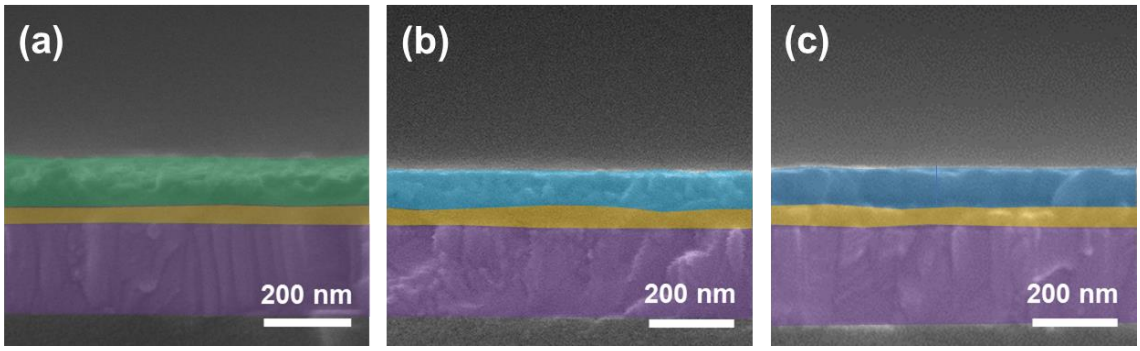

Figure 6.15. Surface analysis. Scanning electron microscope (SEM) cross-section images of A. reference (Rf. 520) and anion-exchanged bulk perovskite films, B. A.E. 490 and C. A.E. 470 conditions.

At first, we expected that the anion exchange treatment might not alter the perovskite film morphology because the method showed non-destructive result with the perovskite nanocrystals. However, the result showed there were morphological changes after the anion exchange treatment and there was additional reduction of thickness of the film. These results suggest that the anion exchange procedure partially dissolve the upper surface of the films and filled empty spaces of the films. This reconstructive effect on the perovskite crystals improved overall quality of the film. Our hypothesis for the surface reconstruction mechanism is that the ions in the pristine perovskite crystals were partially dissolved by the nucleophilic TBP, and then ions in the reaction solution spontaneously re-crystalized at the empty spaces on the substrate due to non-polar character of the reaction solution. Fortunately, the reconstruction effect assists the films to have better coverage and packing which is beneficial for device fabrication.

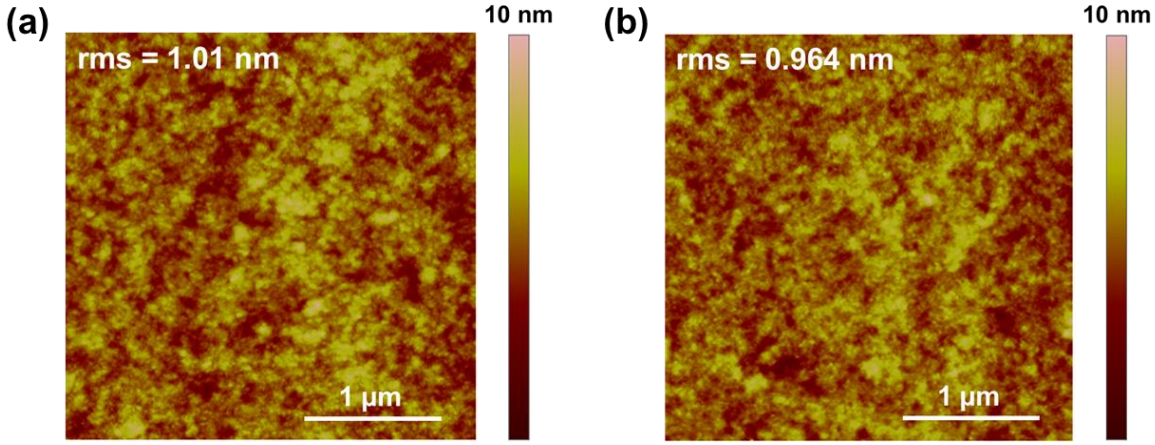

Figure 6.16. Atomic force microscopy (AFM) images of PEDOT:PSS layer (a). w/o and (b). w/ dipping into TBP mixed CF solution.

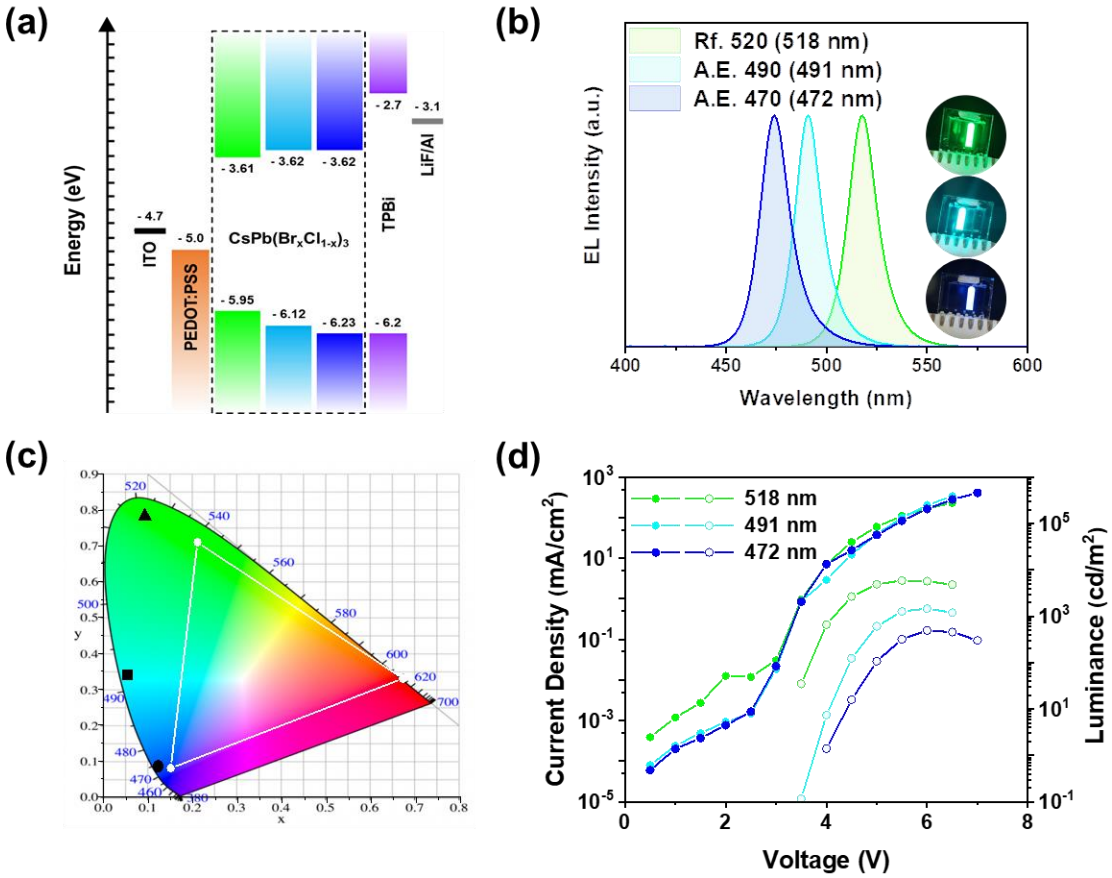

Figure 6.17. PeLEDs characteristics: (a). Band energy diagram of device, (b). electroluminescence spectra, (c). The CIE color space coordinates, (d). *J-V-L* plot of pristine and anion-exchanged bulk perovskite films.

With the fine control of the anion exchange treatment, the narrow blue emission was obtained with inorganic bulk perovskites. Before applying the anion exchanged perovskites to the devices, the effect of anion exchange treatment to the substrate was scanned. **Figure 6.16** is the AFM images of the PEDOT:PSS layer before and after anion exchange treatment. There was no significant change in film morphology and thickness of the layer, which suggests that the anion exchange method could widely be applied to various purposes. With the inorganic bulk blue emissive perovskite films, the PeLEDs were fabricated (**Figure 6.17**). The band diagram of the LED was shown in **Figure 6.17a**, the electronic energy levels were confirmed with the UPS measurement (**Figure 6.18** and **Table 6.2**). The electroluminescence (EL) spectra of the PeLEDs were shown in **Figure 6.17b**. As shown in the PL spectra, the PeLEDs exhibited targeted 470 and 490 nm emission peaks, with A.E. 470 condition and A.E. 490 condition. The EL spectra showed highly saturated colors with narrow FWHM of 19.06 nm and 17.86 nm for A.E. 470 and A.E. 490 condition, respectively. The color coordinates of the PeLEDs are marked in the CIE color space (**Figure 6.17c)** which satisfies the NTSC standard. Based on the

coordinates on the color space, the color purities of the devices were calculated. Considering the center position with the CIE standard illuminant D65, the color purity of PeLEDs with A.E. 470 was 97.29% and with A.E. 490 was 94.07%. The device characteristics are shown in **Figure 6.17d, Figure 6.19** and summarized in **Table 6.3**. The blue color PeLEDs achieved 1.18% and 0.32% of EQE and 1468 cd/m^2 and 495 cd/m^2 of maximum luminance for the A.E. 470 and A.E 490 condition, respectively. The uniformity of the PeLEDs was tested over whole device (**Figure 6.20**). As shown in **Figure 6.8**, The anion exchange treatment was evenly conducted over the film and the result showed very similar values and peak position. Operational spectral stability was also tested (**Figure 6.21**) to confirm the suppressed halide segregation. As shown in thermal stability result, the halide segregation was successfully suppressed and maintained original peak position, at the high level of current injection (~100 mA/cm^2).

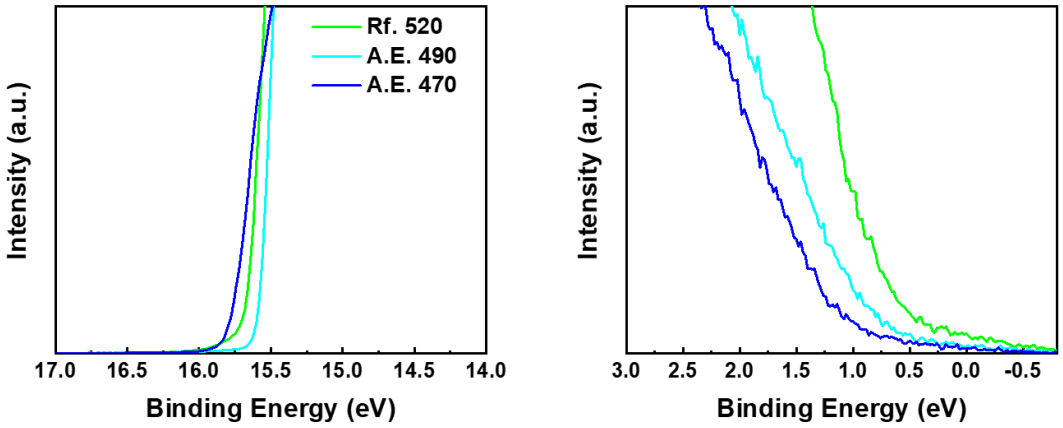

Figure 6.18. UPS spectra (left: secondary electron cutoff region, right: onset region) of reference (Rf. 520) and anion-exchanged bulk perovskite films via dipping method.

	E_g	E_{VB}	E_{CB}
Rf. 520	2.34	5.95	3.61
A.E. 490	2.50	6.12	3.62
A.E. 470	2.61	6.23	3.62

Table 6.2. Summarized energy level values for anion-exchanged bulk perovskite films measured from UPS and Tauc plot.

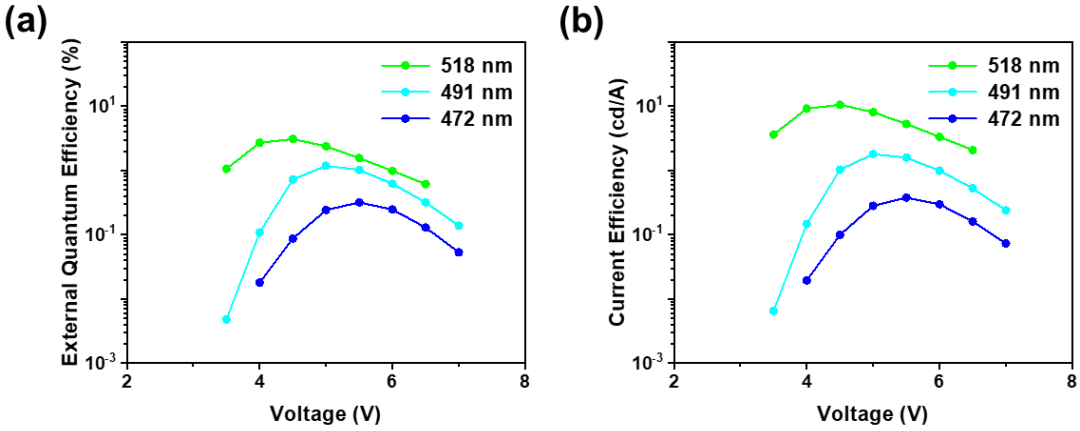

Figure 6.19. (a) external quantum efficiency, and (b). current efficiency of reference and anion-exchanged bulk perovskite films.

Condition	L_{max} [cd m^{-2}] @ bias	LE_{max} [cd A^{-1}] @ bias	EQE_{max} [%] @ bias	Turn-on voltage [V] @ 0.1 cd m^{-2}
Rf. 520	5901.9@5.5	10.57@4.5	3.10@4.5	3.0
A.E. 490	1467.8@6.0	1.80@5.0	1.18@5.0	3.5
A.E. 470	494.7@6.0	0.38@5.5	0.32@5.5	3.5

Table 6.3. Summarized device performances of optimized PeLEDs with reference and anion-exchanged bulk perovskite as emitting layer; Device structure: ITO/ PEDOT:PSS/ Perovskite/ TPBi/ LiF/ Al.

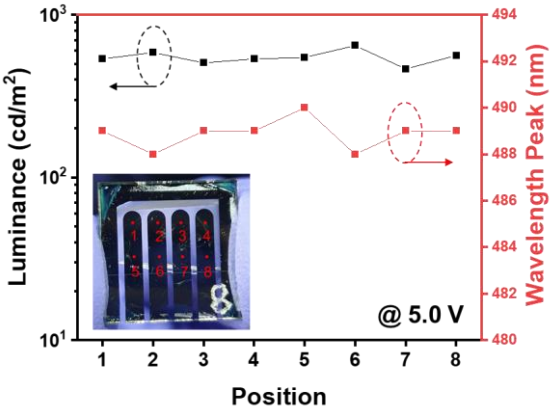

Figure 6.20. Performance uniformity of PeLEDs with anion-exchanged bulk perovskite films, A.E. 490 condition.

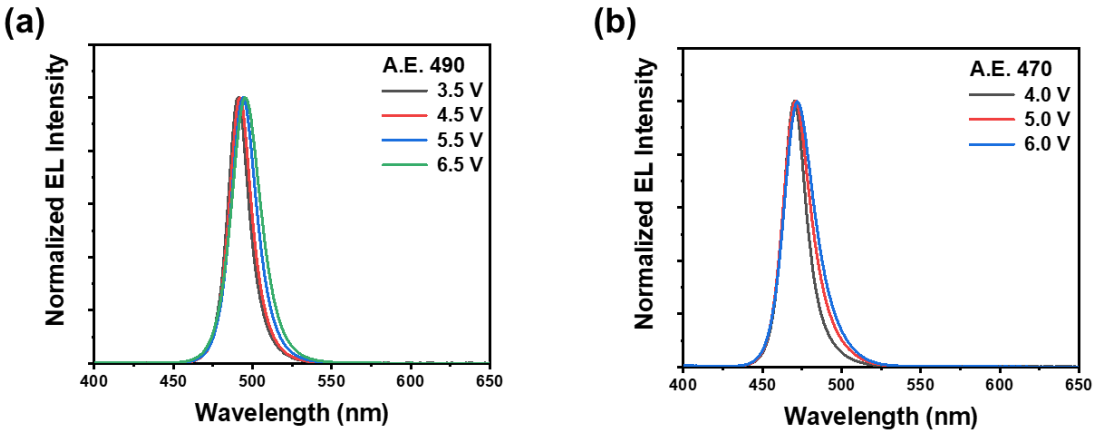

Figure 6.21. EL spectra of operated under different applied voltages of the optimized PeLEDs with anion-exchanged bulk perovskite films, (a). A.E. 490 and (b). A.E. 470 condition.

6.4 Conclusion

In summary, we developed bulk inorganic perovskite blue LEDs through the controlled anion exchange method. The anion exchange method could easily be controlled, and the targeted blue emission was achieved with adjustments. With the atomic analysis, the anion exchange for all over the bulk film were confirmed by XPS and TOF-SIMS measurements. The anion exchange treatment was conducted in the non-polar solvent system, so the bulk perovskite films were maintained original genuine properties. The beneficial reconstructive characteristics were confirmed with the surface and structural analysis. We successfully fabricated highly saturated PeLEDs and achieved 1468 cd/m^2 and 494 cd/m^2 of maximum luminance with 490 nm and 470 nm emission condition respectively, which is highest value in the inorganic bulk perovskite blue LEDs with successfully suppressed halide segregation.

CHAPTER 7. Summary

In this thesis, newly developed halide substitution methods for halide perovskites including nanocrystals and bulk states were discussed. The halide substituted halide perovskites successfully applied to the devices.

In chapter 3, through the halide containing ligand exchange method, the halides were substituted to PeNCs. The tridodecylmethyl ammonium iodide (TrDAI) ligands were used to synthesized indefective and structural sturdy $CsPbBr_xI_{3-x}$ NCs via LMPT method. Not only for the control the halide ratio in the PeNCs, but also for passivating the surface defects the TrDAI ligands were utilized. The surface defects are origin of chemical degradation and related structural distortion. With the halide ligand exchange strategy, the chemical and structural stability of PeNCs was enhanced through the passivation of the surface defect, resulting longer carrier lifetime and better optical properties. Additionally, through the ligand exchange, the capping density of the surface of the PeNCs were optimized and both effective charge injection and effective radiative recombination in EML was enabled. The PeLEDs achieved maximum CE of 7.69 cd/A and EQE of 6.36%.

In chapter 4, I introduced new halide exchange method for PeNCs through noble halide sources, halide containing solvents. The idea was from potentially unstable property of the halide containing solvents, proved by the reported optical or chemical reactions. Based on the knowledge of chemical detachment of the organohalide solvents, the new pathway for obtain halides was developed. The halide solvents and strong nucleophilic ligands were used for the reaction. The strong nucleophilic ligand triggered the reaction and lowered overall chemical energy barriers. The reaction mechanism was revealed to be similar with S_N2 reaction by the computational prediction and confirmed with detection of the biproducts. The reaction happens in all hydrophobic liquid system, which is favorable to the PeNCs, and revealed to be non-destructive to PeNCs. The understanding of the reaction mechanism enabled the fine control of the reaction speed and results of finely controlled halide ratio of PeNCs. Due to the simplicity of the reaction, the halide substitution was able to apply to common PeNCs ($CsPbCl_3$ $\rightleftharpoons$ $CsPbBr_3$ $\rightleftharpoons$ $CsPbI_3$) to get any desired halide ratio and related emission. The halide substituted PeNCs were successfully applied to the LEDs and obtained red, green, and blue EL spectra satisfying the NTSC standard. Because the reaction is free from the cations that have opportunity of participation in perovskite structure, the method is appropriate to get pure PeNCs.

In chapter 5, I suggested clues of narrow emission spectra of PeNCs. Though the systematic study on the PeNCs, the fact that emission spectra is dominantly affected by the mean size of PeNCs, was revealed. This result was beyond my expectation, because I firstly expected the size distribution of the PeNCs will have effect on the emission spectra with statistical reasons. With additional study, it was confirmed that size distribution has effect on the emission spectra, but the mean size amplifies the effect of size distribution on the emission spectra. The typical PeNCs synthesis method has nearly monodispersed size distribution, so the effect of the size distribution was neglected for now. Then, the post treatment surface passivation method for narrower emission spectra was developed. I modified the method introduced in chapter 4, changing the strong nucleophilic ligand. With treatment via ligands of shorter alkyl chain length, the emission width of PeNCs was narrowed, however, the optical efficiency was similarly enhanced. I interpreted this result came from the two factors. The similar enhanced optical property owes to the halide passivation effect of the surface passivation and the narrowed emission spectra is related to the ligand passivation of the surface passivation. The ligand defects, in other words A site defects, were neglected in previous results, because regardless of the density of the A site defects, the performance of the devices was enhanced even only with halide passivation. I obtained blue PeLEDs with very narrow emission spectra with surface passivation. Through the study, I suggested that the A site defect should also be considered for PeLEDs and the next generation displays.

In chapter 6, I applied the halide substitution method developed in chapter 4 to the solid bulk perovskite films. Because the method is totally hydrophobic, halide substitution on the bulk perovskite was possible, unlike other polar solvent containing methods. I fabricated inorganic bulk blue films which was hard with typical method due to the low solubility of inorganic Cl sources. As the mechanism of the reaction also applied to the bulk perovskites, the emission spectra of the film were finely controlled with adjustments of reaction conditions. The inorganic bulk blue perovskite films exhibited stable emission, with suppressed halide segregation effect. With deep study on the surface of the inorganic bulk halide perovskite film, I found that the method has additional beneficial effect of reconstruction of film. The empty space of the films was passivated after the halide substitution procedure and resulted better packing of the film. The PeLEDs with this inorganic bulk blue halide perovskite were fabricated and recorded highest efficiency among the inorganic bulk blue PeLEDs due to the enhanced optoelectrical properties and structural properties.

With the halide substitution method, I found that the great optoelectronic properties of halide perovskite could be enhanced more. The most of optical efficiencies are depends on the defect density of the halide perovskite, so it is critical to passivate those defects to improve the material property and device performances. Interestingly, the substitution of halide in the perovskite with excess supply of the

halide ultimately result in the halide passivation effect. Therefore, the understand of the halide substitution led to the understand of the halide passivation. Based on the understand, I successfully tuned the halides in the halide perovskites ant related optoelectronic bandgaps. I obtained optically efficient PeNCs with saturated colors in red, green, and blue colors and PeLEDs with these advanced PeNCs. These halide substitution methods will suggest the direction of the post treatment method for obtaining defect-free, optically efficient, and stable perovskite optoelectronic devices.

REFERENCES

1. Zissis, G., Energy Consumption and Environmental and Economic Impact of Lighting: The Current Situation. In *Handbook of Advanced Lighting Technology*, **2016**; pp 1-13.
2. Schubert, E. F., History of light-emitting diodes. In *Light-Emitting Diodes*, **2006**; pp 1-26.
3. Hall, R. N.; Fenner, G. E.; Kingsley, J. D.; Soltys, T. J.; Carlson, R. O., Coherent Light Emission From GaAs Junctions. *Phys. Rev. Lett.* **1962,** *9* (9), 366-368.
4. Logan, R. A.; White, H. G.; Wiegmann, W., Efficient green electroluminescent junctions in GaP. *Solid State Electron.* **1971,** *14* (1), 55-70.
5. Nuese, C. J.; Tietjen, J. J.; Gannon, J. J.; Gossenberger, H. F., Optimization of Electroluminescent Efficiencies for Vapor-Grown GaAs[sub 1−x]P[sub x] Diodes. *J. Electrochem. Soc.* **1969,** *116* (2), 248.
6. Nakamura, S.; Mukai, T.; Senoh, M., Candela-class high-brightness InGaN/AlGaN double-heterostructure blue-light-emitting diodes. *Appl. Phys. Lett.* **1994,** *64* (13), 1687-1689.
7. Tang, C. W.; VanSlyke, S. A., Organic electroluminescent diodes. *Appl. Phys. Lett.* **1987,** *51* (12), 913-915.
8. Colvin, V. L.; Schlamp, M. C.; Alivisatos, A. P., Light-emitting diodes made from cadmium selenide nanocrystals and a semiconducting polymer. *Nature*. **1994,** *370* (6488), 354-357.
9. Kim, T.; Kim, K.-H.; Kim, S.; Choi, S.-M.; Jang, H.; Seo, H.-K.; Lee, H.; Chung, D.-Y.; Jang, E., Efficient and stable blue quantum dot light-emitting diode. *Nature*. **2020,** *586* (7829), 385-389.
10. Lin, K.; Xing, J.; Quan, L. N.; de Arquer, F. P. G.; Gong, X.; Lu, J.; Xie, L.; Zhao, W.; Zhang, D.; Yan, C.; Li, W.; Liu, X.; Lu, Y.; Kirman, J.; Sargent, E. H.; Xiong, Q.; Wei, Z., Perovskite light-emitting diodes with external quantum efficiency exceeding 20 per cent. *Nature*. **2018,** *562* (7726), 245-248.
11. Zhao, B.; Bai, S.; Kim, V.; Lamboll, R.; Shivanna, R.; Auras, F.; Richter, J. M.; Yang, L.; Dai, L.; Alsari, M.; She, X.-J.; Liang, L.; Zhang, J.; Lilliu, S.; Gao, P.; Snaith, H. J.; Wang, J.; Greenham, N. C.; Friend, R. H.; Di, D., High-efficiency perovskite–polymer bulk heterostructure light-emitting diodes. *Nat. Photonics*. **2018,** *12* (12), 783-789.
12. Chiba, T.; Hayashi, Y.; Ebe, H.; Hoshi, K.; Sato, J.; Sato, S.; Pu, Y.-J.; Ohisa, S.; Kido, J., Anion-exchange red perovskite quantum dots with ammonium iodine salts for highly efficient light-emitting devices. *Nat. Photonics*. **2018,** *12* (11), 681-687.
13. Shamsi, J.; Urban, A. S.; Imran, M.; De Trizio, L.; Manna, L., Metal Halide Perovskite Nanocrystals: Synthesis, Post-Synthesis Modifications, and Their Optical Properties. *Chem. Rev.* **2019,** *119* (5), 3296-3348.
14. Wells, H. L., Über die Cäsium- und Kalium-Bleihalogenide. *Z. Anorg. Allg. Chem.* **1893,** *3* (1), 195-210.
15. Jeong, M.; Choi, I. W.; Go, E. M.; Cho, Y.; Kim, M.; Lee, B.; Jeong, S.; Jo, Y.; Choi, H. W.; Lee, J.; Bae, J.-H.; Kwak, S. K.; Kim, D. S.; Yang, C., Stable perovskite solar cells with efficiency exceeding 24.8% and 0.3-V voltage loss. *Science*. **2020,** *369* (6511), 1615.
16. Manser, J. S.; Christians, J. A.; Kamat, P. V., Intriguing Optoelectronic Properties of Metal Halide Perovskites. *Chem. Rev.* **2016,** *116* (21), 12956-13008.
17. Uribe, J. I.; Ramirez, D.; Osorio-Guillén, J. M.; Osorio, J.; Jaramillo, F., CH3NH3CaI3 Perovskite: Synthesis, Characterization, and First-Principles Studies. *J. Phys. Chem. C*. **2016,** *120* (30), 16393-16398.
18. Yin, W.-J.; Shi, T.; Yan, Y., Unusual defect physics in CH3NH3PbI3 perovskite solar cell absorber. *Appl. Phys. Lett.* **2014,** *104* (6), 063903.
19. Takagahara, T.; Takeda, K., Theory of the quantum confinement effect on excitons in quantum dots of indirect-gap materials. *Phys. Rev. B*. **1992,** *46* (23), 15578-15581.
20. Protesescu, L.; Yakunin, S.; Bodnarchuk, M. I.; Krieg, F.; Caputo, R.; Hendon, C. H.; Yang,

R. X.; Walsh, A.; Kovalenko, M. V., Nanocrystals of Cesium Lead Halide Perovskites (CsPbX3, X = Cl, Br, and I): Novel Optoelectronic Materials Showing Bright Emission with Wide Color Gamut. *Nano Letters*. **2015,** *15* (6), 3692-3696.
21. Gil-Escrig, L.; Longo, G.; Pertegás, A.; Roldán-Carmona, C.; Soriano, A.; Sessolo, M.; Bolink, H. J., Efficient photovoltaic and electroluminescent perovskite devices. *Chem. Commun.* **2015,** *51* (3), 569-571.
22. Kim, Y.-H.; Cho, H.; Lee, T.-W., Metal halide perovskite light emitters. *Proc. Natl. Acad. Sci.* **2016,** *113* (42), 11694.
23. Yang, W. S.; Noh, J. H.; Jeon, N. J.; Kim, Y. C.; Ryu, S.; Seo, J.; Seok, S. I., High-performance photovoltaic perovskite layers fabricated through intramolecular exchange. *Science*. **2015,** *348* (6240), 1234.
24. Zheng, X.; Hou, Y.; Bao, C.; Yin, J.; Yuan, F.; Huang, Z.; Song, K.; Liu, J.; Troughton, J.; Gasparini, N.; Zhou, C.; Lin, Y.; Xue, D.-J.; Chen, B.; Johnston, A. K.; Wei, N.; Hedhili, M. N.; Wei, M.; Alsalloum, A. Y.; Maity, P.; Turedi, B.; Yang, C.; Baran, D.; Anthopoulos, T. D.; Han, Y.; Lu, Z.-H.; Mohammed, O. F.; Gao, F.; Sargent, E. H.; Bakr, O. M., Managing grains and interfaces via ligand anchoring enables 22.3%-efficiency inverted perovskite solar cells. *Nat. Energy.* **2020,** *5* (2), 131-140.
25. Xing, G.; Mathews, N.; Lim, S. S.; Yantara, N.; Liu, X.; Sabba, D.; Grätzel, M.; Mhaisalkar, S.; Sum, T. C., Low-temperature solution-processed wavelength-tunable perovskites for lasing. *Nat. Mater.* **2014,** *13* (5), 476-480.
26. Liu, Y.; Cui, J.; Du, K.; Tian, H.; He, Z.; Zhou, Q.; Yang, Z.; Deng, Y.; Chen, D.; Zuo, X.; Ren, Y.; Wang, L.; Zhu, H.; Zhao, B.; Di, D.; Wang, J.; Friend, R. H.; Jin, Y., Efficient blue light-emitting diodes based on quantum-confined bromide perovskite nanostructures. *Nat. Photonics*. **2019,** *13* (11), 760-764.
27. Park, M.-H.; Park, J.; Lee, J.; So, H. S.; Kim, H.; Jeong, S.-H.; Han, T.-H.; Wolf, C.; Lee, H.; Yoo, S.; Lee, T.-W., Efficient Perovskite Light-Emitting Diodes Using Polycrystalline Core–Shell-Mimicked Nanograins. *Adv. Funct. Mater.* **2019,** *29* (22), 1902017.
28. Song, J.; Fang, T.; Li, J.; Xu, L.; Zhang, F.; Han, B.; Shan, Q.; Zeng, H., Organic–Inorganic Hybrid Passivation Enables Perovskite QLEDs with an EQE of 16.48%. *Adv. Mater.* **2018,** *30* (50), 1805409.
29. Cao, Y.; Wang, N.; Tian, H.; Guo, J.; Wei, Y.; Chen, H.; Miao, Y.; Zou, W.; Pan, K.; He, Y.; Cao, H.; Ke, Y.; Xu, M.; Wang, Y.; Yang, M.; Du, K.; Fu, Z.; Kong, D.; Dai, D.; Jin, Y.; Li, G.; Li, H.; Peng, Q.; Wang, J.; Huang, W., Perovskite light-emitting diodes based on spontaneously formed submicrometre-scale structures. *Nature*. **2018,** *562* (7726), 249-253.
30. Kim, H.-B.; Yoon, Y. J.; Jeong, J.; Heo, J.; Jang, H.; Seo, J. H.; Walker, B.; Kim, J. Y., Peroptronic devices: perovskite-based light-emitting solar cells. *Energy Environ. Sci.* **2017,** *10* (9), 1950-1957.
31. Min, H.; Kim, M.; Lee, S.-U.; Kim, H.; Kim, G.; Choi, K.; Lee, J. H.; Seok, S. I., Efficient, stable solar cells by using inherent bandgap of α-phase formamidinium lead iodide. *Science*. **2019,** *366* (6466), 749.
32. Kulbak, M.; Gupta, S.; Kedem, N.; Levine, I.; Bendikov, T.; Hodes, G.; Cahen, D., Cesium Enhances Long-Term Stability of Lead Bromide Perovskite-Based Solar Cells. *J. Phys. Chem. Lett.* **2016,** *7* (1), 167-172.
33. Cho, H.; Kim, Y.-H.; Wolf, C.; Lee, H.-D.; Lee, T.-W., Improving the Stability of Metal Halide Perovskite Materials and Light-Emitting Diodes. *Adv. Mater.* **2018,** *30* (42), 1704587.
34. Zou, S.; Liu, Y.; Li, J.; Liu, C.; Feng, R.; Jiang, F.; Li, Y.; Song, J.; Zeng, H.; Hong, M.; Chen, X., Stabilizing Cesium Lead Halide Perovskite Lattice through Mn(II) Substitution for Air-Stable Light-Emitting Diodes. *J. Am. Chem.* **2017,** *139* (33), 11443-11450.
35. Yassitepe, E.; Yang, Z.; Voznyy, O.; Kim, Y.; Walters, G.; Castañeda, J. A.; Kanjanaboos, P.; Yuan, M.; Gong, X.; Fan, F.; Pan, J.; Hoogland, S.; Comin, R.; Bakr, O. M.; Padilha, L. A.; Nogueira, A. F.; Sargent, E. H., Amine-Free Synthesis of Cesium Lead Halide Perovskite Quantum Dots for Efficient Light-Emitting Diodes. *Adv. Funct. Mater.* **2016,** *26* (47), 8757-8763.

36. De Roo, J.; Ibáñez, M.; Geiregat, P.; Nedelcu, G.; Walravens, W.; Maes, J.; Martins, J. C.; Van Driessche, I.; Kovalenko, M. V.; Hens, Z., Highly Dynamic Ligand Binding and Light Absorption Coefficient of Cesium Lead Bromide Perovskite Nanocrystals. *ACS Nano*. **2016,** *10* (2), 2071-2081.
37. Wu, H.; Zhang, Y.; Lu, M.; Zhang, X.; Sun, C.; Zhang, T.; Colvin, V. L.; Yu, W. W., Surface ligand modification of cesium lead bromide nanocrystals for improved light-emitting performance. *Nanoscale*. **2018,** *10* (9), 4173-4178.
38. Ma, J.-P.; Yin, J.; Chen, Y.-M.; Zhao, Q.; Zhou, Y.; Li, H.; Kuroiwa, Y.; Moriyoshi, C.; Li, Z.-Y.; Bakr, O. M.; Mohammed, O. F.; Sun, H.-T., Defect-Triggered Phase Transition in Cesium Lead Halide Perovskite Nanocrystals. *ACS Materials Lett.* **2019,** *1* (1), 185-191.
39. Seth, S.; Ahmed, T.; De, A.; Samanta, A., Tackling the Defects, Stability, and Photoluminescence of CsPbX3 Perovskite Nanocrystals. *ACS Energy Lett.* **2019,** *4* (7), 1610-1618.
40. Hieulle, J.; Wang, X.; Stecker, C.; Son, D.-Y.; Qiu, L.; Ohmann, R.; Ono, L. K.; Mugarza, A.; Yan, Y.; Qi, Y., Unraveling the Impact of Halide Mixing on Perovskite Stability. *J. Am. Chem.* **2019,** *141* (8), 3515-3523.
41. Swarnkar, A.; Marshall, A. R.; Sanehira, E. M.; Chernomordik, B. D.; Moore, D. T.; Christians, J. A.; Chakrabarti, T.; Luther, J. M., Quantum dot–induced phase stabilization of α-CsPbI₃ perovskite for high-efficiency photovoltaics. *Science*. **2016,** *354* (6308), 92-95.
42. Zhang, J.; Zhang, L.; Cai, P.; Xue, X.; Wang, M.; Zhang, J.; Tu, G., Enhancing stability of red perovskite nanocrystals through copper substitution for efficient light-emitting diodes. *Nano Energy*. **2019,** *62*, 434-441.
43. Pan, J.; Quan, L. N.; Zhao, Y.; Peng, W.; Murali, B.; Sarmah, S. P.; Yuan, M.; Sinatra, L.; Alyami, N. M.; Liu, J.; Yassitepe, E.; Yang, Z.; Voznyy, O.; Comin, R.; Hedhili, M. N.; Mohammed, O. F.; Lu, Z. H.; Kim, D. H.; Sargent, E. H.; Bakr, O. M., Highly Efficient Perovskite-Quantum-Dot Light-Emitting Diodes by Surface Engineering. *Advanced Materials*. **2016,** *28* (39), 8718-8725.
44. Kang, B.-H.; Lee, J.-S.; Lee, S.-W.; Kim, S.-W.; Lee, J.-W.; Gopalan, S.-A.; Park, J.-S.; Kwon, D.-H.; Bae, J.-H.; Kim, H.-R.; Kang, S.-W., Efficient exciton generation in atomic passivated CdSe/ZnS quantum dots light-emitting devices. *Sci. Rep.* **2016,** *6* (1), 34659.
45. Owen, J. S.; Park, J.; Trudeau, P.-E.; Alivisatos, A. P., Reaction Chemistry and Ligand Exchange at Cadmium−Selenide Nanocrystal Surfaces. *J. Am. Chem.* **2008,** *130* (37), 12279-12281.
46. Anderson, N. C.; Owen, J. S., Soluble, Chloride-Terminated CdSe Nanocrystals: Ligand Exchange Monitored by 1H and 31P NMR Spectroscopy. *Chem. Mater.* **2013,** *25* (1), 69-76.
47. 120Shin, Y. S.; Yoon, Y. J.; Lee, K. T.; Jeong, J.; Park, S. Y.; Kim, G.-H.; Kim, J. Y., Vivid and Fully Saturated Blue Light-Emitting Diodes Based on Ligand-Modified Halide Perovskite Nanocrystals. *ACS Appl. Mater. Interfaces*. **2019,** *11* (26), 23401-23409.
48. Fang, F.; Chen, W.; Li, Y.; Liu, H.; Mei, M.; Zhang, R.; Hao, J.; Mikita, M.; Cao, W.; Pan, R.; Wang, K.; Sun, X. W., Employing Polar Solvent Controlled Ionization in Precursors for Synthesis of High-Quality Inorganic Perovskite Nanocrystals at Room Temperature. *Adv. Funct. Mater.* **2018,** *28* (10), 1706000.
49. Wang, H.; Luo, C.; Tian, P.; Li, D.; Jiang, C.; Zhong, C.; Chen, S.; Huang, R.; Lin, H.; Peng, H., Formation and dispersion of organometal halide perovskite nanocrystals in various solvents. *J. Colloid Interface Sci.* **2018,** *529*, 575-581.
50. Kim, Y.; Yassitepe, E.; Voznyy, O.; Comin, R.; Walters, G.; Gong, X.; Kanjanaboos, P.; Nogueira, A. F.; Sargent, E. H., Efficient Luminescence from Perovskite Quantum Dot Solids. *ACS Appl. Mater. Interfaces*. **2015,** *7* (45), 25007-25013.
51. Bronstein, L. M.; Huang, X.; Retrum, J.; Schmucker, A.; Pink, M.; Stein, B. D.; Dragnea, B., Influence of Iron Oleate Complex Structure on Iron Oxide Nanoparticle Formation. *Chem. Mater.* **2007,** *19* (15), 3624-3632.
52. Bixner, O.; Lassenberger, A.; Baurecht, D.; Reimhult, E., Complete Exchange of the Hydrophobic Dispersant Shell on Monodisperse Superparamagnetic Iron Oxide Nanoparticles. *Langmuir*. **2015,** *31* (33), 9198-9204.
53. Huang, H. Y.; Yang, R. T.; Chinn, D.; Munson, C. L., Amine-Grafted MCM-48 and Silica

Xerogel as Superior Sorbents for Acidic Gas Removal from Natural Gas. *Industrial & Engineering Chemistry Research*. **2003,** *42* (12), 2427-2433.
54. Bakshi, M. S.; Sachar, S.; Kaur, G.; Bhandari, P.; Kaur, G.; Biesinger, M. C.; Possmayer, F.; Petersen, N. O., Dependence of Crystal Growth of Gold Nanoparticles on the Capping Behavior of Surfactant at Ambient Conditions. *Cryst. Growth Des.* **2008,** *8* (5), 1713-1719.
55. Yoon, Y. J.; Lee, K. T.; Lee, T. K.; Kim, S. H.; Shin, Y. S.; Walker, B.; Park, S. Y.; Heo, J.; Lee, J.; Kwak, S. K.; Kim, G.-H.; Kim, J. Y., Reversible, Full-Color Luminescence by Post-treatment of Perovskite Nanocrystals. *Joule*. **2018,** *2* (10), 2105-2116.
56. Lehmann, F.; Franz, A.; Többens, Daniel M.; Levcenco, S.; Unold, T.; Taubert, A.; Schorr, S., The phase diagram of a mixed halide (Br, I) hybrid perovskite obtained by synchrotron X-ray diffraction. *RSC Adv.* **2019,** *9* (20), 11151-11159.
57. Zhou, Y.; Zhao, Y., Chemical stability and instability of inorganic halide perovskites. *Energy Environ. Sci.* **2019,** *12* (5), 1495-1511.
58. Jing, Q.; Zhang, M.; Huang, X.; Ren, X.; Wang, P.; Lu, Z., Surface passivation of mixed-halide perovskite CsPb(BrxI1−x)3 nanocrystals by selective etching for improved stability. *Nanoscale*. **2017,** *9* (22), 7391-7396.
59. Yang, W. S.; Park, B.-W.; Jung, E. H.; Jeon, N. J.; Kim, Y. C.; Lee, D. U.; Shin, S. S.; Seo, J.; Kim, E. K.; Noh, J. H.; Seok, S. I., Iodide management in formamidinium-lead-halide–based perovskite layers for efficient solar cells. *Science*. **2017,** *356* (6345), 1376-1379.
60. Cho, H.; Jeong, S.-H.; Park, M.-H.; Kim, Y.-H.; Wolf, C.; Lee, C.-L.; Heo, J. H.; Sadhanala, A.; Myoung, N.; Yoo, S.; Im, S. H.; Friend, R. H.; Lee, T.-W., Overcoming the electroluminescence efficiency limitations of perovskite light-emitting diodes. *Science*. **2015,** *350* (6265), 1222.
61. Wang, N.; Cheng, L.; Ge, R.; Zhang, S.; Miao, Y.; Zou, W.; Yi, C.; Sun, Y.; Cao, Y.; Yang, R.; Wei, Y.; Guo, Q.; Ke, Y.; Yu, M.; Jin, Y.; Liu, Y.; Ding, Q.; Di, D.; Yang, L.; Xing, G.; Tian, H.; Jin, C.; Gao, F.; Friend, R. H.; Wang, J.; Huang, W., Perovskite light-emitting diodes based on solution-processed self-organized multiple quantum wells. *Nat. Photonics*. **2016,** *10* (11), 699-704.
62. Xing, J.; Yan, F.; Zhao, Y.; Chen, S.; Yu, H.; Zhang, Q.; Zeng, R.; Demir, H. V.; Sun, X.; Huan, A.; Xiong, Q., High-Efficiency Light-Emitting Diodes of Organometal Halide Perovskite Amorphous Nanoparticles. *ACS Nano*. **2016,** *10* (7), 6623-30.
63. Deng, W.; Xu, X.; Zhang, X.; Zhang, Y.; Jin, X.; Wang, L.; Lee, S.-T.; Jie, J., Organometal Halide Perovskite Quantum Dot Light-Emitting Diodes. *Adv. Funct. Mater.* **2016,** *26* (26), 4797-4802.
64. Meyns, M.; Peralvarez, M.; Heuer-Jungemann, A.; Hertog, W.; Ibanez, M.; Nafria, R.; Genc, A.; Arbiol, J.; Kovalenko, M. V.; Carreras, J.; Cabot, A.; Kanaras, A. G., Polymer-Enhanced Stability of Inorganic Perovskite Nanocrystals and Their Application in Color Conversion LEDs. *ACS Appl Mater Interfaces*. **2016,** *8* (30), 19579-86.
65. Zhang, X.; Xu, B.; Zhang, J.; Gao, Y.; Zheng, Y.; Wang, K.; Sun, X. W., All-Inorganic Perovskite Nanocrystals for High-Efficiency Light Emitting Diodes: Dual-Phase CsPbBr3-CsPb2Br5 Composites. *Adv. Funct. Mater.* **2016,** *26* (25), 4595-4600.
66. Li, G.; Rivarola, F. W.; Davis, N. J.; Bai, S.; Jellicoe, T. C.; de la Pena, F.; Hou, S.; Ducati, C.; Gao, F.; Friend, R. H.; Greenham, N. C.; Tan, Z. K., Highly Efficient Perovskite Nanocrystal Light-Emitting Diodes Enabled by a Universal Crosslinking Method. *Adv Mater*. **2016,** *28* (18), 3528-34.
67. Zhang, X.; Lin, H.; Huang, H.; Reckmeier, C.; Zhang, Y.; Choy, W. C.; Rogach, A. L., Enhancing the Brightness of Cesium Lead Halide Perovskite Nanocrystal Based Green Light-Emitting Devices through the Interface Engineering with Perfluorinated Ionomer. *Nano Lett.* **2016,** *16* (2), 1415-20.
68. Huang, H.; Chen, B.; Wang, Z.; Hung, T. F.; Susha, A. S.; Zhong, H.; Rogach, A. L., Water resistant CsPbX3 nanocrystals coated with polyhedral oligomeric silsesquioxane and their use as solid state luminophores in all-perovskite white light-emitting devices. *Chem. Sci.* **2016,** *7* (9), 5699-5703.
69. Song, J.; Li, J.; Li, X.; Xu, L.; Dong, Y.; Zeng, H., Quantum Dot Light-Emitting Diodes Based

on Inorganic Perovskite Cesium Lead Halides (CsPbX3). *Adv. Mater.* **2015,** *27* (44), 7162-7.
70. Solis-Ibarra, D.; Smith, I. C.; Karunadasa, H. I., Post-synthetic halide conversion and selective halogen capture in hybrid perovskites. *Chem. Sci.* **2015,** *6* (7), 4054-4059.
71. Li, G.; Ho, J. Y.-L.; Wong, M.; Kwok, H. S., Reversible Anion Exchange Reaction in Solid Halide Perovskites and Its Implication in Photovoltaics. *J. Phys. Chem. C*. **2015,** *119* (48), 26883-26888.
72. Chen, K.; Deng, X.; Goddard, R.; Tüysüz, H., Pseudomorphic Transformation of Organometal Halide Perovskite Using the Gaseous Hydrogen Halide Reaction. *Chem. Mater.* **2016,** *28* (15), 5530-5537.
73. Nedelcu, G.; Protesescu, L.; Yakunin, S.; Bodnarchuk, M. I.; Grotevent, M. J.; Kovalenko, M. V., Fast Anion-Exchange in Highly Luminescent Nanocrystals of Cesium Lead Halide Perovskites (CsPbX3, X = Cl, Br, I). *Nano Lett.* **2015,** *15* (8), 5635-40.
74. Parobek, D.; Dong, Y.; Qiao, T.; Rossi, D.; Son, D. H., Photoinduced Anion Exchange in Cesium Lead Halide Perovskite Nanocrystals. *J. Am. Chem. Soc.* **2017,** *139* (12), 4358-4361.
75. DePuy, C. H.; Gronert, S.; Mullin, A.; Bierbaum, V. M., Gas-Phase SN2 and E2 Reactions of Alkyl Halides. *J. Am. Chem. Soc.* **1990,** *112*, 8650-8655.
76. Hines, M. A.; Guyot-Sionnest, P., Bright UV-Blue Luminescent Colloidal ZnSe Nanocrystals. *J. Phys. Chem. B*. **1998,** *102*, 3655-3657.
77. Peng, X.; Manna, L.; Yang, W.; Wickham, J.; Scher, E.; Kadavanich, A.; Alivisatos, A. P., Shape control of CdSe nanocrystals. *Nature*. **1999,** *404*, 59-61.
78. Delley, B., An all-electron numerical method for solving the local density functional for polyatomic molecules. *J. Chem. Phys.* **1990,** *92* (1), 508-517.
79. Delley, B., From molecules to solids with the DMol3 approach. *J. Chem. Phys.* **2000,** *113* (18), 7756-7764.
80. Perdew, J. P.; Burke, K.; Ernzerhof, M., Generalized Gradient Approximation Made Simple. *Phys. Rev. Lett.* **1996,** *77* (18), 3865-3868.
81. Tkatchenko, A.; Scheffler, M., Accurate Molecular Van Der Waals Interactions from Ground-State Electron Density and Free-Atom Reference Data. *Phys. Rev. Lett.* **2009,** *102* (7), 073005.
82. Klamt, A.; Schüürmann, G., COSMO: a new approach to dielectric screening in solvents with explicit expressions for the screening energy and its gradient. *J. Chem. Soc., Perkin Trans.* **1993,** (5), 799-805.
83. Bruno, T. J., Svoronos, P. D. N., *CRC Handbook of Fundamental Spectroscopic Correlation Charts.* CRC Press: Taylor & Francis Group: Boca Raton, FL: **2005**.
84. West, R. C., Astle, M. J., Beyer, W. H., *CRC Handbook of Chemistry and Physics*. 66 ed.; CRC Press: **1985**.
85. Haynes, W. M., *CRC Handbook of Chemistry and Physics*. 96 ed.; CRC Press: Boca Raton, FL: **2016**.
86. Looyenga, H., Dielectric constants of heterogeneous mixtures. *Physica*. **1965,** *31* (3), 401-406.
87. Govind, N.; Petersen, M.; Fitzgerald, G.; King-Smith, D.; Andzelm, J., A generalized synchronous transit method for transition state location. *Comput. Mater. Sci.* **2003,** *28* (2), 250-258.
88. Halgren, T. A.; Lipscomb, W. N., The synchronous-transit method for determining reaction pathways and locating molecular transition states. *Chem. Phys. Lett.* **1977,** *49* (2), 225-232.
89. Akkerman, Q. A.; D'Innocenzo, V.; Accornero, S.; Scarpellini, A.; Petrozza, A.; Prato, M.; Manna, L., Tuning the Optical Properties of Cesium Lead Halide Perovskite Nanocrystals by Anion Exchange Reactions. *J. Am. Chem. Soc.* **2015,** *137* (32), 10276-81.
90. Wittig., G.; Schöllkopf., U., Über Triphenyl-phosphin-methylene als olefinbildende Reagenzien I. *Ber. Dtsch. Chem. Ges.* **1954,** *87* (9), 1318.
91. Koscher, B. A.; Bronstein, N. D.; Olshansky, J. H.; Bekenstein, Y.; Alivisatos, A. P., Surface- vs Diffusion-Limited Mechanisms of Anion Exchange in CsPbBr3 Nanocrystal Cubes Revealed through Kinetic Studies. *J. Am. Chem. Soc.* **2016,** *138* (37), 12065-8.
92. Kim, M.; Kim, G.-H.; Lee, T. K.; Choi, I. W.; Choi, H. W.; Jo, Y.; Yoon, Y. J.; Kim, J. W.; Lee, J.; Huh, D.; Lee, H.; Kwak, S. K.; Kim, J. Y.; Kim, D. S., Methylammonium Chloride Induces Intermediate Phase Stabilization for Efficient Perovskite Solar Cells. *Joule*. **2019,** *3* (9), 2179-

2192.
93. Wang, Q.; Wang, X.; Yang, Z.; Zhou, N.; Deng, Y.; Zhao, J.; Xiao, X.; Rudd, P.; Moran, A.; Yan, Y.; Huang, J., Efficient sky-blue perovskite light-emitting diodes via photoluminescence enhancement. *Nat. Commun.* **2019,** *10* (1), 5633.
94. Tian, Y.; Zhou, C.; Worku, M.; Wang, X.; Ling, Y.; Gao, H.; Zhou, Y.; Miao, Y.; Guan, J.; Ma, B., Highly Efficient Spectrally Stable Red Perovskite Light-Emitting Diodes. *Adv. Mater.* **2018,** *30* (20), 1707093.
95. Hou, S.; Gangishetty, M. K.; Quan, Q.; Congreve, D. N., Efficient Blue and White Perovskite Light-Emitting Diodes via Manganese Doping. *Joule*. **2018,** *2* (11), 2421-2433.
96. Gangishetty, M. K.; Sanders, S. N.; Congreve, D. N., Mn2+ Doping Enhances the Brightness, Efficiency, and Stability of Bulk Perovskite Light-Emitting Diodes. *ACS Photonics*. **2019,** *6* (5), 1111-1117.
97. Gangishetty, M. K.; Hou, S.; Quan, Q.; Congreve, D. N., Reducing Architecture Limitations for Efficient Blue Perovskite Light-Emitting Diodes. *Adv. Mater.* **2018,** *30* (20), 1706226.
98. Creutz, S. E.; Crites, E. N.; De Siena, M. C.; Gamelin, D. R., Anion Exchange in Cesium Lead Halide Perovskite Nanocrystals and Thin Films Using Trimethylsilyl Halide Reagents. *Chem. Mater.* **2018,** *30* (15), 4887-4891.
99. Gong, X.; Voznyy, O.; Jain, A.; Liu, W.; Sabatini, R.; Piontkowski, Z.; Walters, G.; Bappi, G.; Nokhrin, S.; Bushuyev, O.; Yuan, M.; Comin, R.; McCamant, D.; Kelley, S. O.; Sargent, E. H., Electron–phonon interaction in efficient perovskite blue emitters. *Nat. Mater.* **2018,** *17* (6), 550-556.
100. Huang, H.; Bodnarchuk, M. I.; Kershaw, S. V.; Kovalenko, M. V.; Rogach, A. L., Lead Halide Perovskite Nanocrystals in the Research Spotlight: Stability and Defect Tolerance. *ACS Energy Lett.* **2017,** *2* (9), 2071-2083.
101. ten Brinck, S.; Infante, I., Surface Termination, Morphology, and Bright Photoluminescence of Cesium Lead Halide Perovskite Nanocrystals. *ACS Energy Lett.* **2016,** *1* (6), 1266-1272.
102. Zu, Y.; Xi, J.; Li, L.; Dai, J.; Wang, S.; Yun, F.; Jiao, B.; Dong, H.; Hou, X.; Wu, Z., High-Brightness and Color-Tunable FAPbBr3 Perovskite Nanocrystals 2.0 Enable Ultrapure Green Luminescence for Achieving Recommendation 2020 Displays. *ACS Appl. Mater. Interfaces*. **2020,** *12* (2), 2835-2841.
103. Wu, Y.; Wei, C.; Li, X.; Li, Y.; Qiu, S.; Shen, W.; Cai, B.; Sun, Z.; Yang, D.; Deng, Z.; Zeng, H., In Situ Passivation of PbBr64– Octahedra toward Blue Luminescent CsPbBr3 Nanoplatelets with Near 100% Absolute Quantum Yield. *ACS Energy Lett.* **2018,** *3* (9), 2030-2037.
104. Zheng, C.; Bi, C.; Huang, F.; Binks, D.; Tian, J., Stable and Strong Emission CsPbBr3 Quantum Dots by Surface Engineering for High-Performance Optoelectronic Films. *ACS Appl. Mater. Interfaces*. **2019,** *11* (28), 25410-25416.
105. Ochsenbein, S. T.; Krieg, F.; Shynkarenko, Y.; Rainò, G.; Kovalenko, M. V., Engineering Color-Stable Blue Light-Emitting Diodes with Lead Halide Perovskite Nanocrystals. *ACS Appl. Mater. Interfaces*. **2019,** *11* (24), 21655-21660.
106. Bekenstein, Y.; Koscher, B. A.; Eaton, S. W.; Yang, P.; Alivisatos, A. P., Highly Luminescent Colloidal Nanoplates of Perovskite Cesium Lead Halide and Their Oriented Assemblies. *J. Am. Chem.* **2015,** *137* (51), 16008-16011.
107. Butkus, J.; Vashishtha, P.; Chen, K.; Gallaher, J. K.; Prasad, S. K. K.; Metin, D. Z.; Laufersky, G.; Gaston, N.; Halpert, J. E.; Hodgkiss, J. M., The Evolution of Quantum Confinement in CsPbBr3 Perovskite Nanocrystals. *Chem. Mater.* **2017,** *29* (8), 3644-3652.
108. Park, J.; Joo, J.; Kwon, S. G.; Jang, Y.; Hyeon, T., Synthesis of Monodisperse Spherical Nanocrystals. *Angew. Chem. Int. Ed.* **2007,** *46* (25), 4630-4660.
109. Li, Y.; Xu, X.; Wang, C.; Ecker, B.; Yang, J.; Huang, J.; Gao, Y., Light-Induced Degradation of CH3NH3PbI3 Hybrid Perovskite Thin Film. *J. Phys. Chem. C*. **2017,** *121* (7), 3904-3910.
110. Rocks, C.; Svrcek, V.; Maguire, P.; Mariotti, D., Understanding surface chemistry during MAPbI3 spray deposition and its effect on photovoltaic performance. *J. Mater. Chem. C*. **2017,** *5* (4), 902-916.
111. Zeng, B.; Palui, G.; Zhang, C.; Zhan, N.; Wang, W.; Ji, X.; Chen, B.; Mattoussi, H.,

Characterization of the Ligand Capping of Hydrophobic CdSe–ZnS Quantum Dots Using NMR Spectroscopy. *Chem. Mater.* **2018,** *30* (1), 225-238.
112. Gibson, N. A.; Koscher, B. A.; Alivisatos, A. P.; Leone, S. R., Excitation Intensity Dependence of Photoluminescence Blinking in CsPbBr3 Perovskite Nanocrystals. *The Journal of Physical Chemistry C*. **2018,** *122* (22), 12106-12113.
113. Van Le, Q.; Jang, H. W.; Kim, S. Y., Recent Advances toward High-Efficiency Halide Perovskite Light-Emitting Diodes: Review and Perspective. *Small Methods*. **2018,** *2* (10), 1700419.
114. Kumawat, N. K.; Liu, X.-K.; Kabra, D.; Gao, F., Blue perovskite light-emitting diodes: progress, challenges and future directions. *Nanoscale*. **2019,** *11* (5), 2109-2120.
115. Zhang, F.; Cai, B.; Song, J.; Han, B.; Zhang, B.; Zeng, H., Efficient Blue Perovskite Light-Emitting Diodes Boosted by 2D/3D Energy Cascade Channels. *Adv. Funct. Mater.* **2020,** *30* (27), 2001732.
116. Dong, Y.; Wang, Y.-K.; Yuan, F.; Johnston, A.; Liu, Y.; Ma, D.; Choi, M.-J.; Chen, B.; Chekini, M.; Baek, S.-W.; Sagar, L. K.; Fan, J.; Hou, Y.; Wu, M.; Lee, S.; Sun, B.; Hoogland, S.; Quintero-Bermudez, R.; Ebe, H.; Todorovic, P.; Dinic, F.; Li, P.; Kung, H. T.; Saidaminov, M. I.; Kumacheva, E.; Spiecker, E.; Liao, L.-S.; Voznyy, O.; Lu, Z.-H.; Sargent, E. H., Bipolar-shell resurfacing for blue LEDs based on strongly confined perovskite quantum dots. *Nat. Nanotechnol.* **2020,** *15* (8), 668-674.
117. Wang, Y.; Li, T.; Li, Z.; Wang, S.; Deng, X., Solution-Processed Laminated Perovskite Layers for High-Performance Solar Cells. *Adv. Funct. Mater.* **2019,** *29* (45), 1903330.
118. Chiang, C.-H.; Wu, C.-G., A Method for the Preparation of Highly Oriented MAPbI3 Crystallites for High-Efficiency Perovskite Solar Cells to Achieve an 86% Fill Factor. *ACS Nano*. **2018,** *12* (10), 10355-10364.
119. Dong, Q.; Fang, Y.; Shao, Y.; Mulligan, P.; Qiu, J.; Cao, L.; Huang, J., Electron-hole diffusion lengths > 175 μm in solution-grown CH₃NH₃PbI₃ single crystals. *Science*. **2015,** *347* (6225), 967.
120. Sadhanala, A.; Ahmad, S.; Zhao, B.; Giesbrecht, N.; Pearce, P. M.; Deschler, F.; Hoye, R. L. Z.; Gödel, K. C.; Bein, T.; Docampo, P.; Dutton, S. E.; De Volder, M. F. L.; Friend, R. H., Blue-Green Color Tunable Solution Processable Organolead Chloride–Bromide Mixed Halide Perovskites for Optoelectronic Applications. *Nano Lett.* **2015,** *15* (9), 6095-6101.
121. Kim, H. P.; Kim, J.; Kim, B. S.; Kim, H.-M.; Kim, J.; Yusoff, A. R. b. M.; Jang, J.; Nazeeruddin, M. K., High-Efficiency, Blue, Green, and Near-Infrared Light-Emitting Diodes Based on Triple Cation Perovskite. *Adv. Opt. Mater*. **2017,** *5* (7), 1600920.
122. Hu, M.; Chen, M.; Guo, P.; Zhou, H.; Deng, J.; Yao, Y.; Jiang, Y.; Gong, J.; Dai, Z.; Zhou, Y.; Qian, F.; Chong, X.; Feng, J.; Schaller, R. D.; Zhu, K.; Padture, N. P.; Zhou, Y., Sub-1.4eV bandgap inorganic perovskite solar cells with long-term stability. *Nat. Commun.* **2020,** *11* (1), 151.
123. Wang, H.; Zhang, X.; Wu, Q.; Cao, F.; Yang, D.; Shang, Y.; Ning, Z.; Zhang, W.; Zheng, W.; Yan, Y.; Kershaw, S. V.; Zhang, L.; Rogach, A. L.; Yang, X., Trifluoroacetate induced small-grained CsPbBr3 perovskite films result in efficient and stable light-emitting devices. *Nat. Commun.* **2019,** *10* (1), 665.
124. Yoon, Y. J.; Shin, Y. S.; Park, C. B.; Son, J. G.; Kim, J. W.; Kim, H. S.; Lee, W.; Heo, J.; Kim, G.-H.; Kim, J. Y., Origin of the luminescence spectra width in perovskite nanocrystals with surface passivation. *Nanoscale*. **2020,** *12* (42), 21695-21702.
125. Nedelcu, G.; Protesescu, L.; Yakunin, S.; Bodnarchuk, M. I.; Grotevent, M. J.; Kovalenko, M. V., Fast Anion-Exchange in Highly Luminescent Nanocrystals of Cesium Lead Halide Perovskites (CsPbX3, X = Cl, Br, I). *Nano Lett.* **2015,** *15* (8), 5635-5640.
126. Akkerman, Q. A.; D'Innocenzo, V.; Accornero, S.; Scarpellini, A.; Petrozza, A.; Prato, M.; Manna, L., Tuning the Optical Properties of Cesium Lead Halide Perovskite Nanocrystals by Anion Exchange Reactions. *J. Am. Chem.* **2015,** *137* (32), 10276-10281.
127. Parobek, D.; Dong, Y.; Qiao, T.; Rossi, D.; Son, D. H., Photoinduced Anion Exchange in

Cesium Lead Halide Perovskite Nanocrystals. *J. Am. Chem.* **2017,** *139* (12), 4358-4361.
128. Yoon, S. J.; Kuno, M.; Kamat, P. V., Shift Happens. How Halide Ion Defects Influence Photoinduced Segregation in Mixed Halide Perovskites. *ACS Energy Lett.* **2017,** *2* (7), 1507-1514.
129. Yoon, S. J.; Stamplecoskie, K. G.; Kamat, P. V., How Lead Halide Complex Chemistry Dictates the Composition of Mixed Halide Perovskites. *J. Phys. Chem. Lett.* **2016,** *7* (7), 1368-1373.
130. Knight, A. J.; Herz, L. M., Preventing phase segregation in mixed-halide perovskites: a perspective. *Energy Environ. Sci.* **2020,** *13* (7), 2024-2046.
131. Lignos, I.; Protesescu, L.; Emiroglu, D. B.; Maceiczyk, R.; Schneider, S.; Kovalenko, M. V.; deMello, A. J., Unveiling the Shape Evolution and Halide-Ion-Segregation in Blue-Emitting Formamidinium Lead Halide Perovskite Nanocrystals Using an Automated Microfluidic Platform. *Nano Lett.* **2018,** *18* (2), 1246-1252.

Acknowledgements

강산이 변하는 10년을 넘는 11년의 시간을 UNIST에서, 그리고 그 중 7년의 시간을 대학원에서 보내고 이제 학위를 마무리하려 하고 있습니다. 돌이켜 보면 부족한 제가 작지 않은 시간을 무사히 보내고 성과를 내고 학위를 얻을 수 있었던 건 많은 분들의 도움 덕이었습니다.

우주와 공상과학을 좋아하던 고등학생의 저는 태양전지 전공이 있던 UNIST에 큰 흥미를 갖게 되어 진학하게 되었습니다. 비록 태양전지 전공은 입학 후 얼마 안 되어 사라졌지만, 그 흥미는 계속되어 태양전지 연구를 활발히 진행하던 NGEL과 지도교수님 김진영 교수님을 만날 수 있게 되었습니다. 당시 연구실에서는 유기 태양전지 분야를 주로 연구하였지만, 저는 양자점 분야에 흥미를 느끼게 되어 양자점 태양전지를 연구하고 싶었고 이런 저를 교수님께서는 지지해 주시며 하고싶은 연구를 할 수 있도록 지원해 주셨습니다.

작지 않은 시간을 양자점 태양전지를 연구하며 보냈지만, 양자점 태양전지는 소자 제작뿐만 아니라 합성 또한 공부할 필요가 있었고, 저에게 많은 시련과 좌절을 안겨주었습니다. 연구가 버거웠던 그때 김기환 박사님의 권유로 페로브스카이트 양자점 분야를 연구해보게 되었고, 행운이 겹쳐 성과를 얻을 수 있게 되었고 결국에는 전공 연구분야를 페로브스카이트 기반의 발광 소재로 변경하게까지 되었습니다.

비록 의도했던 대로 흘러가지는 않았던 학위기간이었지만, 그 과정 하나하나에서 많은 것을 배울 수 있었습니다. 작게 보면 양자점 태양전지를 연구하면서 배웠던 모든 것들 덕에 페로브스카이트 양자점 분야에서 성과를 얻을 수 있었고, 크게 보면 시련과 좌절을 겪으면서 스스로 성장하는 계기가 되었던 것 같습니다.

그러한 학위기간 중에서도 가장 어려웠던 일은 스스로 할 일을 찾아내야 하는 점이었던 것 같습니다. 이전에는 늘 주어진 일만 하던 저에게 스스로 해야 할 일을 찾는 것은 미지의 영역이었고 좌절도 있었으며 익숙해지는 데도 많은 시간이 걸렸던 것 같습니다. 때문에 연구주제를 바꾸게 되는 일도 있었지만 그러한 과정 속에서도 늘 믿고 기다려 주시고 제 뜻을 지지해주신 지도교수님 김진영 교수님께 너무나 감사한 마음입니다.

연구내외적으로 항상 많은 신경 써준 김기환 박사님께도 큰 감사의 말을 드리고 싶습니다. 연구실 내에서 다소 생소한 분야를 연구하면서 생기던 일들에 많은 조언을 해주시

고 과정에서 생기는 힘듦을 이해하고 지지해 주셔서 무사히 연구를 진행할 수 있었던 것 같습니다.

많은 시간을 함께 보낸 허정우 박사님께도 감사한 마음입니다. 학부시절부터 시작된 긴 인연으로 연구실을 소개해 주시고 잘 적응할 수 있도록 많은 도움을 주셨고 학위기간 동안 있었던 고민들에 많은 조언을 받았습니다. 감사합니다.

NGEL 식구들에게도 감사한 마음뿐입니다. 연구실에 많은 신경 쓴 혜림이누나, 항상모범이 되는 학범이형, 해외에서도 고생하시며 열심히 하시는 재기형, 밤낮을 가리지 않고 일한 세영이누나, 많은 노력과 성과를 보여준 송이누나와 택호, 선배님들에게 많은 것을 배웠고 동기로 많은 시간을 같이 지낸 강택이형, 나경이, 그리고 연구에 많은 도움을 준 후배님들, 이제 곧 졸업할 재원이, 실험실 궂은일 도맡아 하고 랩장으로 고생한 형수, 항상 연구에 열정적이고 같은 연구주제로 함께 많이 고생하고 큰 도움 준 윤섭이, 본인 연구를 찾으려 꾸준히 노력하는 혜원이, 과제로 고생 많이 하고 있는 지우, 항상 스스로 많은 문제를 해결하는 종득이형, 나노입자의 어려운 길을 걷기로 각오하고 고생하고 있는 찬범이, 석사로 잘 졸업하고 이제 취업할 현서, 언제나 최선을 다하고 있는 중건이, 합성하느라 고생한 우진이, 생소한 분야도 선배를 도와가며 열심인 도훈이, 이제 막 들어온 태희, 그리고 이제 들어올 재휘까지 모두에게 감사의 말을 전합니다.

학위논문을 심사하는데 시간을 할애해주신 송명훈 교수님, 권태혁 교수님, 박종남 교수님께도 감사드립니다.

7년이라는 시간을 버틸 수 있게 해준 친구들, 민규, 준규, 한준, 진수, 혜규, 정현이, Astral 친구들, 노네임드 친구들, S. U., K. D.와 K. A.에게도 고마운 마음입니다.

끝으로 항상 믿고 기다려 주신 부모님께도 감사하고 사랑한다는 말을 전하고 싶습니다.

학위기간이 완벽했다고 말할 순 없어도 할 수 있었던 최선을 다 하려고 노력했다고 생각합니다. 많은 분들의 도움 덕에 무사히 대학원 생활을 마무리한다는 것을 잊지 않고 앞으로의 인생도 열심히 살아보겠습니다. 정말 감사합니다.